

Important Notice

This copy may be used only for the purposes of research and private study, and any use of the copy for a purpose other than research or private study may require the authorization of the copyright owner of the work in question. Responsibility regarding questions of copyright that may arise in the use of this copy is assumed by the recipient.

UNIVERSITY OF CALGARY

Time-Lapse Numerical Modeling for a Carbon Capture and Storage (CCS) Project in Alberta,
Using a Poroelastic Velocity-Stress Staggered-Grid Finite-Difference Method

by

Shahin Moradi

A THESIS

SUBMITTED TO THE FACULTY OF GRADUATE STUDIES
IN PARTIAL FULFILLMENT OF THE REQUIREMENTS FOR THE
DEGREE OF DOCTOR OF PHILOSOPHY

GRADUATE PROGRAM IN GEOLOGY AND GEOPHYSICS

CALGARY, ALBERTA

July, 2016

© Shahin Moradi 2016

Abstract

A finite-difference algorithm was developed based on the Biot's equations of motion to model seismic wave propagation in poroelastic media. As opposed to the elastic case, in the poroelastic approach the properties of the pore fluid are taken into account in the modeling process. Poroelastic modelling could be useful in cases where the fluid content of the rock is of interest, such as Carbon Capture and Storage (CCS) projects. The developed program was then used to investigate the detectability of CO₂ in a CCS project in Alberta. Two models were defined for the baseline and monitor scenarios that respectively, represented the subsurface before and after injection of CO₂ and the corresponding synthetic seismic sections were generated. The difference between the calculated seismic sections for the two scenarios shows that the residual amplitude is comparable with the baseline amplitude. With this result, the injected CO₂ in the Quest project over a year could be detected providing the data have good bandwidth and a high signal-to-noise ratio. Furthermore, a comparison between the poroelastic algorithm and the elastic algorithm shows that the time-lapse effect in the poroelastic case is smaller than the one in the elastic case. In the fluid saturated media, some of the wave energy is dissipated due to fluid viscosity, and the poroelastic approach helps us to take this loss into account in the modeling process.

Acknowledgements

I would like to sincerely thank my supervisor Dr. Don Lawton for his guidance and support that have helped me to accomplish this work.

I gratefully acknowledge CMC (Carbon Management Canada), CREWES (Consortium for Research in Elastic Wave Exploration Seismology), and NSERC (Natural Science and Engineering Research Council of Canada) through the grant CRDPJ 379744-08 for financial support during my PhD program. I would also like to thank Shell Canada Limited for providing the well data.

Special thanks goes to David Henley for reading and commenting my thesis, Hassan Khaniani, Dr. Edward Krebes, and Peter Manning for useful discussions and suggestions. Thanks to Laura Baird for her help as an administrator support, and to Kevin Hall and Kevin Bertram for their technical support.

I am thankful to my husband Mahdi for his unlimited and unconditional love and support during all these years. I would also thank my brother Shahpoor for being an inspiration and a great mentor to me during my entire academic career. Also to my family members for sending love from the other side of the world.

Dedication

To my husband Mahdi, my siblings Shahram, Shahla, Shahpoor and my parents Maman and Kavka.

Table of Contents

Abstract	ii
Acknowledgements	iii
Dedication	iv
Table of Contents	v
List of Tables	vii
List of Figures and Illustrations	viii
1 Introduction	1
1.1 Carbon Capture and storage	1
1.2 Seismic monitoring	2
1.2.1 Forward modeling: finite-difference method	3
1.3 Poroelastic media	7
1.4 Motivation	7
1.5 Objectives	8
1.6 contributions	9
1.7 Thesis structure	10
2 Quest Carbon Capture and Storage (CCS) Project	12
2.1 Introduction	12
2.2 Quest CCS project	13
2.3 Geological setting	15
2.3.1 Basal Cambrian Sands	15
2.3.2 Middle Cambrian Shales	19
2.3.3 Lower Lotsberg Salt	19
2.3.4 Upper Lotsberg Salt	19
2.3.5 Overburden strata	19
2.4 Summary	23
3 Data and Gassmann Fluid Substitution	24
3.1 Introduction	24
3.2 Well logs	24
3.3 Gassmann Fluid Substitution	25
3.3.1 Theory	27
3.3.2 Work flow	28
3.3.2.1 Properties of the initially saturated rock	29
3.3.2.2 Fluid properties	29
3.3.2.3 Rock matrix properties	33
3.3.2.4 Porosity	33
3.3.3 Results and Discussion	33
3.4 Summary	36
4 Biot's Theory	37
4.1 Introduction	37
4.1.1 Stress-strain relations	38
4.1.2 Dynamic equations	42
4.1.3 Wave equations in 2D case	44

4.2	Perfectly Matched Layers	44
4.3	Summary	48
5	Finite difference modeling	50
5.1	Introduction	50
5.2	Discretization	51
5.3	The staggered grid technique	52
5.4	Discrete velocity-stress equations	53
	5.4.1 Discrete equations in the internal region	55
	5.4.2 Discrete equations in the PML region	56
5.5	Source implementation	58
5.6	Generated snapshots	60
	5.6.1 Uniform model with zero fluid viscosity: non-diffusive slow mode . . .	60
	5.6.2 Uniform model with nonzero fluid viscosity: diffusive slow mode . . .	61
	5.6.3 Two layer model with zero fluid viscosity	64
5.7	PML boundary condition	67
5.8	Stability	68
5.9	Summary	77
6	Time-lapse model-based numerical simulations for the Quest Carbon Capture and Storage project	78
6.1	Introduction	78
6.2	Baseline scenario	79
6.3	Monitor scenario	80
	6.3.1 Plume size calculation	81
6.4	Numerical modeling and discussion	82
6.5	Summary	85
7	Conclusions and Future Work	90
7.1	Conclusions	90
7.2	Future Work	92
	Bibliography	94
A	Matlab Code	98

List of Tables

3.1	Average physical properties of the BCS extracted from the well logs	25
3.2	Estimated properties of Brine and CO ₂ at the BCS conditions	30
3.3	Physical properties of BCS for baseline and monitor scenarios	35
4.1	List of symbols and their definitions	49
6.1	Physical properties of the elastic layers in the baseline and monitor scenarios. .	80

List of Figures and Illustrations

1.1	An illustration of the Sleipner project in North Sea. The CO ₂ generated from the natural gas is injected directly into the Utsira saline aquifer for permanent storage (Figure courtesy of Statoil).	4
1.2	Synthetic seismic data along with the observed data from the Sleipner project. a) Synthetic data prior to injection in 1994, b) Synthetic data after injection in 1999, c) Observed data prior to injection in 1994, d) Observed data after injection in 1999. The amount of injected CO ₂ was 2.3 million tonnes. Modified after Chadwick et al. (2005).	5
2.1	Alberta is divided into six regions based on the suitability of the basin for carbon sequestration (Bachu et al., 2000).	13
2.2	Area of study for the Quest project, as well as the location of well SCL-8-19-59-20W4 (Radway well). Figure is generated using Google maps.	14
2.3	Stratigraphic column of the Western Canadian Sedimentary Basin and the hydrological information. On the right a larger view of the Quest storage complex is illustrated. The target in the Quest CCS project is the Basal Cambrian Sands (Shell Canada Limited, 2010).	16
2.4	The map of BCS thickness at the area of interest along with the existing wells. The wells that penetrate the Precambrian basement are denoted with filled black circles. This includes the Radway well (8-19-59-20) (Shell Canada Limited, 2010).	17
2.5	East-west view of the Cambrian and lower Ordovician in the plains of Alberta and Saskatchewan. The Basal sands spread throughout most of Alberta and Saskatchewan. The sand unit is locally absent in some highs of Precambrian (Slind et al., 1994).	18
2.6	The distribution of the Middle Cambrian Shale over the Western Canadian Sedimentary Basin (WCSB) along with the approximate location of the Quest project (modified after Slind et al. (1994))	20
2.7	The distribution of the Upper and Lower Lotsberg Salts over the Western Canadian Sedimentary Basin (WCSB), and the approximate location of the Quest project (modified after Grobe (2000))	21
3.1	Data from well SCL- 8-19-59-20W4 and some of the horizons in the zone of interest. Respectively from bottom to top the tracks show the density, gamma-ray, P-wave velocity, S-wave velocity, and V_P/V_S ratio.	26
3.2	Carbon dioxide temperature-pressure diagram. The CO ₂ is in a supercritical state for when the temperature and the pressure are beyond the critical point. Copyright 1999 ChemicalLogic Corporation.	32
3.3	The physical properties of the fluid and the saturated rock at BCS after fluid substitution as a function of CO ₂ saturation. a) The bulk modulus of the fluid mixture, b) the density of the fluid mixture, c) the bulk modulus of the rock saturated with new fluid mixture, d) the density of the new saturated rock	34

3.4	Percent change in P-wave and S-wave velocities of the new saturated rock versus the CO ₂ saturation.	35
4.1	Schematic view of the PML region and how the damping factors a_x and a_z are defined in two directions of x and z.	45
5.1	Schematic view of the staggered grid. The particle velocities of the solid and the fluid, V_x, V_z, W_x and W_z are calculated on a staggered time grid and the rest of the unknowns are defined on a regular time grid. The fluid pressure P and the normal stresses of the solid, τ_{xx} and τ_{zz} are calculated on a regular spatial grid, and the rest of the unknowns re evaluated on a staggered spatial grid.	52
5.2	Calculation of $\Delta_x \tau_{xz} \Big _{i,j+1/2}$ on the staggered grid (equation 5.9).	54
5.3	Calculation of $\Delta_z \tau_{zz} \Big _{i,j+1/2}$ on the staggered grid (equation 5.10).	55
5.4	The Ricker wavelet used as an explosive source in the modelings, represented in time (a) and frequency (b) domains. The dominant frequency of this wavelet is 40 Hz.	59
5.5	The uniform model used in examples, and the location of the source. This model is based on the in-situ properties of the BCS that are listed in Table 3.3 as BCS_{Base}	61
5.6	Sample snapshots of the vertical particle velocities of the solid (top row) and the fluid with respect to solid (bottom row) in both x and z directions. The model used in this example is the uniform model with $b = 0$. The snapshots were taken at the time of 0.14 s. The fast and the slow P-waves are respectively denoted by P_f and P_s	62
5.7	Sample snapshots of the vertical particle velocities of the solid (top row) and the fluid respect to solid (bottom row) for three different values of factor b . By increasing the value of b , the slow P-wave starts to become diffusive and being absorbed in the medium. The fast and the slow P-waves are respectively denoted P_f and P_s . The snapshots were taken at the time of 0.14 s.	64
5.8	Traces from the vertical particle velocities of the solid in poroelastic media, for two values of $b = 0$ and $b = 10^5 Pa sm^{-2}$. The slow P-wave in the case of $b \neq 0$ dissipates quickly while in the case of $b = 0$ it does not dissipate in the medium.	65
5.9	The two-layer model used in the examples. The top layer represents the BCS with in-situ properties, also listed in Table 3.3 as BCS_{Base} . The lower layer represents the BCS after injecting CO ₂ , also listed in Table 3.3 as BCS_{Mon}	66
5.10	Snapshots of the vertical particle velocity of the solid for the two-layer model, calculated for a) poroelastic case, and b) elastic case. The horizontal line at the depth of 1000m represents the boundary. To see the reflections more clearly, the amplitudes are magnified by factor of 100. The direct and reflected waves are denoted in the figure as follows: the direct fast P-wave (P_f), the reflected fast P-wave ($P_f P_f$), the slow P-wave (P_s), the S-wave converted from the fast P-wave ($P_f S$), the slow P-wave converted from the fast P-wave ($P_f P_s$), and the fast P-wave converted from the slow P-wave ($P_s P_f$).	67

5.11	Snapshots of the vertical particle velocity of the solid with different values of $n_{PML}=0, 10, 20, 30$. By increasing the thickness of the PML region, the outgoing waves are absorbed more effectively. To see the artifacts more clearly, the amplitudes are magnified by the factor of 10.	69
5.12	a) An example of a PML grid defined for the uniform model with dimensions of $1000\text{ m} \times 1000\text{ m}$. The image shows the summation a_x+a_z where a_x and a_z are the attenuation factors in x and z directions. b) A closer view of the corner of the grid. In this example 20 grid points are used in the PML layer. The attenuation factors are zero at the internal grid and increase when moving towards the grid borders.	70
5.13	Sample shot gathers generated for the uniform model with $b \neq 0$, using the poroelastic algorithm, along with the selected traces from these gathers. a) No PML is used, therefore strong reflections from the boundaries are generated. b) A PML boundary with 20 nodes is used and the artifacts are efficiently removed. The amplitudes are magnified by the factor of ten to better illustrate the artifacts. c) and d) are selected trace at location of $x=600\text{ m}$ respectively from shot gathers in a and b.	71
5.14	Sample shot gathers generated for the uniform model with $b = 0$, using the poroelastic algorithm, along with the selected traces from these gathers. a) No PML is used, therefore strong reflections from the boundaries are generated. b) A PML boundary with 20 nodes is used and the artifacts are efficiently removed. The amplitudes are magnified by the factor of ten to better illustrate the artifacts. c) and d) are selected trace at location of $x=600\text{ m}$ respectively from shot gathers in a and b.	72
5.15	a) The surface separating the stable and unstable areas calculated based on Masson et al. (2006) criteria for our uniform model. This surface is plotted as a function of the time interval Δt , the grid size h and the factor m/ρ_f . b) The Δt - m/ρ_f plane view of the surface, which indicates for $m/\rho_f < \rho_f/\rho$ the solution is always unstable. c) The Δt - h view, where the relationship between Δt and h is always linear.	74
5.16	Several pairs of $(\Delta t, h)$ were used to test the stability of our algorithm for the uniform model (for $b = 0$). The stable pairs are shown with blue stars and the unstable ones are shown with red crosses. The straight line is the Masson et al. (2006) stability criteria calculated for this model. The stability of our algorithm matches the Masson et al. (2006) criteria very well.	75
5.17	Sample snapshots with different pairs of $(\Delta t, h)$. The top row of snapshots belong to the diffusive case ($b \neq 0$) and the bottom row snapshots belong to the non-diffusive case ($b = 0$). The pair $(\Delta t, h)=(0.3\text{ ms}, 4\text{ m})$ leads to instability in the solution, indicating that the diffusive mode makes the solution less stable than the non-diffusive case. Moreover, the pair $(\Delta t, h) = (0.2\text{ ms}, 6\text{ m})$ lead to dispersion in the slow P-wave confirming that increasing the grid size results in more numerical dispersion.	76

6.1	Cylindrical shape considered for the CO ₂ plume for the monitor model (left). The height of the cylinder is equal to the thickness of the BCS. The cylinder will appear as a block in the 2D model (right)	82
6.2	a) Acoustic impedance models for a) baseline and b) monitor scenarios. The warmer colors show higher impedance values. The blue color of the CO ₂ plume in the monitor model indicates the decrease in the BCS impedance after injecting CO ₂	83
6.3	Synthetic seismic sections generated using the poroelastic algorithm for the baseline (a) and the monitor(b) scenarios. The changes in the reflections and also the time shift in the monitor section are due to the injection of CO ₂ . The difference section is shown in (c) and is created by subtracting (b) from (a). The top and the base of the plume are observed in the difference section as a result of the change in the physical properties of the BCS	86
6.4	Synthetic seismic sections generated using an elastic algorithm for the baseline (a) and the monitor(b) scenarios. The changes in the reflections and also the time shift in the monitor section are due to the injection of CO ₂ . The difference section is shown in (c) and is created by subtracting (b) from (a).	87
6.5	a) Extracted traces from the sections in Figure 6.3 at the location of 1240 m, and b) Extracted traces from the sections in Figure 6.4 at the same location. The traces are shown in blue for baseline scenario, red for monitor scenario and black for the difference of the two scenarios.	88
6.6	Comparison between the traces generated using elastic and poroelastic algorithms. These are the same traces in Figure 6.5, but plotted separately for the two scenarios and also the time-lapse difference.	89

Chapter 1

Introduction

1.1 Carbon Capture and storage

The greenhouse effect is a natural process that keeps our planet warm enough for us to live on. Greenhouse Gases (GHG) allow the sun's rays to enter the atmosphere to warm up the planet, but keep the heat from escaping to space. The concerning issue is that the amount of greenhouse gases is increasing in the atmosphere due to human activities, leading to global warming. Among the greenhouse gases, carbon dioxide (CO₂) produced from fossil fuels and industrial processes is the largest contributor to anthropogenic GHG emissions (IPCC, 2015).

Carbon Capture and Storage (CCS) is considered by many to be one of the most effective methods for reducing CO₂ emissions in the atmosphere (Metz et al., 2005). In this process, CO₂ from large emitters is captured before it can be released into the atmosphere, transported and then injected into a deep geological formation for permanent storage. Based on the new regulations of the Government of Alberta (2015), the facilities that produce 100,000 tonnes of CO₂ annually, are required to reduce their emissions by 12%. This reduction target increases to 15% in 2016 and 20% in 2017. The producers that do not reach their target will have to pay the carbon fine that is \$20 per tonne in 2016 and this amount increases to \$30 in 2017.

Alberta's new climate change strategy draws attention to the importance of employing CCS technology in order to reduce carbon emissions. Alberta has great potential and opportunities for CCS. There are numerous depleted oil and gas reservoirs, deep saline aquifers and coal-beds in Alberta's basin that are ideal for CO₂ sequestration (Michael et al., 2009; Bachu et al., 2000, 2002) .

1.2 Seismic monitoring

CCS technology consists of three major steps: capture, transport, and storage. Prior to injection into the storage formation, a comprehensive study is carried out to investigate the feasibility of sequestration and containment in the storage formation. The focus of this dissertation is on the storage step. The seismic method is used during different phases of the project from pre-injection to facility closure for monitoring purposes. The goal is to ensure that the injected CO₂ remains within the storage formation, since the leakage of the CO₂ into the groundwater, soil, or into the atmosphere poses health and environmental risks.

A laboratory study by Wang et al. (1998) on flooding CO₂ in carbonate reservoir showed that the P-wave velocity decreased 4–11 % in the saturated rock. In fact, injecting CO₂ into a fluid saturated rock will decrease its P-wave velocity due to the low incompressibility of CO₂. Consequently, the seismic response of the reservoir undergoes some changes that help in tracking the path of the injected CO₂. Time-lapse seismic methods have become popular in the industry to follow the changes in the oil reservoirs after production or injection (Greaves and Fulp, 1987; Watts et al., 1996; Wang, 1997; Lumley, 2001). In the time-lapse method, a set of baseline data prior to production is acquired and used as a reference to observe the changes exhibited by the reservoir after production. This is accomplished by tracking the changes in the seismic amplitude, traveltimes and other attributes between baseline and monitor data. The same idea has been utilized in CO₂ sequestration projects for imaging the CO₂ plume in the storage reservoir (Arts et al., 2004; Vera, 2012; Alshuhail, 2011; Carcione et al., 2006).

Numerical modeling is a key step in time-lapse studies, particularly in CO₂ sequestration projects. Numerical methods are employed to predict the possible response of the reservoir after injection. In this process, two models are defined, one for baseline and one for monitor scenarios, and the possible seismic responses of the two models are calculated numerically. The monitor model, that represents the subsurface model after injection, is generated by adding a CO₂ plume to the baseline model. Numerical modeling can help save millions of dollars in CCS

projects by assisting the survey designs and planning strategies.

The Sleipner project in Norway, which is the first industrial scale CO₂ storage project in the world, is an excellent example of utilizing seismic methods in CCS technology. The project has been conducted by Statoil since 1996 at the Sleipner gas field in North Sea, Norway (Chadwick et al., 2005; Arts et al., 2004). The CO₂ produced from the Sleipner natural gas field is injected into the Utsira formation for greenhouse gas mitigation purposes. A smaller project, named Saline Aquifer CO₂ Storage (SACS) was specifically defined to monitor the injected CO₂. Figure 1.1 illustrates an overview of the storage process in Sleipner. A baseline seismic survey was collected in 1996 prior to initial CO₂ injection. The purpose was to monitor the fate of CO₂ as well as the shape of the plume after injection. Figure 1.2 shows the time-lapse field data along with numerical modeling results for this site (Chadwick et al., 2005). In order to generate the monitor data, a CO₂ saturation model was defined and the synthetic data were generated for this model. The synthetic seismic data match the real data quite well, indicating that the modeled CO₂ plume is likely similar to the real plume. The effect of the injected CO₂ appears as a change in the reflection signature as well a time push-down effect for the reflections within and below the CO₂ plume. The push-down effect is caused by the decrease in the seismic wave-velocity due to presence of CO₂ in the formation. The baseline and monitor surveys were acquired, respectively, in 1994 before injection, and in 1999 after injecting 2.35 million tonnes of CO₂. SACS ended in 2002, but the CO₂STORE project has been continuing parts of its activities since then.

1.2.1 Forward modeling: finite-difference method

Seismic forward modeling is the process of numerically generating seismic data based on a known geological model. In practice, the subsurface model is unknown, and the acquired seismic data are used to estimate the elastic properties of the subsurface through a process called “inversion”. Forward modeling is an essential step in the inversion process, and thus has been always of interest in geophysical applications. Carcione et al. (2002) offer a comprehensive

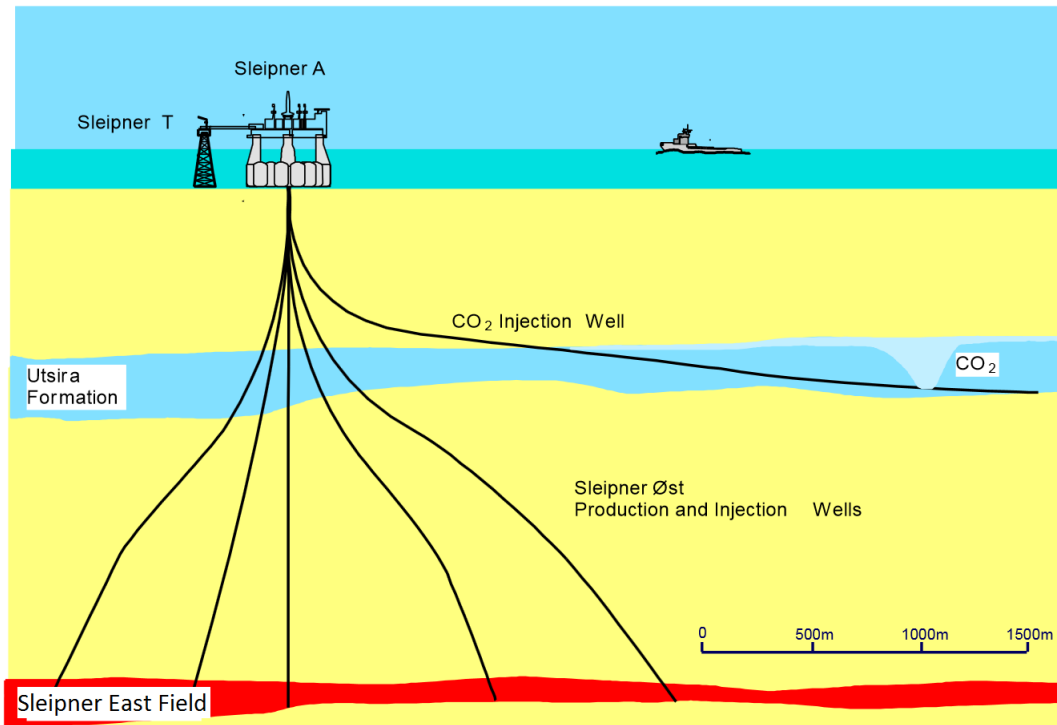


Figure 1.1: An illustration of the Sleipner project in North Sea. The CO₂ generated from the natural gas is injected directly into the Utsira saline aquifer for permanent storage (Figure courtesy of Statoil).

review of the different numerical modeling methods.

The finite-difference method is a popular approach among the numerical methods of seismic modeling. The main reason is that in this method the entire waveform is modeled based on the wave equations of motion. Therefore, it is the most accurate method for modeling seismic waves. The basic concept of finite-difference method is to replace the partial derivatives in the partial differential wave equations with their approximations based on Taylor series. The wave equations can be then solved on a numerical grid to obtain the wave motions in the medium.

A general summary of the main steps of finite-difference modeling is presented here, and the details will be presented in Chapter 5. These steps are:

1. **Wave equation formulation:** Wave equations can be either written in a displacement-stress formulation, or a velocity-stress formulation. The advantage of the velocity-stress

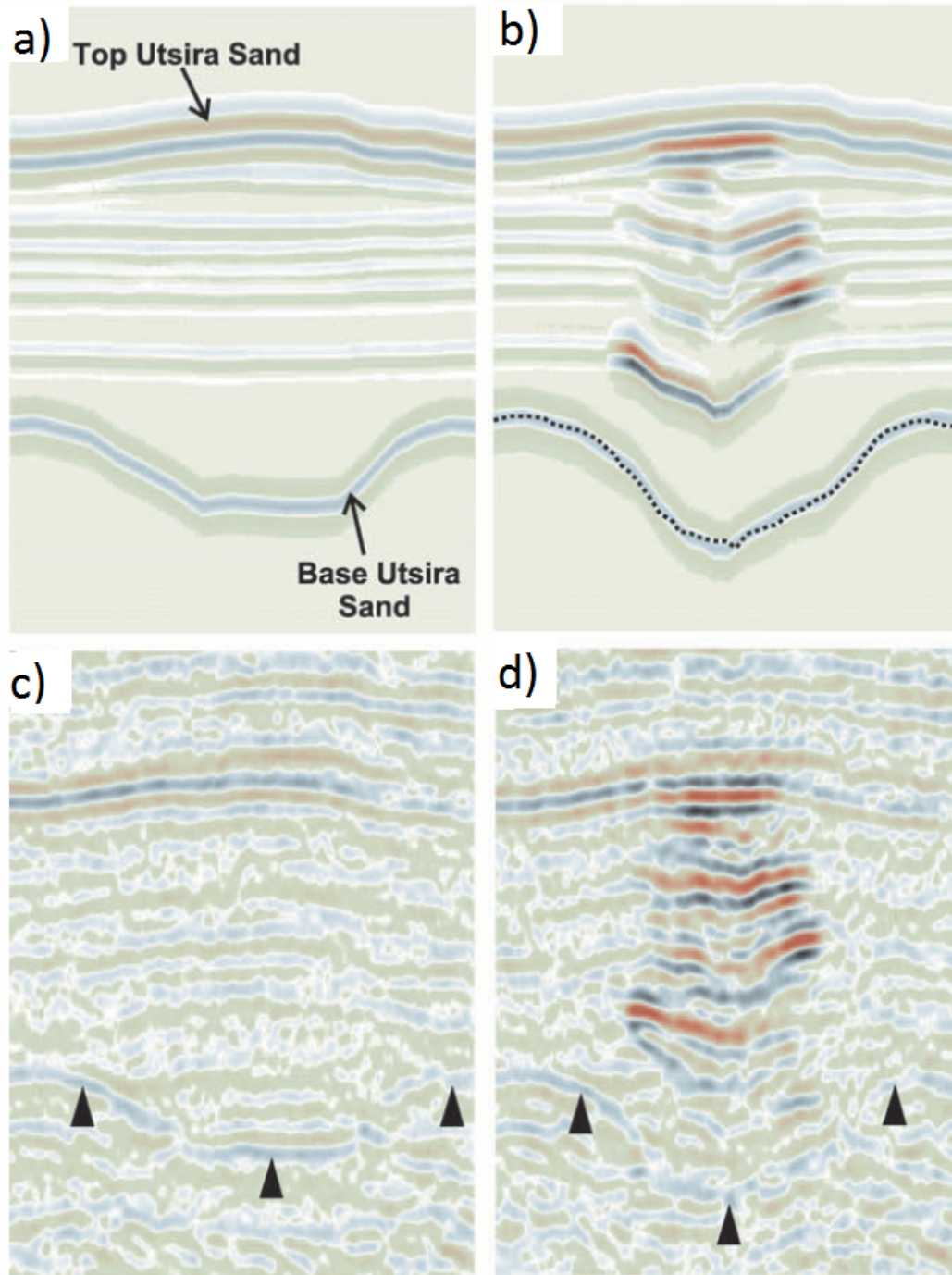


Figure 1.2: Synthetic seismic data along with the observed data from the Sleipner project. a) Synthetic data prior to injection in 1994, b) Synthetic data after injection in 1999, c) Observed data prior to injection in 1994, d) Observed data after injection in 1999. The amount of injected CO₂ was 2.3 million tonnes. Modified after Chadwick et al. (2005).

formulation is that the equations are first-order in time, making it easier to solve. In fact, the time derivatives of the displacements in the displacement-stress equations are replaced by velocity to reduce the order in time in the equations. The velocity-stress formulation is typically used with the staggered grid scheme of discretization. The wave equations and also the finite-difference scheme used in this thesis will be explained in more detail in Chapters 4 and 5.

2. **Discretization:** In order to numerically solve any partial differential equations using the finite-difference method, it is necessary to discretize the equations first. This is done by replacing the time and space derivatives with their approximations from Taylor series.
3. **Source implementation:** The seismic sources are of different types depending on their generated force. For example, explosive source and shear vibrator, respectively impose pressure and shear forces on the medium. In finite-difference modeling, the source is implemented by adding the force to the stress and displacement (or velocity) fields. For instance, in the case of a pressure source, the normal stress fields must be equal at the source location and initial time. Therefore, $\tau_{xx} = \tau_{yy} = \tau_{zz}$, where $\tau_{xx}, \tau_{yy}, \tau_{zz}$ are the normal stresses in x,y and z directions. Accordingly, to add an explosive source, the force function is added to the normal stress fields at the initial time of calculations.
4. **Boundary conditions:** Numerical models are finite in space as opposed to the real Earth. Therefore, the wave reflects from the boundaries of the model, instead of traveling infinitely as it would in the Earth. In order to avoid these undesired reflections, a layer is added to the grid in which the outgoing waves dissipate quickly.

For simplification and also cost-saving purposes, the Earth is usually assumed to be a single-phase elastic solid. Therefore, only elastic solid properties are incorporated in the modeling process, and the wave equations are formulated for an elastic medium. However, the reservoirs that are of interest in most geophysical applications are porous rocks saturated with fluid mixtures.

This type of medium, that is also referred to as "poroelastic", is the main focus of this thesis. CCS projects are excellent examples of the need to consider poroelastic media. Therefore, in order to better model seismic waves in CCS projects, the wave behavior in fluid saturated media needs to be well understood.

1.3 Poroelastic media

Maurice Biot first proposed a theory of poroelasticity to describe wave propagation in fluid saturated media (Biot, 1962). His theory holds that a poroelastic medium is composed of an elastic solid frame and a viscous pore fluid mixture. It is known that, in such a medium, two compressional waves are generated: a fast P-wave due to the motion of the solid rock frame, and a slow P-wave due to the relative motion of the fluid with respect to the solid frame. In low frequencies, such as typical seismic frequencies, the effect of fluid viscosity becomes stronger than the internal effects, leading to diffusion of the slow mode (Carcione et al., 2010). Therefore, the slow P-wave should not be observed at low frequencies. However, when the ratio of the fluid viscosity to the permeability (the factor b) tends to zero, the slow mode begins to behave as a traveling wave. However, in both cases the fluid movement affects the wave energy, which accordingly affects the seismic response of the medium. The wave behavior in poroelastic media can be useful to monitor CCS projects since the storage rocks are porous and saturated with fluids.

1.4 Motivation

Carbon Capture and Storage is the most effective technology for short-term mitigation of greenhouse gases (Metz et al., 2005). An important step in successfully deploying this technology is to ensure that it does not pose any health and environmental risks. Time-lapse seismic is one of the key parts of the Measurement Monitoring and Verification (MMV) program, which aims to assure that the storage formation securely retains CO_2 without any leakage risks. MMV in-

volves initial numerical forward modeling to investigate the feasibility of the time-lapse seismic surveys in detecting and tracking the injected CO₂. Performing more realistic forward modeling is therefore valuable in the MMV program for better designing seismic surveys as well as for planning purposes. This can be accomplished only by using more accurate modeling algorithms, such as poroelastic modeling, in which the effect of injected fluid is taken into account in the calculations.

1.5 Objectives

As discussed earlier in this chapter, the importance of seismic numerical modeling in the CCS technology is well known. Any further improvement of the numerical methods could lead to a significant difference in the management of CCS projects. Therefore, The main objectives of this dissertation are summarized here, and are:

- To develop a forward modeling program using the finite-difference method to model wave propagation in poroelastic media. In poroelastic modeling both fluid and solid phases are considered in the modeling process, and therefore it is specifically useful for simulating the seismic response of the fluid saturated media in CCS projects.
- To investigate the role of factor b (the ratio of viscosity to permeability) on the seismic response of the saturated rock. The factor b is expected to cause energy loss, and therefore needs to be investigated in more detail. This involves examining the wave behavior in the presence or absence of the factor b in the seismic frequency range.
- To use the finite-difference program developed in this thesis to carry out time-lapse numerical modeling for the Quest CCS project in Alberta. The Quest project is a suitable example of a poroelastic medium. Hence, the effect of the pore fluid in this project can be investigated by comparing the synthetic traces calculated from our poroelastic program with the ones generated by an elastic algorithm, in which the medium is assumed to be a

single solid phase without fluid effect.

- A final objective is to perform a time-lapse feasibility analysis for the Quest project. This involves the examination of the changes in the seismic signature of the storage rock after injection. This is accomplished by a Gassmann fluid substitution approach and poroelastic finite-difference modeling, and comparing the seismic reflection amplitudes and times before and after CO₂ injection.

1.6 contributions

The main contribution of this dissertation is to investigate the effect of the fluid viscosity on wave propagation in fluid saturated media. This is accomplished by developing a 2-D velocity-stress staggered-grid finite-difference algorithm to simulate the wave propagation in such media. To my knowledge, the effect of fluid viscosity in poroelastic media has yet to be deeply explored in the literature. Using the developed program, I demonstrate that there is a measurable loss of wave energy in the poroelastic media due to diffusion of the slow P-wave that is not observed in the elastic media. Results show that by increasing the fluid viscosity, the slow P-wave is more quickly absorbed in the medium.

Furthermore, a poroelastic model is constructed for a Carbon Capture and Storage (CCS) project in Alberta, and a model-based time-lapse simulations is carried out using the developed program. This includes a framework for defining model parameters to perform a poroelastic time-lapse modeling. By comparing the modeling results with those generated from an elastic program in which the fluid phase is ignored, the amount of loss caused by the fluid phase is revealed. The accuracy of the modeling algorithm may aid in enhancing seismic imaging and monitoring the injected CO₂ volume.

1.7 Thesis structure

This dissertation is composed of 7 chapters. The first chapter is a brief introduction to the Carbon Capture and Storage technology (CCS), seismic monitoring and discusses motivation and objectives.

In Chapter 2 the Quest CCS project is introduced. Then the geological setting of the area including the storage formation Basal Cambrian Sands (BCS), the major seals and baffles are presented.

The well data from the Quest project are presented in Chapter 3. These data are used to extract physical properties of the storage formation, BCS, and also to define some numerical models that will be used as examples in the later chapters to verify the finite-difference program. Fluid substitution modeling based on Gassmann's method is also carried out in this chapter to predict the changes in the properties of the BCS storage formation, after injecting a certain amount of CO₂. These properties are also used later to define baseline and monitor models for time-lapse modeling.

Biot's theory of poroelasticity and the equations of motion in the fluid saturated media are introduced in Chapter 4. Then the partial differential equations for the 2D case, in which the wave travels only in the x-z plane, are presented. Finally, the Perfectly Matched Layer method (PML) is used to derive the partial differential equations for the grid boundary. These equations will be used in a thin layer around the grid in order to absorb the outgoing waves and avoid the numerical reflection from the grid boundaries.

Chapter 5 explains the steps in the finite-difference modeling procedure. A staggered grid method is used to obtain the discrete velocity-stress partial differential equations for both internal and PML regions. Some example snapshots are presented in this chapter in order to verify the finite-difference program. Then the effect of the factor b on the generated snapshots as well as synthetic traces are analyzed. At the end of the chapter, the PML boundary condition, and also the stability of the program are examined.

Time-lapse numerical modeling is carried out for the Quest project in Chapter 6. The models for the baseline and the monitor scenarios are defined based on the properties extracted from the well logs as well as the results from the Gassmann's fluid substitution. A CO₂ plume is added to the baseline model to define the monitor model. The objective is to qualitatively assess the effect of the CO₂ on the seismic signature of the BCS, such as reflection amplitude and time. Eventually, the conclusions and recommendations for future work are presented in Chapter 7.

Chapter 2

Quest Carbon Capture and Storage (CCS) Project

2.1 Introduction

Carbon Capture and Storage (CCS) technology plays an important role in Alberta's strategies to mitigate greenhouse gas emissions. Several studies on the feasibility of CCS in Canada have been carried out based on hydrological and geothermal regimes, hydrocarbon potential, tectonics, and the basin structure (Bachu et al., 2000). Bachu et al. (2002) investigated possible suitable geological formations for carbon storage projects throughout Canada. The study showed that the most suitable formations are within the Western Canadian Sedimentary Basin (WCSB) where deep saline aquifers are overlain by several extensive impermeable formations. Moreover, Alberta's portion of the basin is divided into six regions based on the geological attributes and the potential for carbon storage (Figure 2.1). These regions ranged from unsuitable at the eastern region to extremely suitable in southeastern and central part of Alberta. Central Alberta is considered to be extremely suitable for sequestration for several reasons:

- This region is located in the center of WCSB where the thicknesses of the formations are suitable for sequestration.
- The aquifers are sealed by multiple impermeable layers such as salt and shale, lowering the risk of CO₂ upward migration.
- Numerous coal beds as well as oil reservoirs close to the depletion stage are available for sequestration.
- This region is tectonically inactive, and there are no active faults to threaten the containment of the injected CO₂.

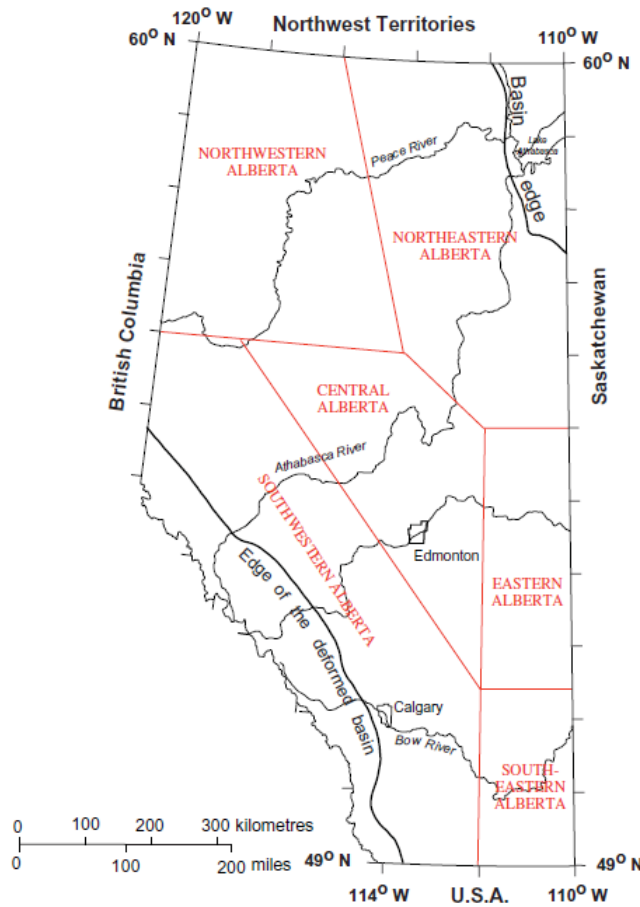


Figure 2.1: Alberta is divided into six regions based on the suitability of the basin for carbon sequestration (Bachu et al., 2000).

This reveals the potential of Alberta for successful sequestration of CO₂. In fact, since Central Alberta is a heavy industrial region, the CO₂ could be transported to the injection sites with minimal transportation costs.

2.2 Quest CCS project

Quest is a large-scale CCS project conducted by Shell and its partners in the central part of the Alberta basin. The purpose of this project is to reduce CO₂ emissions from the Scotford Upgrader by storing it in a deep geological formation. The location of the Scotford Upgrader is about 5 km northeast of Fort Saskatchewan, within Alberta's heavy industrial zone (Figure 2.2).



Figure 2.2: Area of study for the Quest project, as well as the location of well SCL-8-19-59-20W4 (Radway well). Figure is generated using Google maps.

Storage sites are preferred to be close to industrial regions where high levels of CO₂ are produced. The life of the Quest project is expected to be minimum of 25 years, which is equal to the life of the Scotford Upgrader. The captured CO₂ will be transferred to the injection site by an approximately 80 km long pipeline and will be injected into the ground through 3 injection wells in the area. The rate of injection will be 1 million tonnes a year, which is 80 percent of the CO₂ produced by the Scotford Upgrader. Therefore, the estimated amount of injected CO₂ during the life of the project will be about 27 million tonnes. Shell's feasibility analysis was carried out using the existing 3D surface seismic data as well as well logs (Shell Canada Limited, 2010). Gravity and magnetic data sets have also been acquired along with the seismic data. The

injection site was chosen so that it is far away from the existing deep wells in the area (Alberta Department of Energy, 2015). This is to ensure that there will not be possible groundwater contamination due to the brine moving up from the legacy wells. These wells penetrate at least one of the geological seals; and thus injecting CO₂ in the vicinity of these wells would increase the risk of brine penetrating shallower aquifers and contaminating the groundwater (Figure 2.4). The selected geological formation for the CO₂ storage in Quest project is the Basal Cambrian Sands(BCS), which is a saline aquifer within WCSB, at an approximate depth of 2 km below surface. It is expected that the BCS has the capacity to contain the CO₂ emissions from the Scotford Upgrader for decades.

2.3 Geological setting

The storage complex for the quest project is composed of the Basal Cambrian Sands, three major seals, and shallow strata of WCSB. Figure 2.3 shows the regional stratigraphic section for the zone of interest along with a more detailed view of the Quest storage complex. The BSC lies directly on top of the crystalline Precambrian basement rocks. Negligible porosity and permeability of the Precambrian granites make a confining zone directly beneath the basal sands.

Containment of the storage complex is one of the principal requirements of CO₂ sequestration. This is to ensure that the injected CO₂ is permanently confined within the storage unit. More details on the storage complex BCS and the geological seals are presented below.

2.3.1 Basal Cambrian Sands

The injection zone for the quest project is the Basal Cambrian Sands (BCS) formation, which is composed of fine to coarse-grained sandstone with some shale inclusions. BCS lies unconformably on the erosional upper surface of Precambrian basement. This unconformity is present between the Precambrian and Cambrian sequence throughout the WSCS, and represents 1.5 bil-

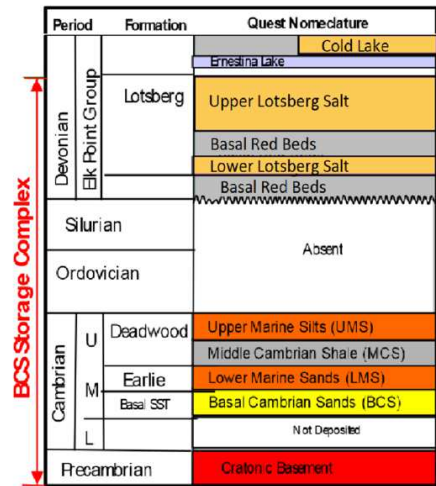
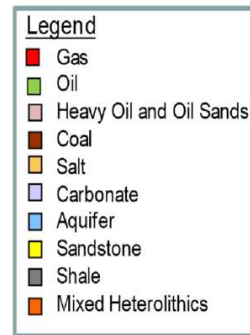
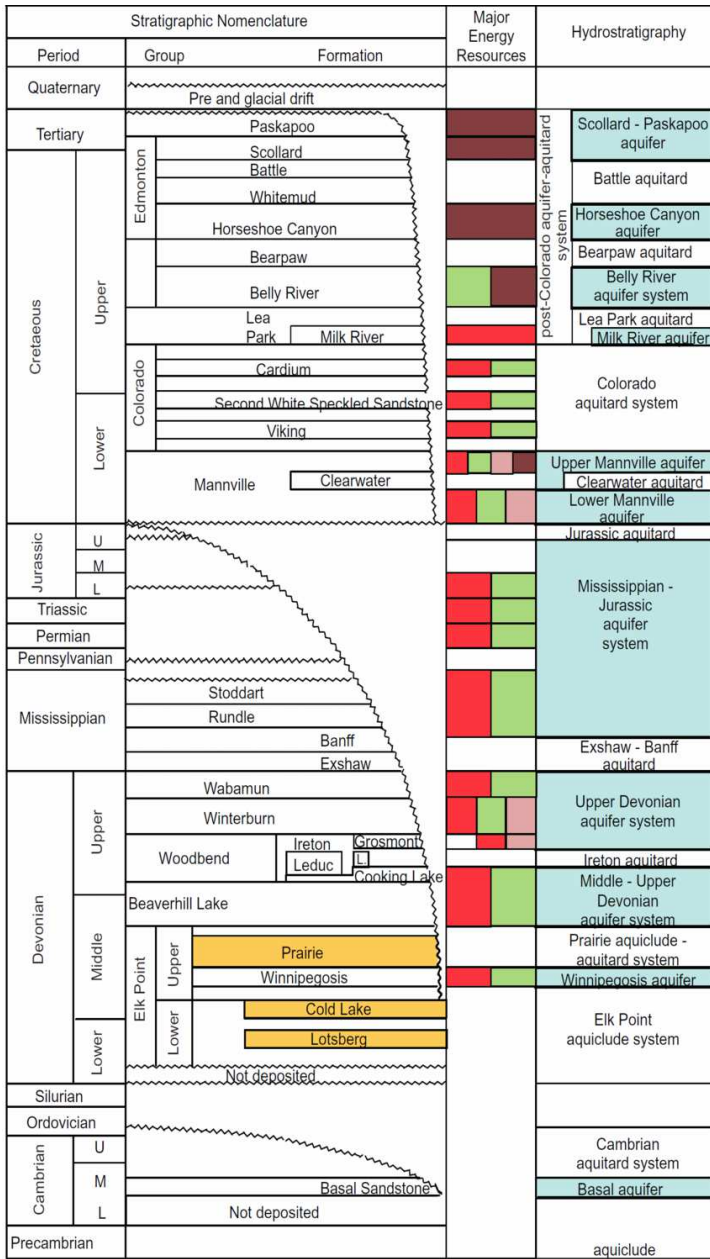


Figure 2.3: Stratigraphic column of the Western Canadian Sedimentary Basin and the hydrological information. On the right a larger view of the Quest storage complex is illustrated. The target in the Quest CCS project is the Basal Cambrian Sands (Shell Canada Limited, 2010).

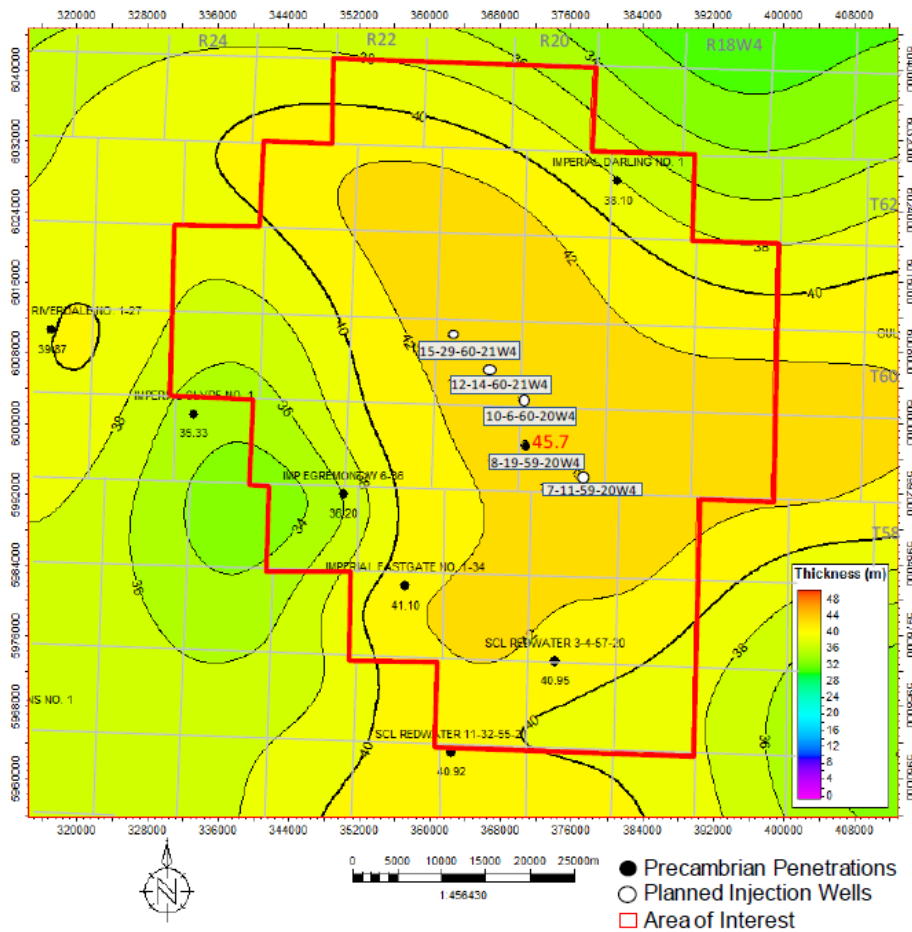


Figure 2.4: The map of BCS thickness at the area of interest along with the existing wells. The wells that penetrate the Precambrian basement are denoted with filled black circles. This includes the Radway well (8-19-59-20) (Shell Canada Limited, 2010).

lion years worth of missing deposition and subsequent erosion (Slind et al., 1994). The BCS is present almost throughout most of Alberta and Saskatchewan except at some local Precambrian highs that have prevented deposition (Figure 2.5).

In terms of reservoir quality, the BCS provides ideal conditions for CO₂ sequestration. The core data suggest a porosity of 8–24% and a permeability of 1 *mD* to > 1 *D*. The geological confinement of the BCS is another criteria that make it favorable for storage. BCS is overlain by three major seals and multiple aquitard systems that effectively isolate the injected CO₂ (Alberta

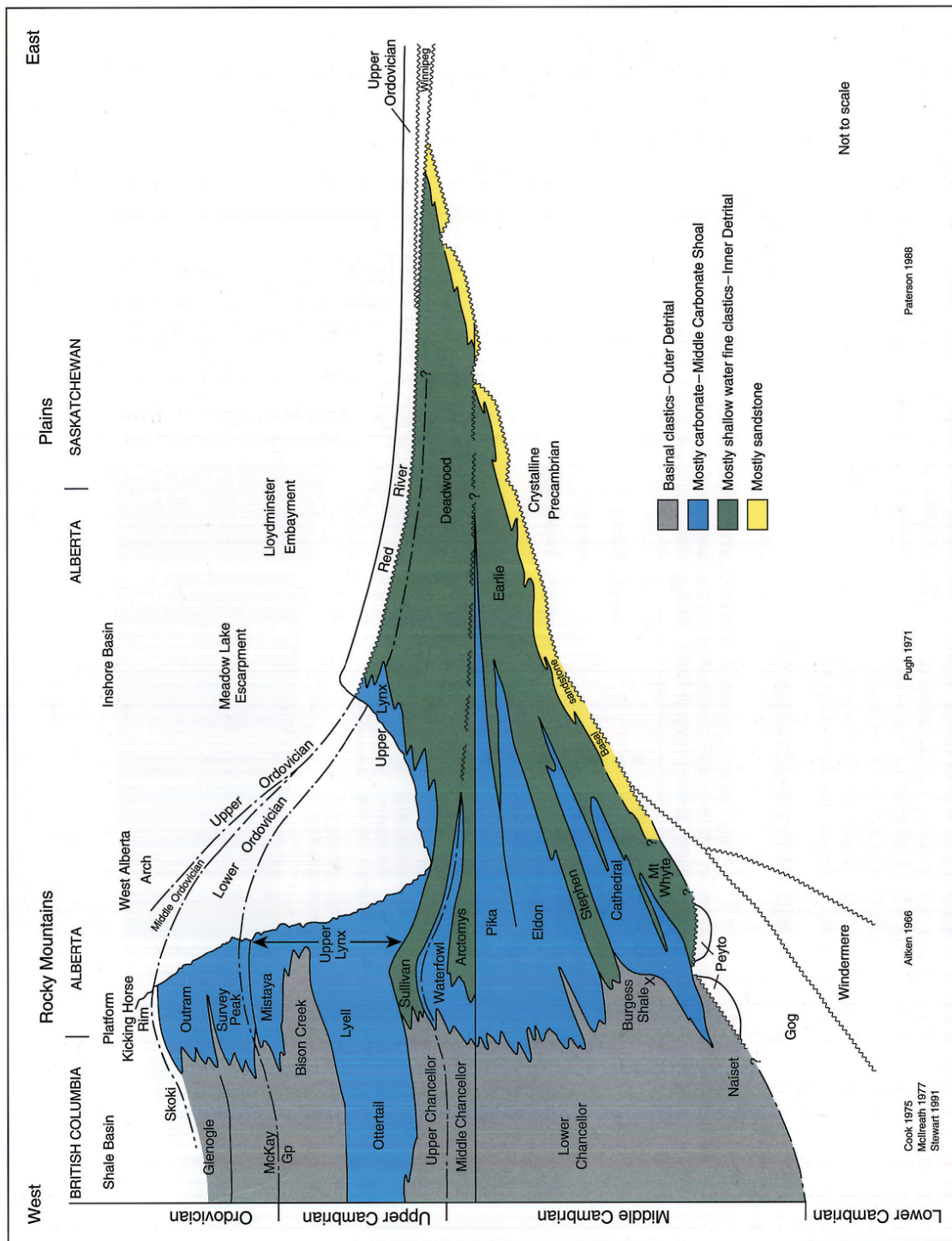


Figure 2.5: East-west view of the Cambrian and lower Ordovician in the plains of Alberta and Saskatchewan. The Basal sands spread throughout most of Alberta and Saskatchewan. The sand unit is locally absent in some highs of Precambrian (Slind et al., 1994).

Department of Energy, 2015). These major seals are: Middle Cambrian Shales (MCS), Lower Lotsberg Salt, and Upper Lotsberg Salt (Figure 2.3).

2.3.2 Middle Cambrian Shales

Middle Cambrian Shales (MCS) from the Deadwood Formation is the first and the main seal above the BCS. This unit, along with the Lower Marine Sands (LMS) from the Earlie Formation and Upper Marine Silts from the Deadwood Formation form an aquitard overburden for BCS. The distribution of the MCS in Alberta and Saskatchewan is shown in Figure 2.6. The average thickness of this layer is approximately 60 m.

2.3.3 Lower Lotsberg Salt

The lower Lotsberg Salt extends through central and eastern Alberta, and continues across the border into Saskatchewan (Figure 2.7). The Top of the Lower Lotsberg Salt is at a depth between 1050 to 2100 m, and the maximum thickness of this unit is 60 m. This is a halite aquitard within the Devonian Elk Point Group, which makes an excellent upper seal for the BCS aquifer.

2.3.4 Upper Lotsberg Salt

The Upper Lotsberg Salt is another halite formation in the Devonian Elk Point Group that also extends through central Alberta and Saskatchewan but over a larger area (Figure 2.7). The maximum thickness is around 150 m and the depth to top of the formation starts from 750 m in the east and increases to 2100 m in the west. The Lower and Upper Lotsberg Salts are separated by the Devonian mudstones (Shell Canada Limited, 2010; Grobe, 2000).

2.3.5 Overburden strata

Within the overburden strata, there are some layers deposited between the major seals that act as barriers for the Quest storage complex (Shell Canada Limited, 2010). These layers are:

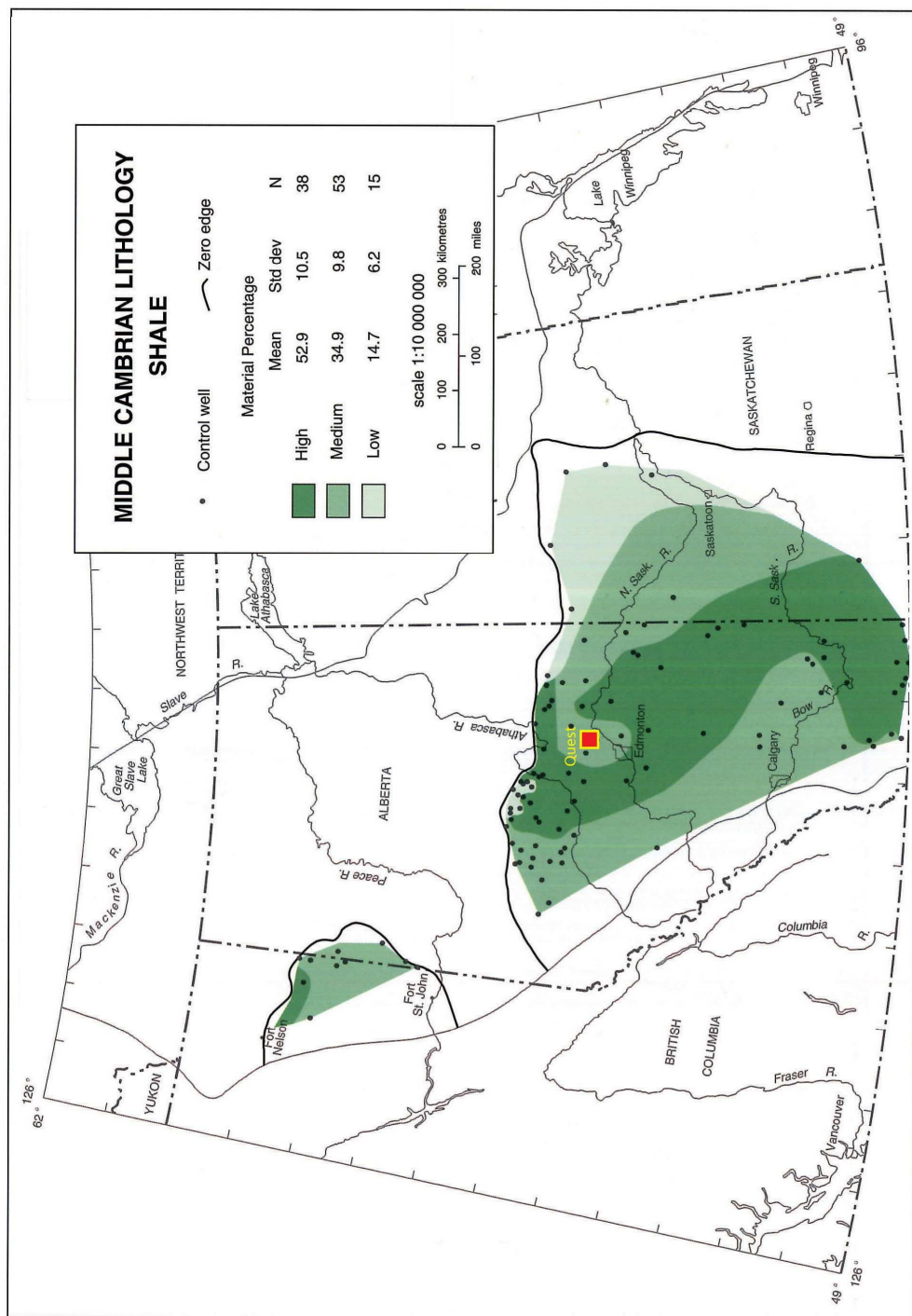


Figure 2.6: The distribution of the Middle Cambrian Shale over the Western Canadian Sedimentary Basin (WCSB) along with the approximate location of the Quest project (modified after Slind et al. (1994))

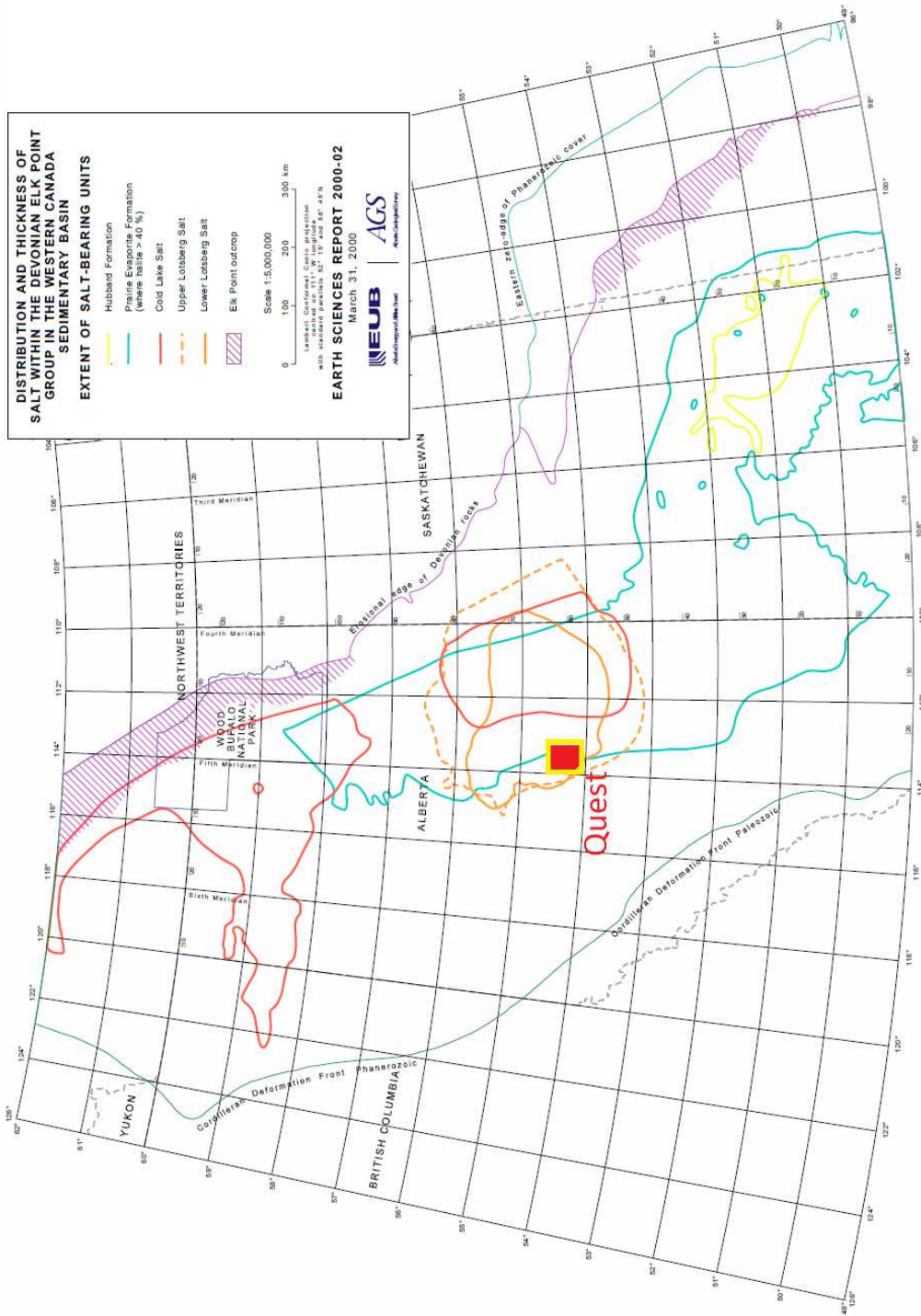


Figure 2.7: The distribution of the Upper and Lower Lotsberg Salts over the Western Canadian Sedimentary Basin (WCSB), and the approximate location of the Quest project (modified after Grobe (2000))

- *Lower Marine Sands(LMS) from the Earlie Formation:* The BCS is directly overlaid by LMS. The effective porosity of the LMS is estimated to be 6% with the average permeability being 4 mD. However, the insignificant vertical permeability of the LMS prevents the CO₂ from migrating upwards.
- *Upper Marine Silts (UMS) from the Upper Deadwood Formation:* Directly overlying the Cambrian MCS is the Upper Cambrian UMS, with the maximum thickness of 60 m. The Cambrian UMS is predominantly shale with an effective porosity of 1–2 % and permeability values less than 1 mD. The poor permeability and porosity of the UMS make it an effective barrier for the CO₂.
- *Devonian Basal Red Beds:* The fine grained Basal Red Beds lie directly above the Cambrian UMS. This layer, with a typical porosity of 5 % and permeability values between 0.001–1 mD creates another baffle for the storage complex in the Quest project.

Besides the impermeable layers mentioned above, there are multiple aquitard and aquifer systems in the shallower overburden strata. Some hydrologic characteristics of the overburden strata could be summarized as follows:

- Winnipegosis Formation within the Elk Point Group is the first major porous layer above the BCS. However, the Prairie Evaporites that consists of dolomite, salt and shale, lie directly above this formation. Therefore, Prairie Evaporites form an aquitard overlying the Winnipegosis Formation, acting as a barrier for the migration of CO₂.
- The middle Devonian Beaverhill Lake Group, are considered an aquifer system lying above the Prairie Evaporite Formation. The Ireton Formation separates the middle Devonian aquifer system from the upper Devonian aquifer. Ireton is a thick aquitard composed of shale and marlstone within the Leduc Group.
- There is a major absence in deposition from the Upper Devonian to Lower Cretaceous.

Above this unconformity, the Mannville aquifer system is overlaid by the Colorado aquitard system.

- Above the Colorado aquitard, there is a sequence of aquitards and aquifers from the upper Cretaceous to Tertiary, referred to as “post-Colorado aquifer-aquitard system” (Bachu et al., 2000).

2.4 Summary

The Western Canadian Sedimentary Basin (WCSB) has excellent potential for carbon sequestration. This region, which is tectonically inactive, contains deep saline aquifers and oil reservoirs near depletion stage, as well as coal-beds, that are all suitable for CO₂ storage. The Quest project, which is being conducted in Alberta by Shell Canada Limited and its partners, is a perfect example of unlocking this potential. The project is located within a heavy industrial zone in central Alberta, and the geological setting of the storage complex suggests an excellent containment of CO₂. The injection zone, Basal Cambrian Sands (BCS), is overlain by multiple impermeable layers, reducing the chance of CO₂ upward migration. Furthermore, high porosity and permeability of the BCS, offers an ideal reservoir quality for injection of CO₂.

Chapter 3

Data and Gassmann Fluid Substitution

3.1 Introduction

Fluid substitution modeling is an essential step in most reservoir time-lapse modeling studies. In this process, the initial pore fluid of the reservoir rock is substituted by a new fluid to calculate the new properties of the saturated rock. These properties can then be used in the time-lapse modeling algorithms to generate synthetic data useful in reservoir monitoring studies. In CCS projects, the in situ fluids that are usually either brine or oil, are partially replaced by CO₂. Since CO₂ has lower incompressibility than the reservoir fluids, the bulk modulus of the saturated rock will decrease to some extent after the initial reservoir fluids are replaced by CO₂. These changes in elastic properties can be detected in seismic data and used to track CO₂ in the target formation. In this chapter the available data from the quest project are presented, and the in-situ properties of the storage formation, BCS, are extracted from the data. This is followed by a review of the Gassmann (1951) method and the fluid substitution modeling for the Quest project using his method. The calculated properties in this chapter are then used for numerical modeling in the later chapters.

3.2 Well logs

The numerical models used in this thesis are all based on the data from well SCL-8-19-59-20W4 which is also called "Radway well". These well data were received from Shell Canada Limited in summer 2012. The location of this well is within the Thorhild County area where the candidate injection wells are also located (Figures 2.4 and 2.2). A baseline 3D seismic survey has been acquired in the area as well. However, in the work described here there was access

only to the well data, and the numerical models used in this dissertation are based solely on the logs from this well. The available logs are shown in Figure 3.1. There are 5 tracks that show density, gamma-ray, P-wave velocity, S-wave velocity and V_p/V_s ratio. Some of the formation tops are marked in this figure as well. The Upper and Lower Lotsberg Salts show a significant decrease in density due to the low density of the salt. The base of the BCS, which is the top of the Precambrian Basement, is distinguished by the sudden increase in the P-wave velocity and density at the bottom of the well. Since the Precambrian Basement mainly consists of granite, the density and the seismic velocity at this depth is high. The top of the BCS could not be easily recognized from the density and velocity logs due to low contrast with the overlying layer that is the LMS. However, in the gamma ray log, the BCS shows notably low values that is indication of higher sand content compared to upper layers. The thickness identified of the BCS in this log is around 50 m. The average rock properties of the BCS was then extracted from these logs. These properties are listed in Table 3.1.

Table 3.1: Average physical properties of the BCS extracted from the well logs

Property	BCS	Standard Deviation
ρ	2390 (kg/m^3)	41 (kg/m^3)
V_p	4100 (m/s)	103 (m/s)
V_s	2350 (m/s)	121(m/s)

3.3 Gassmann Fluid Substitution

Fluid substitution modeling is a process in which the fluid content of a saturated rock is theoretically substituted by a new fluid mixture and the physical properties of the new saturated rock are calculated. The Gassmann (1951) method is commonly employed for fluid substitution modeling. In this method the bulk modulus of a saturated rock is calculated based on the properties of the pore fluid and the dry rock frame. In this chapter this method is used to calculate the properties of the Basal Cambrian Sands (BCS) in the Quest project after injecting

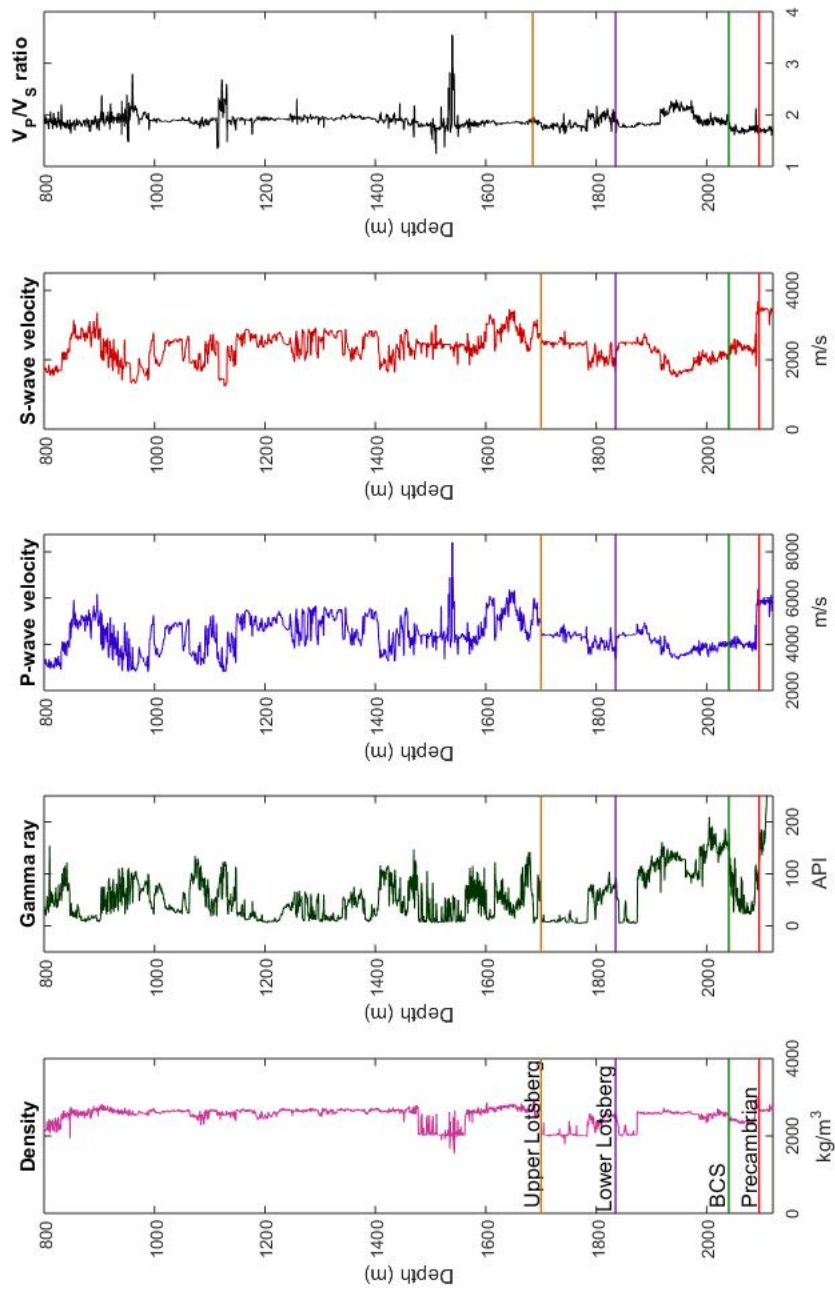


Figure 3.1: Data from well SCL- 8-19-59-20W4 and some of the horizons in the zone of interest. Respectively from bottom to top the tracks show the density, gamma-ray, P-wave velocity, S-wave velocity, and V_p/V_s ratio.

CO₂. The calculated properties are needed for the time-lapse wave equation modeling later in this dissertation.

The Gassmann formulation was established under several assumptions, and it is therefore valid only for homogeneous isotropic materials with connected pore space. Therefore in the case that the rock is anisotropic, or consists of several minerals with highly contrasting elastic properties, the Gassmann model is no longer valid (Smith et al., 2003). The BCS is mostly composed of sandstone and could be assumed homogeneous and isotropic. Therefore, Gassmann fluid substitution could be carried out for BCS, with efficiency.

3.3.1 Theory

Gassmann (1951) defined the bulk modulus of the fluid saturated rock as a function of porosity and the bulk moduli of the rock matrix (K_M), the fluid (K_f) and the dry rock frame (K_{Dry}):

$$K_{sat} = K_{Dry} + \frac{\left(1 - \frac{K_{Dry}}{K_M}\right)^2}{\left(\frac{\phi}{K_f} + \frac{(1-\phi)}{K_M} - \frac{K_{Dry}}{K_M^2}\right)}. \quad (3.1)$$

This formula has been used extensively for fluid substitution modeling in the recent decades. All parameters on the right hand side of the equation are usually known, except the bulk modulus of the dry rock frame. This parameter, which is the bulk modulus of the drained rock, could be estimated using one of the following methods (Smith et al., 2003): 1) By measuring the velocity in the rock physics lab when the rock is drained under controlled conditions. A very small amount of moisture must exist in the rock when the velocity is being measured to avoid errors. 2) Using empirical relationships or effective medium theory (Spencer et al., 1994; Wang et al., 2001). 3) Calculating directly from log data using Equation 3.1 and solving for K_{Dry} . Since K_{Dry} remains unchanged regardless of the fluid content of the rock, this parameter could be calculated using the bulk modulus of the initially saturated rock K_{sat_0} and the bulk modulus of the initial fluid K_{f_0} . The later method was used in this work to estimate the bulk modulus of the

dry frame from the log data. Therefore, solving Equation 3.1 for K_{Dry} gives:

$$K_{Dry} = \frac{K_{sat_0} \left(\frac{\phi K_M}{K_{f_0}} + 1 - \phi \right) - K_M}{\frac{\phi K_M}{K_{f_0}} + \frac{K_{sat_0}}{K_M} - 1 - \phi}, \quad (3.2)$$

Once K_{Dry} is evaluated, K_{sat} can be calculated for the rock saturated with any new fluids from Equation 3.1.

3.3.2 Work flow

To perform fluid substitution modeling for the Basal Cambrian Sands (BCS) based on Equations 3.1 and 3.2, the physical properties of the Fluid, the matrix, and the saturated rock are required. These properties are:

ρ_{f_0} : density of the initial fluid;

ρ_M : density of the Rock Matrix;

ρ_{sat_0} : density of the initially saturated rock;

K_{f_0} : bulk modulus of the initial fluid;

K_M : bulk modulus of the matrix;

K_{sat_0} : bulk modulus of the initially saturated rock;

ϕ : Porosity of the rock;

and the following properties can be calculated during the fluid substitution:

ρ_f : density of the new fluid mixture;

ρ_{sat} : density of the new saturated rock;

K_f : bulk modulus of the new fluid mixture;

K_{Dry} : bulk modulus of the dry rock frame;

K_{sat} : bulk modulus of the new saturated rock.

The purpose of the fluid substitution modeling was to theoretically replace some of the brine with CO₂ and calculate the new physical properties of the BCS from after substitution. Therefore, two scenarios are considered: one is the baseline scenario in which the fluid content

of the BCS is 100 % brine, and the second one is the monitor scenario where the BCS is saturated with a mixture of brine and CO₂. Here the procedure of evaluating the required parameters is presented followed by the fluid substitution results for BCS.

3.3.2.1 Properties of the initially saturated rock

For the Quest project, some properties of the initially saturated rock were extracted from the well logs. These parameters are the density (ρ_{sat_0}), the P-wave velocity (V_{P_0}), and the S-wave velocity (V_{S_0}), which are also listed in Table 3.1. From the definition of the seismic velocities we have:

$$\mu = \rho_{sat_0} V_{S_0}^2, \quad (3.3)$$

$$K_{sat_0} = \rho_{sat_0} V_{P_0}^2 - 4\mu/3, \quad (3.4)$$

where μ is the shear modulus of the rock. This parameter is assumed to be independent of the fluid content and remains constant during the fluid substitution. Therefore, the calculated μ from Equation 3.3 could be used throughout the fluid substitution procedure regardless of the changes in the pore fluid. The calculated values from Equations 3.3 and 3.4 for BCS were $\mu = 13.20 \text{ GPa}$, and $K_{sat_0} = 22.00 \text{ GPa}$.

3.3.2.2 Fluid properties

The fluid properties had to be calculated empirically due to the lack of information about the fluid properties of the BCS. To evaluate the bulk modulus and the density of the brine and CO₂, Batzle and Wang equations of state (Batzle and Wang, 1992) were used. For this purpose the CREWES online fluid property calculator was employed, which is based on Batzle-Wang method. The goal was to calculate the properties of CO₂ and brine at the conditions of the BCS aquifer. The temperature and pore pressure at BCS were needed as inputs of the software. Since this information were not available, the geothermal and hydrostatic gradients were used, respectively, to calculate the temperature and the pressure at the BCS. The temperature T at the

depth of z , is given by:

$$T(z) = G * z + T(z_0) \quad (3.5)$$

where $T(z_0)$ is the temperature at the surface, that was assumed to be 15°C . Moreover, G is the geothermal gradient that in Alberta is about $27^\circ\text{C}/\text{km}$ Hitchon (1984). The temperature at BCS was found to be 70°C .

Moreover, the pressure P at the depth of z is:

$$P(z) = H * z, \quad (3.6)$$

where H is the hydrostatic pressure gradient that is $9.792\text{ KPa}/\text{m}$. The average depth of 2050 m was considered for BCS, and the pressure obtained for this depth was 20 MPa (200 bar). In the normal temperature and pressure, CO_2 exists in the gaseous phase. Figure 3.2 shows the phase diagram of CO_2 as a function of temperature and pressure. The physical state of CO_2 changes by temperature and pressure. For example, at low temperatures CO_2 is solid anywhere above the sublimation line and it turns directly from solid to gas along this line without becoming liquid. Furthermore, above the critical point ($T=31.1^\circ\text{C}$, $P=73.9\text{ bar}$) CO_2 enters the supercritical zone. Under supercritical conditions, CO_2 has a density close to that of the fluid state but it expands to fill its container like a gas.

Based on the phase diagram, in the temperature and pressure of the BCS ($T=70^\circ\text{C}$, $P=200\text{ bar}$), CO_2 will be in supercritical phase. By inserting these values into the CREWES fluid property calculator, the bulk modulus and density of CO_2 and brine at these conditions were evaluated. These properties are summarized in Table 3.2.

Table 3.2: Estimated properties of Brine and CO_2 at the BCS conditions

Fluid	Bulk Modulus	Density	P-Wave Velocity
CO_2	$0.08 \times 10^9\text{ Pa}$	$625\text{ kg}/\text{m}^3$	$360\text{ m}/\text{s}$
Brine	$3.8 \times 10^9\text{ Pa}$	$1230\text{ kg}/\text{m}^3$	$1770\text{ m}/\text{s}$

The next step was to calculate the properties of the mixture of brine and CO₂. Since Gassmann assumes the pore fluid is homogeneous, the bulk modulus and the density of the fluid mixture must be calculated from those of the individual fluids in the mixture. The bulk modulus of the fluid mixture could be calculated using the Reuss average approach (Smith et al., 2003):

$$K_f = \left[\sum_{i=1}^n \frac{S_i}{K_i} \right]^{-1} \quad (3.7)$$

where S_i and K_i are respectively the saturation and the bulk modulus of each fluid phase in the mixture, with n being the number of the fluid phases. Therefore, this formula could be used for any mixture of multiple fluids. BCS is assumed to have only two phases after injection: the brine, and the CO₂. Then we have:

$$K_f = \left[\frac{S_{CO_2}}{K_{CO_2}} + \frac{(1 - S_{CO_2})}{K_{brine}} \right]^{-1}, \quad (3.8)$$

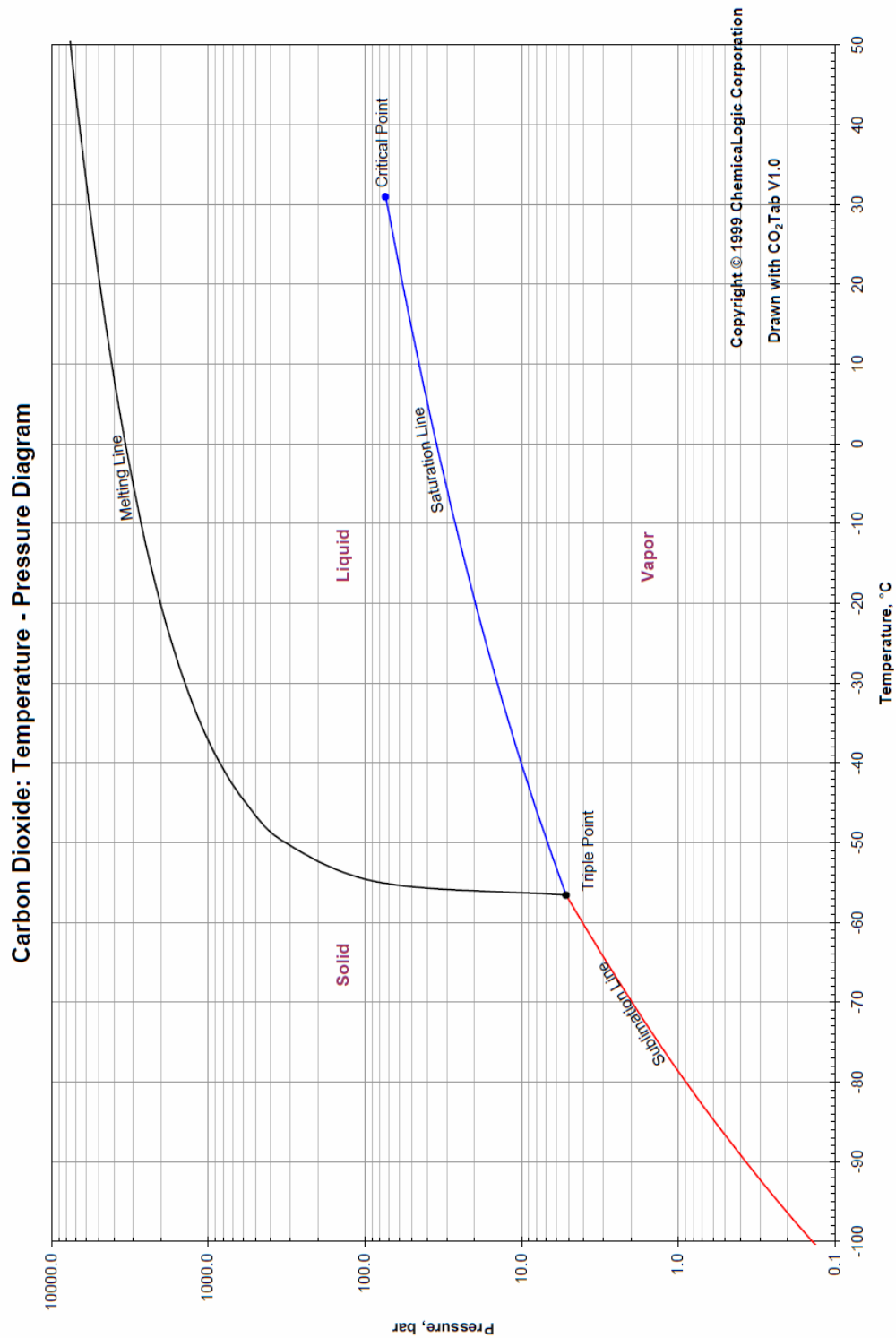
where S_{CO_2} is the saturation of CO₂, and consequently, $(1 - S_{CO_2})$ is the saturation of brine. K_{brine} and K_{CO_2} are, respectively, the bulk moduli of brine and CO₂. To understand how the bulk modulus of the fluid mixture, K_f , changes by CO₂ saturation, this modulus was calculated for different values of S_{CO_2} ranging from zero to 1. The calculated K_f is shown in Figure 3.3 a. There is a sudden decrease in the bulk modulus of the mixture below $S_{CO_2} = 0.2$, and only subtle changes at greater CO₂ saturations. The density of the fluid mixture are simply calculated from a volumetric mix of the fluids:

$$\rho_f = \sum_{i=1}^n S_i \rho_i \quad (3.9)$$

where ρ_i is the density of each fluid phase in the mixture, and S_i is their saturation. For BCS we have:

$$\rho_f = S_{CO_2} \rho_{CO_2} + (1 - S_{CO_2}) \rho_{brine} \quad (3.10)$$

Figure 3.3 b shows the fluid density of the mixture for different values of CO₂ saturations. The density linearly decreases from the density of the brine, with $S_{CO_2} = 0$ to the density of CO₂, with $S_{CO_2} = 1$.



Copyright © 1999 ChemicalLogic Corporation
 Drawn with CO₂Tab V1.0

Figure 3.2: Carbon dioxide temperature-pressure diagram. The CO₂ is in a supercritical state for when the temperature and the pressure are beyond the critical point. Copyright 1999 Chemical-Logic Corporation.

3.3.2.3 Rock matrix properties

The Reuss average could be used to calculate the bulk modulus of a rock matrix composed of multiple minerals:

$$K_M = \left[\sum_{i=1}^n \frac{F_i}{K_i} \right]^{-1} \quad (3.11)$$

where F_i is the volumetric fraction of each mineral and K_i is their bulk moduli. However, in this study BCS was assumed to be composed of quartz only, with the bulk modulus of $K_M = 38 \text{ GPa}$.

3.3.2.4 Porosity

The porosity is calculated from the relationship between the density of the rock matrix ρ_M , the density of the initial fluid ρ_{f_0} , and the density of the initially saturated rock ρ_{sat_0} :

$$\rho_{sat_0} = \rho_{f_0} \phi + \rho_M (1 - \phi) \quad (3.12)$$

The estimated porosity using these values from the BCS was approximately 18 %.

3.3.3 Results and Discussion

Now that the required parameters for Gassmann modeling are evaluated, the bulk modulus and the density of the saturated rock could be calculated for different values of CO_2 saturation from Gassmann's equation. The results are shown in Figure 3.3 c-d. The density of the fluid decreases linearly with increasing CO_2 saturation and as a result, the density of the saturated rock follows the same trend. The bulk modulus of the saturated rock however has a trend similar to that of the the fluid bulk modulus. Using Equations 3.3 and 3.4 the shear and compressional seismic velocities, V_S and V_P are then calculated. Figure 3.4 shows the percent change in both velocities versus CO_2 saturation.

The P-wave velocity, V_P , decreases sharply once CO_2 is added to the fluid content, and starts to slowly increase when the CO_2 saturation passes 30–40 %. The P-wave velocity depends on the bulk modulus and the inverse of the density. It is observed that the effect of density begins

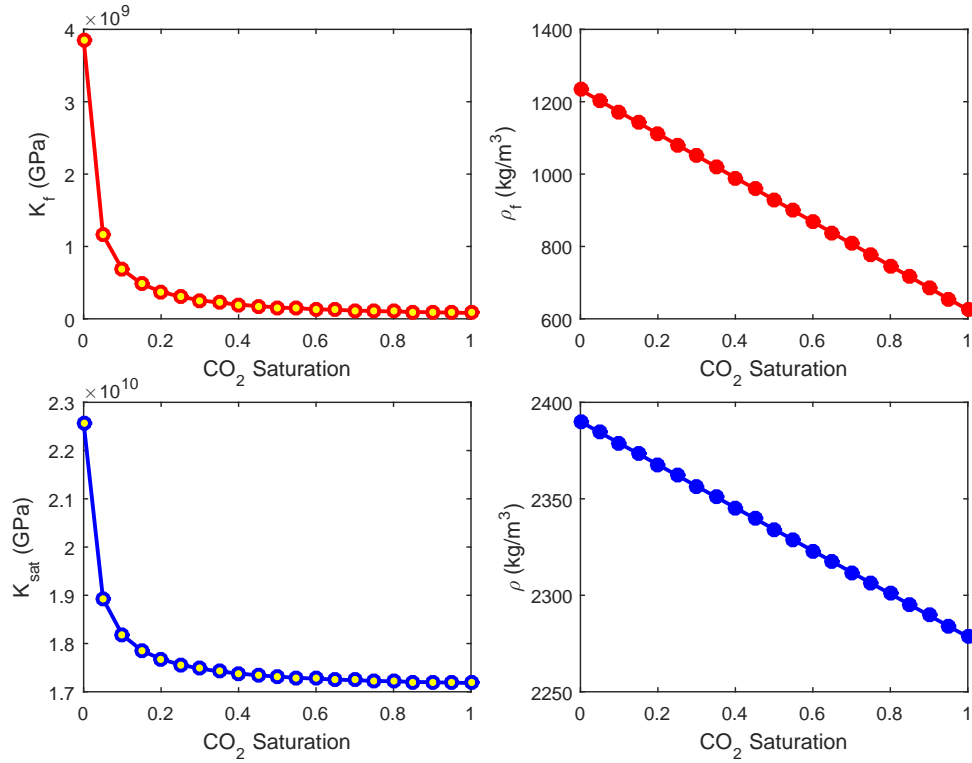


Figure 3.3: The physical properties of the fluid and the saturated rock at BCS after fluid substitution as a function of CO₂ saturation. a) The bulk modulus of the fluid mixture, b) the density of the fluid mixture, c) the bulk modulus of the rock saturated with new fluid mixture, d) the density of the new saturated rock

to dominate the bulk modulus beyond $S_{CO_2}=30\%$. Therefore, the velocity starts to increase to some extent after this point. The S-wave velocity, V_S , only depends on the inverse of the density and thus increases linearly with CO₂ saturation. The maximum decrease in the V_P is 6%, and the maximum increase in the V_S is 1.5%.

As previously mentioned, two scenarios are considered for time-lapse modeling. The pore fluid is assumed to be 100 % brine for the baseline scenario, and a mixture with 40 % CO₂ and 60 % brine. The CO₂ saturation 40% was chosen because it is a typical value for saturation in CCS projects. The properties of BCS for the baseline and monitor scenarios are listed in Table 3.3, respectively represented by BCS_{Base} and BCS_{Mon} . Later in this dissertation, these properties are used to define numerical models for wave propagation modeling.

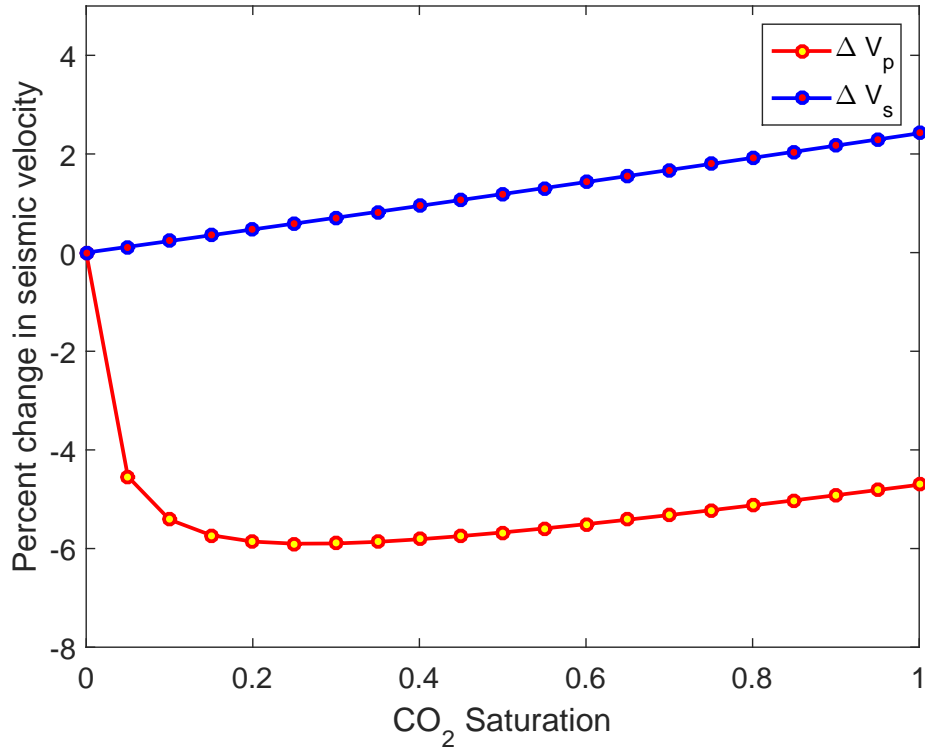


Figure 3.4: Percent change in P-wave and S-wave velocities of the new saturated rock versus the CO₂ saturation.

Table 3.3: Physical properties of BCS for baseline and monitor scenarios

Property	BCS _{Base}	BCS _{Mon}
ρ_M	2650 kg/m ³	2650 kg/m ³
ρ_f	1230 kg/m ³	1050 kg/m ³
ρ_{sat}	2390 kg/m ³	2350 kg/m ³
K_M	38.00 × 10 ⁹ Pa	38.00 × 10 ⁹ Pa
K_f	3.8 × 10 ⁹ Pa	0.25 × 10 ⁹ Pa
K_{sat}	22 × 10 ⁹ Pa	17.2 × 10 ⁹ Pa
V_P	4100 m/s	3850 m/s
V_S	2350 m/s	2365 m/s
ϕ	18%	18%

3.4 Summary

Gassmann fluid substitution modeling was carried out to evaluate the rock and fluid properties of the Basal Cambrian Sands after injecting CO₂. The compressional velocity decreased sharply for CO₂ saturation values below 30% and increased insignificantly past this point. Additionally, the shear wave velocity increased slightly with increasing CO₂ saturation with a linear trend. The properties of the fluid and the saturated rock are essential for the poroelastic wave equation modeling which is the main focus of this thesis. These properties were calculated for the baseline and monitor scenarios and will be used in our numerical models in the next chapters.

Chapter 4

Biot's Theory

4.1 Introduction

Time-lapse seismic techniques are used extensively in the oil and gas industry for monitoring and planning purposes. To ensure that the seismic methods are capable of detecting the changes in physical properties of the reservoir, numerical modeling is usually carried out. Most of the modeling algorithms are based on the assumption that the Earth is composed of solid elastic layers. However, in reality reservoirs are porous rocks that are saturated with fluids. Wave propagation in porous media has attracted attention in the last fifty years, since Maurice Biot established his theory on poroelasticity (Biot, 1962). Based on his definition, a poroelastic medium is composed of two phases. One phase is the porous elastic solid frame, and the other is the compressible viscous pore fluid that can move within the pore space. The relative movement of the fluid with respect to the solid generates a "slow P-wave" that travels with a velocity close to the wave velocity in the fluid. The wave-induced fluid flow leads to energy dissipation in the medium that is often neglected in elastic modeling algorithms. Biot's theory could be therefore, also used in modeling algorithms for cases in which fluid properties of the reservoir change through time. A good example for such projects is Carbon Capture and Storage (CCS) projects, where CO₂ is injected into deep geological formations for permanent storage.

Some studies show that the presence of the slow P-wave in the fluid saturated media may change the seismic wave-field noticeably (Gurevich et al., 1997; Shapiro and Müller, 1999). At seismic frequencies the viscosity effects dominate the internal effects (Carcione and Quiroga-Goode, 1995; Jianfeng, 1999), therefore the slow P-wave becomes diffusive and dissipates quickly in the medium. However, in the case of zero fluid viscosity, the slow P-wave become a traveling wave at all ranges of frequency (Carcione et al., 2010).

There have been extensive numerical studies, including the finite-difference method, to simulate the wave motion in a poroelastic media since the fluid content of the rock is always of interest in reservoir characterization and monitoring (Carcione et al., 2010). For example, Zhu and McMechan (1991) used a standard finite-difference algorithm based on particle displacements, and Dai et al. (1995) employed a MacCormack finite-difference scheme. Others implemented staggered-grid velocity-stress scheme for solving the wave equations (Zeng et al., 2001; Wang et al., 2003; Aldridge et al., 2004; Sheen et al., 2006). Furthermore, Jianfeng (1999) developed a quadrangle-grid velocity-stress finite-difference which was based on a non-orthogonal grid. Zhang's scheme aimed to better handle the curved interfaces and surface topography.

Having an effective boundary condition is essential in any finite-difference wave modeling algorithm to avoid artificial reflections from the computational boundaries. The perfectly matched layer (PML) was introduced by Berenger (1994) for electromagnetic waves and later used by Chew and Liu (1996) for elastic and Zeng et al. (2001) for poroelastic media. This layer is defined so that the reflection coefficient at the computational boundary is zero at all angles and the outgoing waves are absorbed as much as possible. In this thesis the PML boundary condition is implemented on a staggered grid velocity-stress finite-difference algorithm to solve the wave equation in poroelastic media. This finite-difference scheme is similar to the one used by Zeng et al. (2001) and Sheen et al. (2006). However, the numerical examples used in this dissertation are for a CO₂ storage project, and the algorithm is examined for possible monitoring purposes in these types of projects. Therefore, a model-based poroelastic time-lapse study was carried out in this thesis, and the results were compared with the results from a more simplistic elastic algorithm.

4.1.1 Stress-strain relations

Maurice Biot was the first to propose a theory of poroelasticity (Biot, 1962). He made the following assumptions to derive the equations of motion in the porous media: (1) the rock frame is assumed to be elastic and isotropic; (2) the pores are connected so that the fluid can

travel through the pore spaces; (3) the seismic wavelength is much larger than the average pore size; and (4) the deformations are small enough that the mechanical processes become linear (Dai et al., 1995).

Consider a rock cube with a unit size from within a porous rock saturated with fluid. This cube could be considered statically isotropic, if for all cross sections of the rock, the ratio of the pore area to the solid area is constant. It is also assumed that the pore size is much smaller than the cube size and much smaller than the seismic wavelength. Any force that is applied to a face of this cube, would be divided into two parts: one is the average stress applied on the solid rock frame; and the other is a hydrostatic pressure applied on the fluid content of the rock. The applied stress is therefore divided into two parts. One is the force acting on the solid frame of the rock that is denoted by the following tensor:

$$\begin{bmatrix} \tau_{xx} & \tau_{xy} & \tau_{xz} \\ \tau_{yx} & \tau_{yy} & \tau_{yz} \\ \tau_{zx} & \tau_{zy} & \tau_{zz} \end{bmatrix}, \quad (4.1)$$

The other part of the total stress is the force acting on the fluid content of the rock, that is (Biot, 1956):

$$\begin{bmatrix} S & 0 & 0 \\ 0 & S & 0 \\ 0 & 0 & S \end{bmatrix}, \quad (4.2)$$

where S is a function of the fluid pressure P and porosity ϕ :

$$S = -\phi P, \quad (4.3)$$

The strain generated in the solid is represented by the following tensor:

$$\begin{bmatrix} e_{xx} & e_{xy} & e_{xz} \\ e_{yx} & e_{yy} & e_{yz} \\ e_{zx} & e_{zy} & e_{zz} \end{bmatrix}, \quad (4.4)$$

with

$$e_{ij} = \frac{1}{2}(v_{i,j} + v_{j,i}), \quad (4.5)$$

where $\vec{v} = [v_x, v_y, v_z]$ is the particle displacement vector of the solid, and the fluid particle displacement vector is $\vec{u} = [u_x, u_y, u_z]$, where $i, j = x, y, z$. The comma notation is a convenient way of showing spatial differentiation. For example:

$$A_{,j} = \frac{dA}{dx_j} \quad (4.6)$$

Therefore, the amount of the fluid that moves in and out of the unit cube is:

$$\zeta = -\text{div}(\vec{u} - \vec{v}), \quad (4.7)$$

where $\vec{u} - \vec{v}$ is the relative particle displacement of the fluid with respect to the solid and is denoted by \vec{w} . Accordingly:

$$\zeta = -w_{k,k} = -\left[\frac{\partial w_x}{\partial x} + \frac{\partial w_y}{\partial y} + \frac{\partial w_z}{\partial z}\right], \quad (4.8)$$

Biot (1962) showed that for an isotropic poroelastic medium the linear relationship between the stress and strain is:

$$\begin{aligned} \tau_{xx} &= 2\mu e_{xx} + \lambda e - \alpha M \zeta, \\ \tau_{yy} &= 2\mu e_{yy} + \lambda e - \alpha M \zeta, \\ \tau_{zz} &= 2\mu e_{zz} + \lambda e - \alpha M \zeta, \\ \tau_{xz} &= 2\mu e_{xz}, \\ \tau_{xy} &= 2\mu e_{xy}, \\ \tau_{yz} &= 2\mu e_{yz}, \\ P &= -\alpha M e + M \zeta, \end{aligned} \quad (4.9)$$

with

$$e = e_{xx} + e_{yy} + e_{zz}, \quad (4.10)$$

where λ is the the bulk Lamé's constant and μ is the shear modulus. The presence of the fluid does not impact the shear modulus of the saturated rock, therefore the shear moduli of the drained rock and of the saturated rock are the same. The parameter α is the Biot's coefficient, defined by $1 - \frac{K_{Dry}}{K_M}$, with K_{Dry} being the bulk modulus of the drained rock, and K_M being the bulk modulus of the solid material (or the mineral). The constant M is the measure of coupling between the fluid and the rock frame, defined by $[\frac{\phi}{K_f} + \frac{(\alpha-\phi)}{K_M}]^{-1}$. Equations 4.9 show that the fluid flow contributes to the normal stress acting on the rock frame. In addition, the normal solid stress e plays a role in the fluid pressure P . The equations 4.9 could be shown in a more compact way by using index notation:

$$\tau_{ij} = \mu(v_{i,j} + v_{j,i}) + \delta_{ij}(\lambda v_{k,k} - \alpha M w_{k,k}), \quad (4.11)$$

$$P = -\alpha M v_{k,k} + M w_{k,k}, \quad (4.12)$$

where δ_{ij} is the Kronecker delta in which:

$$\delta_{ij} = \begin{cases} 1, & \text{if } i = j, \\ 0, & \text{if } i \neq j, \end{cases} \quad (4.13)$$

and

$$v_{k,k} = \frac{\partial v_x}{\partial x} + \frac{\partial v_y}{\partial y} + \frac{\partial v_z}{\partial z}, \text{ etc.} \quad (4.14)$$

$$v_{i,j} = \frac{\partial v_i}{\partial x_j}, \quad (4.15)$$

Equations 4.11 to 4.12 are the stress-strain relations for a poroelastic medium. To construct a numerical modeling algorithm for poroelastic media, which is the purpose of this thesis, the dynamic equations are also required. The dynamic equations describe the relation between the displacements of the solid and the fluid with the solid stresses and the fluid pressure. In the next section we review Biot's dynamic equations.

4.1.2 Dynamic equations

Biot derived the dynamic equations based on the Lagrangian definition for two cases, with and without friction. Here we review the case with friction which is the more general one. It is assumed that the friction is caused by the relative movement of the fluid with respect to the rock frame. The dissipation function D is then defined as a function of relative fluid particle velocity that is the time derivative of the relative fluid displacement:

$$2D = b [W_x^2 + W_y^2 + W_z^2], \quad (4.16)$$

$$W_i = \frac{\partial w_i}{\partial t},$$

The factor b represents resistive damping due to the relative movement of the fluid with respect to the solid, where $b = \eta/\kappa$ with η and κ being the fluid viscosity and the rock permeability, respectively (Norris, 1985). If the total force acting on the saturated rock unit cube in the direction of x_i is denoted by f_i , and the one acting on the fluid is denoted by F_i , from the Lagrange's equations we have:

$$\frac{d}{dt} \left(\frac{\partial T}{\partial V_i} \right) = f_i, \quad (4.17)$$

$$\frac{d}{dt} \left(\frac{\partial T}{\partial W_i} \right) + \frac{\partial D}{\partial W_i} = F_i, \quad (4.18)$$

where V_i is the solid particle velocity written as $\frac{\partial v_i}{\partial t}$. Moreover, T is the kinetic energy for the total volume of the saturated rock, defined as:

$$2T = \rho(V_x^2 + V_y^2 + V_z^2) + 2\rho_f(V_x W_x + V_y W_y + V_z W_z) + m(W_x^2 + W_y^2 + W_z^2), \quad (4.19)$$

where ρ is the density of the saturated written as a function of the density of the fluid ρ_f , the density of the solid frame ρ_M , and the porosity ϕ :

$$\rho = \phi\rho_f + (1 - \phi)\rho_M, \quad (4.20)$$

The parameter m is the fluid's effective density, defines as $\frac{T\rho_f}{\phi}$, where T is the tortuosity that is a function of the pore shape. Furthermore, we explicitly have:

$$f_i = \rho \frac{\partial V_i}{\partial t} + \rho_f \frac{\partial W_i}{\partial t}, \quad (4.21)$$

$$F_i = \rho_f \frac{\partial V_i}{\partial t} + m \frac{\partial W_i}{\partial t} + bW_i, \quad (4.22)$$

On the other hand, the forces are defined as stress gradients:

$$f_i = \frac{\partial \tau_{ij}}{\partial x_j} \quad (4.23)$$

$$F_i = \frac{\partial P}{\partial x_i} \quad (4.24)$$

Thus, Equations 4.21 and 4.22 become:

$$\frac{\partial \tau_{ij}}{\partial x_j} = \rho \frac{\partial V_i}{\partial t} + \rho_f \frac{\partial W_i}{\partial t}, \quad (4.25)$$

$$\frac{\partial P}{\partial x_j} = \rho_f \frac{\partial V_i}{\partial t} + m \frac{\partial W_i}{\partial t} + bW_i, \quad (4.26)$$

By rearranging these two equations, a set of velocity-stress relations can be obtained:

$$(m\rho - \rho_f^2) \frac{\partial V_i}{\partial t} = m \frac{\partial \tau_{ij}}{\partial x_j} + \rho_f \frac{\partial P}{\partial x_i} + \rho_f bW_i, \quad (4.27)$$

$$(m\rho - \rho_f^2) \frac{\partial W_i}{\partial t} = -\rho_f \frac{\partial \tau_{ij}}{\partial x_j} - \rho \frac{\partial P}{\partial x_i} - \rho bW_i, \quad (4.28)$$

In order to develop a staggered-grid finite-difference program, we need to write the partial differential equations in a velocity-stress formulation. The Equations 4.27 and 4.28 are already in that form. The rest of equations are obtained by taking a time derivative from both sides of Equations 4.11 and 4.12. Finally, Biot's velocity-stress partial differential equations are:

$$\frac{\partial V_i}{\partial t} = A \frac{\partial \tau_{ij}}{\partial x_j} - B \left(\frac{\partial P}{\partial x_i} + b W_i \right), \quad (4.29)$$

$$\frac{\partial W_i}{\partial t} = B \frac{\partial \tau_{ij}}{\partial x_j} + C \left(\frac{\partial P}{\partial x_i} + b W_i \right), \quad (4.30)$$

$$\frac{\partial \tau_{ij}}{\partial t} = \mu \left(\frac{\partial V_i}{\partial x_j} + \frac{\partial V_j}{\partial x_i} \right) + \delta_{ij} \left(\lambda \frac{\partial V_k}{\partial x_k} - \alpha M \frac{\partial W_k}{\partial x_k} \right), \quad (4.31)$$

$$\frac{\partial P}{\partial t} = -\alpha M \frac{\partial V_k}{\partial x_k} + M \frac{\partial W_k}{\partial x_k}, \quad (4.32)$$

where all symbols are defined in Table 4.1.

4.1.3 Wave equations in 2D case

In the 2D case, where the wave travels only in the x-z plane and $i, j = x, z$, Equations 4.28 to 4.31 make a set of 8 coupled equations:

$$\frac{\partial V_z}{\partial t} = A\left(\frac{\partial \tau_{xz}}{\partial x} + \frac{\partial \tau_{zz}}{\partial z}\right) - B\left(\frac{\partial P}{\partial z} + bW_z\right), \quad (4.33)$$

$$\frac{\partial V_x}{\partial t} = A\left(\frac{\partial \tau_{xx}}{\partial x} + \frac{\partial \tau_{xz}}{\partial z}\right) - B\left(\frac{\partial P}{\partial x} + bW_x\right), \quad (4.34)$$

$$\frac{\partial W_z}{\partial t} = B\left(\frac{\partial \tau_{xz}}{\partial x} + \frac{\partial \tau_{zz}}{\partial z}\right) + C\left(\frac{\partial P}{\partial z} + bW_z\right), \quad (4.35)$$

$$\frac{\partial W_x}{\partial t} = B\left(\frac{\partial \tau_{xx}}{\partial x} + \frac{\partial \tau_{xz}}{\partial z}\right) + C\left(\frac{\partial P}{\partial x} + bW_x\right), \quad (4.36)$$

$$\frac{\partial P}{\partial t} = -\alpha M\left(\frac{\partial V_x}{\partial x} + \frac{\partial V_z}{\partial z}\right) - M\left(\frac{\partial W_x}{\partial x} + \frac{\partial W_z}{\partial z}\right), \quad (4.37)$$

$$\frac{\partial \tau_{xx}}{\partial t} = (2\mu + \lambda_c)\frac{\partial V_x}{\partial x} + \lambda_c\frac{\partial V_z}{\partial z} + \alpha M\left(\frac{\partial W_x}{\partial x} + \frac{\partial W_z}{\partial z}\right), \quad (4.38)$$

$$\frac{\partial \tau_{zz}}{\partial t} = (2\mu + \lambda_c)\frac{\partial V_z}{\partial z} + \lambda_c\frac{\partial V_x}{\partial x} + \alpha M\left(\frac{\partial W_x}{\partial x} + \frac{\partial W_z}{\partial z}\right), \quad (4.39)$$

$$\frac{\partial \tau_{xz}}{\partial t} = \mu\left(\frac{\partial V_z}{\partial x} + \frac{\partial V_x}{\partial z}\right), \quad (4.40)$$

These equations will be used for numerical modeling. However, the equations need to be discretized in order to be solved numerically in a computer program. The quantities on the left hand side of these equations are the unknowns that will be calculated in the modeling process. The model parameters, such as fluid and solid properties are incorporated in the right hand side of these equations. The discrete form of these equations and details about the numerical simulations will be explained in the next chapter.

4.2 Perfectly Matched Layers

One of the limitations of numerical modeling is that unlike in the real Earth, the computational domain is finite. Therefore, a wave hitting the grid boundaries reflects back into the medium. In order to overcome this problem a boundary condition is needed at the edges of the geological

model to eliminate the undesired reflections. As discussed in the introduction of this chapter, the PML boundary condition is a popular method in finite-difference modeling for absorbing the outgoing waves at the edges. In order to employ this method, the computational grid is divided into two regions: the internal region, where the Equations 4.33 to 4.40 are solved; and the PML region, where the damping factors are added to these equations so that the outgoing waves dissipate very quickly (Figure 4.1).

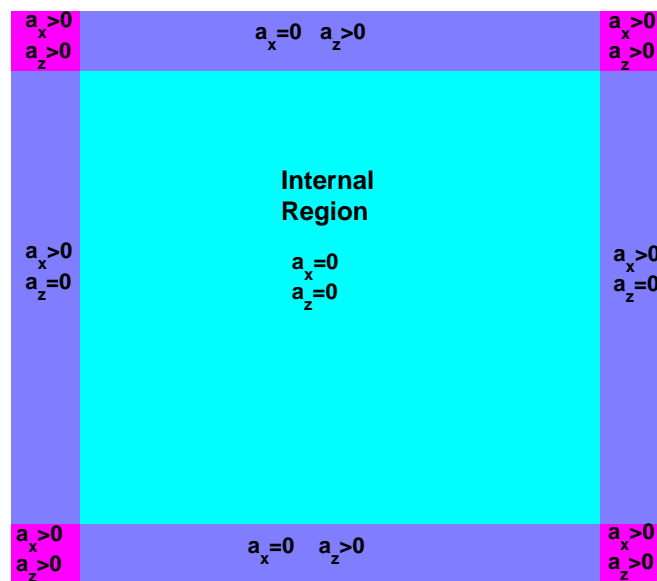


Figure 4.1: Schematic view of the PML region and how the damping factors a_x and a_z are defined in two directions of x and z .

The process of defining the PML equations for any sets of differential equations is accomplished by replacing the regular coordinate variables in the frequency domain by the complex stretched variables, and also splitting the velocity and stress fields before transforming back to time domain. The complex stretched variables are defined as (Chew and Liu, 1996; Sheen et al., 2006):

$$\tilde{\xi} = \int_0^{\xi} S_{\xi}(\xi) d\xi, \quad S_{\xi}(\xi) = 1 - \frac{a_{\xi}(\xi)}{i\omega} \quad i = 1, 2, 3; \quad (4.41)$$

Where $\xi = x, z$ and a_{ξ} is the damping factor in ξ direction, and ω is the temporal frequency.

Considering the 2D case, equation 4.33 after transforming to the frequency domain becomes:

$$(-i\omega)\hat{V}_z = A \left(\frac{\partial \hat{\tau}_{xz}}{\partial \tilde{x}} + \frac{\partial \hat{\tau}_{zz}}{\partial \tilde{z}} \right) - B \left(\frac{\partial \hat{P}}{\partial \tilde{z}} + b\hat{W}_x \right), \quad (4.42)$$

From the definition in Equation 4.40 we can use $\partial/\partial\tilde{\xi} = (\frac{1}{S_{\xi}})\partial/\partial\xi$ to replace the complex variable $\tilde{\xi}$ by the regular coordinate variable ξ . For simplicity of the equations, the velocities and the stresses are split into x and z components. For example: $V_x = V_x^x + V_x^z$ and $V_z = V_z^x + V_z^z$

and . Equation 4.33 after change of variables and splitting becomes:

$$(-i\omega)\hat{V}_z^x = \left(\frac{A}{S_x} \right) \left(\frac{\partial \hat{\tau}_{xz}}{\partial x} \right) - B b\hat{W}_z^x, \quad (4.43)$$

and

$$(-i\omega)\hat{V}_z^z = \left(\frac{A}{S_z} \right) \left(\frac{\partial \hat{\tau}_{zz}}{\partial z} \right) - \left(\frac{B}{S_z} \right) \frac{\partial \hat{P}}{\partial z} - B b\hat{W}_z^z. \quad (4.44)$$

By transforming these equations back to the time domain we have:

$$\left(\frac{\partial}{\partial t} + a_x \right) V_z^x = A \frac{\partial \tau_{xz}}{\partial x} - B b \left(W_z^x + a_x \int_{-\infty}^t W_z^x dt \right), \quad (4.45)$$

$$\left(\frac{\partial}{\partial t} + a_z \right) V_z^z = A \frac{\partial \tau_{zz}}{\partial z} - B \frac{\partial P}{\partial z} - B b \left(W_z^z + a_z \int_0^t W_z^z dt \right), \quad (4.46)$$

where V_x^x and V_x^z are the split fields of V_x . The damping factors a_x and a_z are defined based on the location of the calculated point on the grid. The same approach could be used to obtain the rest of the equations. Then we have:

$$\left(\frac{\partial}{\partial t} + a_x \right) V_x^x = A \frac{\partial \tau_{xx}}{\partial x} - B \frac{\partial P}{\partial x} - B b \left(W_x^x + a_x \int_0^t W_x^x dt \right), \quad (4.47)$$

$$\left(\frac{\partial}{\partial t} + a_z \right) V_x^z = A \frac{\partial \tau_{xz}}{\partial z} - B b \left(W_x^z + a_z \int_0^t W_x^z dt \right), \quad (4.48)$$

$$\left(\frac{\partial}{\partial t} + a_z\right) W_z^z = B \frac{\partial \tau_{zz}}{\partial z} + C \frac{\partial P}{\partial z} + C b \left(W_z^z + a_z \int_0^t W_z^z dt \right), \quad (4.49)$$

$$\left(\frac{\partial}{\partial t} + a_z\right) W_z^x = B \frac{\partial \tau_{zx}}{\partial x} + C b \left(W_z^x + a_x \int_0^t W_z^x dt \right), \quad (4.50)$$

$$\left(\frac{\partial}{\partial t} + a_z\right) W_x^z = B \frac{\partial \tau_{xz}}{\partial z} + C b \left(W_x^z + a_z \int_0^t W_x^z dt \right), \quad (4.51)$$

$$\left(\frac{\partial}{\partial t} + a_x\right) W_x^x = B \frac{\partial \tau_{xx}}{\partial x} + C \frac{\partial P}{\partial x} + C b \left(W_x^x + a_x \int_0^t W_x^x dt \right), \quad (4.52)$$

$$\left(\frac{\partial}{\partial t} + a_x\right) P^x = -M \left(\alpha \frac{\partial V_x}{\partial x} + \frac{\partial W_x}{\partial x} \right), \quad (4.53)$$

$$\left(\frac{\partial}{\partial t} + a_z\right) P^z = -M \left(\alpha \frac{\partial V_z}{\partial z} + \frac{\partial W_z}{\partial z} \right), \quad (4.54)$$

$$\left(\frac{\partial}{\partial t} + a_z\right) \tau_{xx}^z = \lambda_c \frac{\partial V_z}{\partial z} + \alpha M \frac{\partial W_z}{\partial z}, \quad (4.55)$$

$$\left(\frac{\partial}{\partial t} + a_x\right) \tau_{xx}^x = (2\mu + \lambda_c) \frac{\partial V_x}{\partial x} + \alpha M \frac{\partial W_x}{\partial x}, \quad (4.56)$$

$$\left(\frac{\partial}{\partial t} + a_z\right) \tau_{zz}^z = (2\mu + \lambda_c) \frac{\partial V_z}{\partial z} + \alpha M \frac{\partial W_z}{\partial z}, \quad (4.57)$$

$$\left(\frac{\partial}{\partial t} + a_x\right) \tau_{zz}^x = \lambda_c \frac{\partial V_x}{\partial x} + \alpha M \frac{\partial W_x}{\partial x}, \quad (4.58)$$

$$\left(\frac{\partial}{\partial t} + a_z\right) \tau_{xz}^z = \mu \frac{\partial V_x}{\partial z}, \quad (4.59)$$

$$\left(\frac{\partial}{\partial t} + a_x\right) \tau_{xz}^x = \mu \frac{\partial V_z}{\partial x}. \quad (4.60)$$

The computational grid is then divided into two regions: the internal region and the PML region. The field splitting doubles the number of the differential equations in the PML region, therefore there will be 16 equations to solve (Equations 4.45 to 4.60).

Values of a_x and a_z in the PML region could be either zero or nonzero depending on the location of the grid point. This is shown in Figure 4.1. At the corners of the grid, both a_x and

a_z are nonzero so that the strong reflections generated in these areas are damped properly. The values of a_x and a_z are both zero in the internal grid. Consequently, the Equations 4.33 to 4.40 are solved in this region. Calculation of a_x and a_z in this study is based on the criteria suggested by Collino and Tsogka (2001). For example:

$$a_x = \log \left(\frac{1}{R} \right) \left(\frac{3V_p}{2} \right) \left(\frac{x^2}{L_{PML}^3} \right), \quad (4.61)$$

where R is the theoretical reflection coefficient and x is the distance from the PML boundary. $L_{PML} = n_{PML} \times h$ is the thickness of the PML region, where n_{PML} is the number of the grid points included in the PML boundary, and h is the grid spacing.

4.3 Summary

In this chapter Biot's theory of poroelasticity was reviewed, and the velocity-stress partial differential equations for the poroelastic media were presented. These equations are needed to develop a program for modeling seismic wave propagation in fluid saturated media. Our purpose is to develop a finite-difference modeling program based on Biot's theory, and to examine the developed program for a carbon capture and storage project.

Due to limitations of the computational domain, the numerical models are finite in dimensions. Therefore, the waves that hit the boundaries of the computational grid, reflect back into the medium and generate artifacts. In order to avoid this issue, a Perfectly Matched Layer (PML) boundary is added to the the grid, in which region a different set of equations are solved. The PML equations and also the derivation of these equations were presented in this chapter. This layer acts as a highly attenuating medium and absorbs any outgoing wave. The discrete form of Biot's equations and also the PML equations will be explained in the next chapter.

Table 4.1: List of symbols and their definitions

symbol	discription	
e_{ij}	solid strain	$\frac{1}{2} \left(\frac{\partial v_i}{\partial x_j} + \frac{\partial v_j}{\partial x_i} \right)$
τ_{ij}	solid stress tensor	
\vec{v}	particle displacement of the solid	
\vec{u}	particle displacement of the fluid	
\vec{w}	particle displacement of the fluid with respect to the solid	$\vec{v} - \vec{u}$
ζ	$\nabla \cdot (\vec{v} - \vec{u})$	
μ	shear modulus of the rock	
λ_c	Lame parameter of the saturated rock	
α	Biot's coefficient	$\left(1 - \frac{K_{Dry}}{K_M} \right)$
K_M	bulk modulus of the mineral (the solid)	
K_{Dry}	bulk modulus of the dry rock frame	
K_f	bulk modulus of the fluid	
M	coupling modulus	
P	fluid pressure	
V_i	particle velocity of the solid	$\frac{\partial u_i}{\partial t}$
W_i	particle velocity of the fluid relative to the solid	
ρ_f	density of the fluid	
ρ_M	density of the mineral (the solid)	
ρ_{sat}	density of the saturated rock	$\phi \rho_f + (1 - \phi) \rho_M$
ϕ	porosity	
m	the fluid effective density	$T \rho_f / \phi$
T	tortuosity	
factor b	resistive damping factor	η / κ
κ	permeability	
η	fluid viscosity	
A	Coefficients defined in this thesis for simplicity	$\left(\frac{m}{m\rho - \rho_f^2} \right)$
B		$\left(\frac{-\rho_f}{m\rho - \rho_f^2} \right)$
C		$\left(\frac{-\rho}{m\rho - \rho_f^2} \right)$

Chapter 5

Finite difference modeling

5.1 Introduction

Predicting the observed seismic data is an important step in seismic inversion and interpretation. The finite-difference method is relatively dominant among all other forward modeling methods for several reasons. The main reason is that the finite-difference method calculates the complete waveform and therefore delivers more accurate results. Besides, complex models can be handled effectively using this method. In the finite-difference technique a computational space-time grid is defined and a set of partial differential equations is solved numerically in this grid. Finite-difference algorithms can be also applied in the frequency domain. However, in this thesis we only focus on the finite-difference time domain (FDTD) technique.

In order to solve the wave equations numerically using the finite-difference method, they need to be first discretized. In this work the staggered grid technique was used for discretization, in which some of the wave quantities are defined on a reference grid, and the rest of the quantities are defined on a staggered grid, which is half a grid point shifted from the reference grid. The staggered grid scheme was suggested by Madariaga (1976) and used to model an expanding circular fault. The scheme was based on the particle velocities and stresses in circular coordinates. Virieux (1984, 1986) applied the staggered grid scheme in Cartesian coordinates to model P-SV waves in elastic heterogeneous media. Both Madariaga and Virieux used second order operators in time and space, referred to as $O(\Delta t^2, h^2)$. Levander (1988) developed a staggered grid scheme with a fourth order operator in space i.e. $O(\Delta t^2, h^4)$. In this thesis Levander's scheme was used to develop a finite-difference program for modeling wave propagation in poroelastic media. This scheme and the discretized wave equations are explained in more detail in the beginning of this chapter, and generated snapshots will be shown. Further-

more, The effect of viscosity on the results will be presented, based on the modeled diffusive and non-diffusive modes of the slow P-wave. Finally, at the end of this chapter the boundary conditions and stability of the algorithm are discussed.

5.2 Discretization

In the finite-difference method the wave quantities are calculated on a numerical grid. For this purpose, all quantities need to be assigned to times and spatial locations on a discrete numerical grid. Therefore, the continuous time and locations need to be discretized into a grid through a discretization technique. For example in 2D case where the wave travels in the $x - z$ plane, the reference grid is defined as:

$$\begin{aligned}
 t &= n\Delta t, & n &= 1, 2, 3, \dots, N, \\
 x &= ih, & i &= 1, 2, 3, \dots, I, \\
 z &= jh, & j &= 1, 2, 3, \dots, J,
 \end{aligned} \tag{5.1}$$

where Δt is the time interval or step, and h is the grid size or the space interval. The total time is therefore $N\Delta t$ with N being the number of time steps used in the calculations. The size of the model will be $(Ih) \times (Jh)$, where I and J are the number of the grid points in the x and z directions.

In the time domain finite-difference method, the wave quantities at each time step are calculated based on the quantities calculated in the previous time steps. For example, the quantities at the time of $(n+1)\Delta t$ are calculated using the quantities calculated in the time $n\Delta t$. However, the method that the quantities are calculated based on the other points in the grid depends on the type of discretization technique and the differential operators that are used.

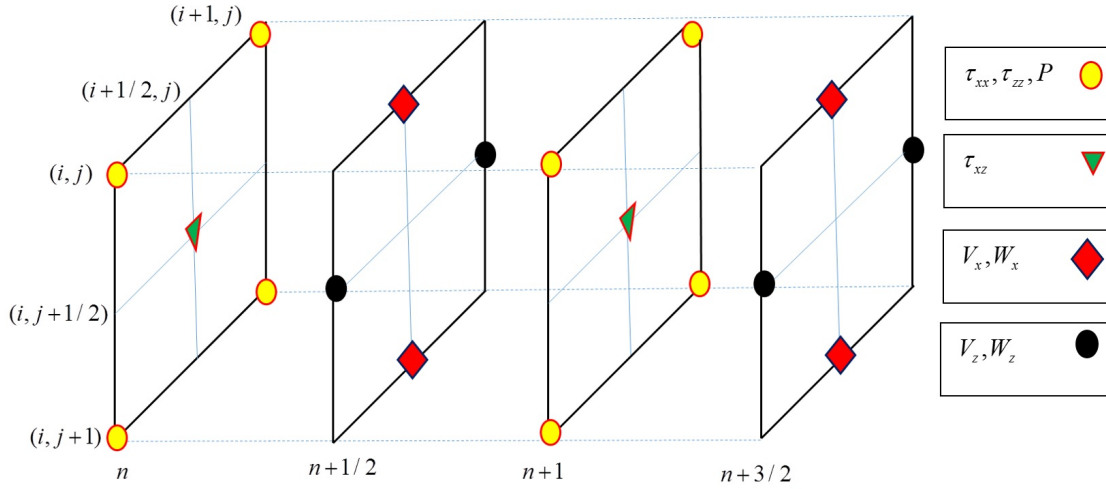


Figure 5.1: Schematic view of the staggered grid. The particle velocities of the solid and the fluid, V_x , V_z , W_x and W_z are calculated on a staggered time grid and the rest of the unknowns are defined on a regular time grid. The fluid pressure P and the normal stresses of the solid, τ_{xx} and τ_{zz} are calculated on a regular spatial grid, and the rest of the unknowns re evaluated on a staggered spatial grid.

5.3 The staggered grid technique

Equations 4.33 to 4.40 represent the velocity-stress formulation of the Biot's equations of motion in poroelastic media. The left hand side of the equations are the time derivatives of the unknown quantities. These quantities are: the particle velocities of the solid V_i and the fluid relative to the solid W_i , the solid stresses τ_{xx} , τ_{zz} , τ_{xz} , and the fluid pressure P . As mentioned previously, in the staggered grid technique some of the quantities are defined on a reference grid, and the rest of the are defined on a staggered grid that is shifted half a grid size. In the staggered grid method, the wave equations of motion are written as first order partial differential equations in terms of velocities and stresses (Levander, 1988). For the poroelastic media the quantities τ_{xx}, τ_{zz} and P are calculated on the reference grid, say, $x=ih$ (Figure 5.1). The rest of the quantities are then calculated on the staggered grid, say, $x=(i+1/2)h$, and $z=(j+1/2)h$.

The temporal grid is also consisted of both standard and staggered grids. The particle ve-

locities, V_x , V_z , W_x , and W_z are calculated on a staggered time grid in which for example $t = (n + 1/2)\Delta t$. The rest of unknowns are calculated on the standard time grid, in which $t = n\Delta t$ (Figure 5.1). The coordinates of the grid points are represented by their indices. For example, for the quantity V_z at the location of $x=ih$, and $z=(j + 1/2)h$ and the time of $t = (n + 1/2)\Delta t$ is represented as $V_z \Big|_{i,j+1/2}^{n+1/2}$. For all the quantities in the poroelastic medium in the 2D case we have:

$$\begin{aligned}\tau_{xx}(x, z, t) &= \tau_{xx} [ih, jh, n\Delta t] = \tau_{xx} \Big|_{i,j}^n, \\ \tau_{zz}(x, z, t) &= \tau_{zz} [ih, jh, n\Delta t] = \tau_{zz} \Big|_{i,j}^n, \\ P(x, z, t) &= P [ih, jh, n\Delta t] = P \Big|_{i,j}^n,\end{aligned}\tag{5.2}$$

$$\tau_{xz}(x, z, t) = \tau_{xz} \left[(i + 1/2)h, (j + 1/2)h, n\Delta t \right] = \tau_{xz} \Big|_{i+1/2, j+1/2}^n,\tag{5.3}$$

$$\begin{aligned}V_x(x, z, t) &= V_x \left[(i + 1/2)h, jh, (n + 1/2)\Delta t \right] = V_x \Big|_{i+1/2, j}^{n+1/2}, \\ W_x(x, z, t) &= W_x \left[(i + 1/2)h, jh, (n + 1/2)\Delta t \right] = W_x \Big|_{i+1/2, j}^{n+1/2},\end{aligned}\tag{5.4}$$

$$\begin{aligned}V_z(x, z, t) &= V_z \left[ih, (j + 1/2)h, (n + 1/2)\Delta t \right] = V_z \Big|_{i, j+1/2}^{n+1/2}, \\ W_z(x, z, t) &= W_z \left[ih, (j + 1/2)h, (n + 1/2)\Delta t \right] = W_z \Big|_{i, j+1/2}^{n+1/2},\end{aligned}\tag{5.5}$$

where all of these quantities are illustrated on a grid in Figure 5.1.

5.4 Discrete velocity-stress equations

In order to simulate wave propagation in the poroelastic media using the staggered-grid technique, the velocity-stress equations based on Biot's theory needed to be solved numerically. For

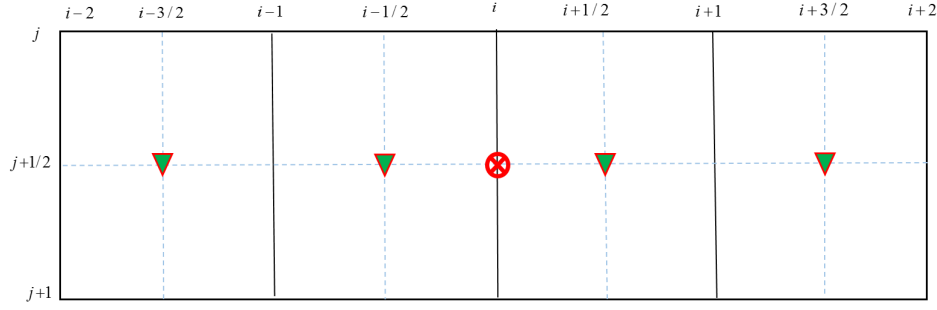


Figure 5.2: Calculation of $\Delta_x \tau_{xz} \Big|_{i,j+1/2}$ on the staggered grid (equation 5.9).

this purpose, Equations 4.33 to 4.40 were discretized using the staggered-grid finite-difference approximation. For example Equation 4.33, after discretization becomes:

$$V_z \Big|_{i,j+1/2}^{n+1/2} = V_z \Big|_{i,j+1/2}^{n-1/2} + \Delta t \left[A (D_x \tau_{xz} + D_z \tau_{zz}) - B (D_z P + b \bar{W}_z) \right] \Big|_{i,j+1/2}^n, \quad (5.6)$$

where superscripts and subscripts denote temporal and spatial indices, respectively. For the time derivative operator, a second order backward finite difference approximation is used, that for function ψ is

$$\frac{\partial \psi}{\partial t} = D_t \psi(t) \approx \frac{\psi(t) - \psi(t - \Delta t)}{\Delta t}, \quad (5.7)$$

therefore,

$$D_t V_z \Big|_{i,j+1/2}^{n+1/2} \approx \frac{V_z \Big|_{i,j+1/2}^{n+1/2} - V_z \Big|_{i,j+1/2}^{n-1/2}}{\Delta t}. \quad (5.8)$$

Furthermore, Δ_x and Δ_z are fourth-order $O(h^4)$ partial differential operators with respect to x and z , that are centred about the quantity being calculated. For example :

$$\Delta_x \tau_{xz} \Big|_{i,j+1/2} = \left[-c_1 \left(\tau_{xz} \Big|_{i+3/2,j+1/2} - \tau_{xz} \Big|_{i-3/2,j+1/2} \right) + c_2 \left(\tau_{xz} \Big|_{i+1/2,j+1/2} - \tau_{xz} \Big|_{i-1/2,j+1/2} \right) \right] / h, \quad (5.9)$$

where $c_2 = 9/8$ and $c_1 = 1/24$, are the inner and outer difference coefficients defined by Levan-
 der (1988). Figure 5.2 shows how $\Delta_x \tau_{xz} \Big|_{i,j+1/2}$ is being calculated using the values of τ_{xz} on

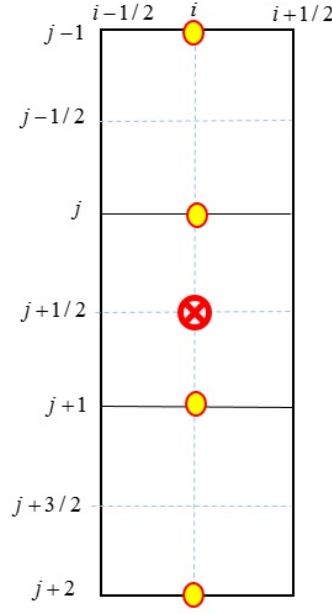


Figure 5.3: Calculation of $\Delta_z \tau_{zz} \Big|_{i,j+1/2}$ on the staggered grid (equation 5.10).

four adjacent grid points. The rest of the approximations could be derived similarly. Another example is shown in Figure 5.3 that presents the calculation of $\Delta_z \tau_{zz} \Big|_{i,j+1/2}$:

$$\Delta_z \tau_{zz} \Big|_{i,j+1/2} = \left[-c_1 \left(\tau_{zz} \Big|_{i,j+2} - \tau_{zz} \Big|_{i,j-1} \right) + c_2 \left(\tau_{zz} \Big|_{i,j+1} - \tau_{zz} \Big|_{i,j} \right) \right] / h. \quad (5.10)$$

5.4.1 Discrete equations in the internal region

Equation 5.6 is the discretized form of Equation 4.33. The discretization could be accomplished similarly for the rest of the equations. Thus, for Equations 4.33 to 4.40 we have:

$$V_z \Big|_{i,j+1/2}^{n+1/2} = V_z \Big|_{i,j+1/2}^{n-1/2} + \Delta t \left[A (D_x \tau_{xz} + D_z \tau_{zz}) - B (D_z P + b \overline{W}_z) \right] \Big|_{i,j+1/2}^n, \quad (5.11)$$

$$V_x \Big|_{i+1/2,j}^{n+1/2} = V_x \Big|_{i+1/2,j}^{n-1/2} + \Delta t \left[A (D_x \tau_{xx} + D_z \tau_{xz}) - B (D_x P + b \overline{W}_x) \right] \Big|_{i+1/2,j}^n, \quad (5.12)$$

$$W_z \Big|_{i,j+1/2}^{n+1/2} = W_z \Big|_{i,j+1/2}^{n-1/2} + \Delta t \left[B (D_x \tau_{xz} + D_z \tau_{zz}) - C (D_z P + b \overline{W}_z) \right] \Big|_{i,j+1/2}^n, \quad (5.13)$$

$$W_x \Big|_{i+1/2,j}^{n+1/2} = W_x \Big|_{i+1/2,j}^{n-1/2} + \Delta t \left[B(D_x \tau_{xx} + D_z \tau_{xz}) - C(D_x P + b \overline{W}_x) \right] \Big|_{i+1/2,j}^n, \quad (5.14)$$

$$P \Big|_{i,j}^{n+1} = P \Big|_{i,j}^n - M \Delta t \left[\alpha(D_x V_x + D_z V_z) + (D_x W_x + D_z W_z) \right] \Big|_{i,j}^{n+1/2}, \quad (5.15)$$

$$\tau_{xx} \Big|_{i,j}^{n+1} = \tau_{xx} \Big|_{i,j}^n + \Delta t \left[(2\mu + \lambda_c) D_x V_x + \lambda_c D_z V_z + \alpha M (D_x W_x + D_z W_z) \right] \Big|_{i,j}^{n+1/2}, \quad (5.16)$$

$$\tau_{zz} \Big|_{i,j}^{n+1} = \tau_{zz} \Big|_{i,j}^n + \Delta t \left[(2\mu + \lambda_c) D_z V_z + \lambda_c D_x V_x + \alpha M (D_x W_x + D_z W_z) \right] \Big|_{i,j}^{n+1/2}, \quad (5.17)$$

$$\tau_{xz} \Big|_{i+1/2,j+1/2}^{n+1} = \tau_{xz} \Big|_{i+1/2,j+1/2}^n + \Delta t \left[\mu (D_x V_z + D_z V_x) \right] \Big|_{i+1/2,j+1/2}^{n+1/2}. \quad (5.18)$$

These equations are used in the internal region of the computational grid. As explained earlier, the grid is divided into two region in order to have an absorbing region close to the boundaries of the grid. The absorbing boundary region is referred to as the "PML region" since the PML method is used in this region.

5.4.2 Discrete equations in the PML region

At the PML region Equation 5.18 is split into the following equations:

$$V_z^x \Big|_{i,j+1/2}^{n+1/2} = (1 - a_x \Delta t) V_z^x \Big|_{i,j+1/2}^{n-1/2} + \Delta t \left[A \Delta_x \tau_{xz} - B b \left(\overline{W}_z^x + a_x \int_0^t \overline{W}_z^x dt \right) \right] \Big|_{i,j+1/2}^n, \quad (5.19)$$

$$V_z^z \Big|_{i,j+1/2}^{n+1/2} = (1 - a_z \Delta t) V_z^z \Big|_{i,j+1/2}^{n-1/2} + \Delta t \left[A \Delta_z \tau_{zz} - B \Delta_z S - B b \left(\overline{W}_z^z + a_z \int_0^t \overline{W}_z^z dt \right) \right] \Big|_{i,j+1/2}^n, \quad (5.20)$$

The finite-difference approximation for the rest of equations could be obtained similarly and used to develop the modeling program. All the Biot's equations are discretized similarly to develop the poroelastic finite-difference program. The discrete equations after applying the PML are:

$$V_x^z \Big|_{i+1/2,j}^{n+1/2} = (1 - a_z \Delta t) V_x^z \Big|_{i+1/2,j}^{n-1/2} + \Delta t \left[AD_z \tau_{xz} - Bb \left(\overline{W_x^z} + a_z \int_0^t W_x^z dt \right) \right] \Big|_{i+1/2,j}^n, \quad (5.21)$$

$$V_x^x \Big|_{i+1/2,j}^{n+1/2} = (1 - a_x \Delta t) V_x^x \Big|_{i+1/2,j}^{n-1/2} + \Delta t \left[AD_x \tau_{xx} - BD_x P - Bb \left(\overline{W_x^x} + a_x \int_0^t W_x^x dt \right) \right] \Big|_{i+1/2,j}^n, \quad (5.22)$$

$$W_z^z \Big|_{i,j+1/2}^{n+1/2} = (1 - a_z \Delta t) W_z^z \Big|_{i,j+1/2}^{n-1/2} + \Delta t \left[BD_z \tau_{zz} + CD_z P + Cb \left(\overline{W_z^z} + a_z \int_0^t W_z^z dt \right) \right] \Big|_{i,j+1/2}^n, \quad (5.23)$$

$$W_z^x \Big|_{i,j+1/2}^{n+1/2} = (1 - a_x \Delta t) W_z^x \Big|_{i,j+1/2}^{n-1/2} + \Delta t \left[BD_x \tau_{xz} + Cb \left(\overline{W_z^x} + a_x \int_0^t W_z^x dt \right) \right] \Big|_{i,j+1/2}^n, \quad (5.24)$$

$$W_x^z \Big|_{i+1/2,j}^{n+1/2} = (1 - a_z \Delta t) W_x^z \Big|_{i+1/2,j}^{n-1/2} + \Delta t \left[BD_z \tau_{xz} + Cb \left(\overline{W_x^z} + a_z \int_0^t W_x^z dt \right) \right] \Big|_{i+1/2,j}^n, \quad (5.25)$$

$$W_x^x \Big|_{i+1/2,j}^{n+1/2} = (1 - a_x \Delta t) W_x^x \Big|_{i+1/2,j}^{n-1/2} + \Delta t \left[BD_x \tau_{xx} + CD_x P + Cb \left(\overline{W_x^x} + a_x \int_0^t W_x^x dt \right) \right] \Big|_{i+1/2,j}^n, \quad (5.26)$$

$$P^z \Big|_{i,j}^{n+1} = (1 - a_z \Delta t) P \Big|_{i,j}^n - M \Delta t \left[\alpha D_z V_z + D_z W_z \right] \Big|_{i,j}^{n+1/2}, \quad (5.27)$$

$$P^x \Big|_{i,j}^{n+1} = (1 - a_x \Delta t) P \Big|_{i,j}^n - M \Delta t \left[\alpha D_x V_x + D_x W_x \right] \Big|_{i,j}^{n+1/2}, \quad (5.28)$$

$$\tau_{xx}^z \Big|_{i,j}^{n+1} = (1 - a_z \Delta t) \tau_{xx}^z \Big|_{i,j}^n + \Delta t \left[\lambda_c D_z V_z + \alpha M D_z W_z \right] \Big|_{i,j}^{n+1/2}, \quad (5.29)$$

$$\tau_{xx}^x \Big|_{i,j}^{n+1} = (1 - a_x \Delta t) \tau_{xx}^x \Big|_{i,j}^n + \Delta t \left[(2\mu + \lambda_c) D_x V_x + \alpha M D_x W_x \right] \Big|_{i,j}^{n+1/2}, \quad (5.30)$$

$$\tau_{zz}^z \Big|_{i,j}^{n+1} = (1 - a_z \Delta t) \tau_{zz}^z \Big|_{i,j}^n + \Delta t \left[(2\mu + \lambda_c) D_z V_z + \alpha M D_z W_z \right] \Big|_{i,j}^{n+1/2}, \quad (5.31)$$

$$\tau_{zz}^x \Big|_{i,j}^{n+1} = (1 - a_x \Delta t) \tau_{zz}^x \Big|_{i,j}^n + \Delta t \left[\lambda_c D_x V_x + \alpha M D_x W_x \right] \Big|_{i,j}^{n+1/2}, \quad (5.32)$$

$$\tau_{xz}^z \Big|_{i+1/2,j+1/2}^{n+1} = (1 - a_z \Delta t) \tau_{xz}^z \Big|_{i+1/2,j+1/2}^n + \Delta t \mu D_z V_x \Big|_{i+1/2,j+1/2}^{n+1/2}, \quad (5.33)$$

$$\tau_{xz}^x \Big|_{i+1/2,j+1/2}^{n+1} = (1 - a_x \Delta t) \tau_{xz}^x \Big|_{i+1/2,j+1/2}^n + \Delta t \mu D_x V_z \Big|_{i+1/2,j+1/2}^{n+1/2}. \quad (5.34)$$

5.5 Source implementation

One of the key steps in finite difference modeling is the implementation of the source. In this thesis, we assume that an explosive source generates only a compressional (P) wave. This type of source could be used both in land and marine seismic surveys. In this thesis an explosive source was used in the numerical modeling. To generate a source pulse in the model, a wavelet is injected into the stress tensors through time. In the case of the explosive source, the wavelet needs to be added to the solid normal stresses τ_{xx} and τ_{zz} . Since the proelastic medium is composed of a fluid and a solid phase, the source needs to be also added to the fluid pressure P. This approach has been used previously by (Zhu and McMechan, 1991). In terms of the energy, the source energy is partitioned between the solid and the fluid phases. This is done by scaling the wavelet by the factor of $(1 - \phi)$ for the solid phase, and by the factor of ϕ for the fluid phase with ϕ being the porosity. Therefore, two source wavelets are defined:

$$w_{solid} = (1 - \phi)w, \quad (5.35)$$

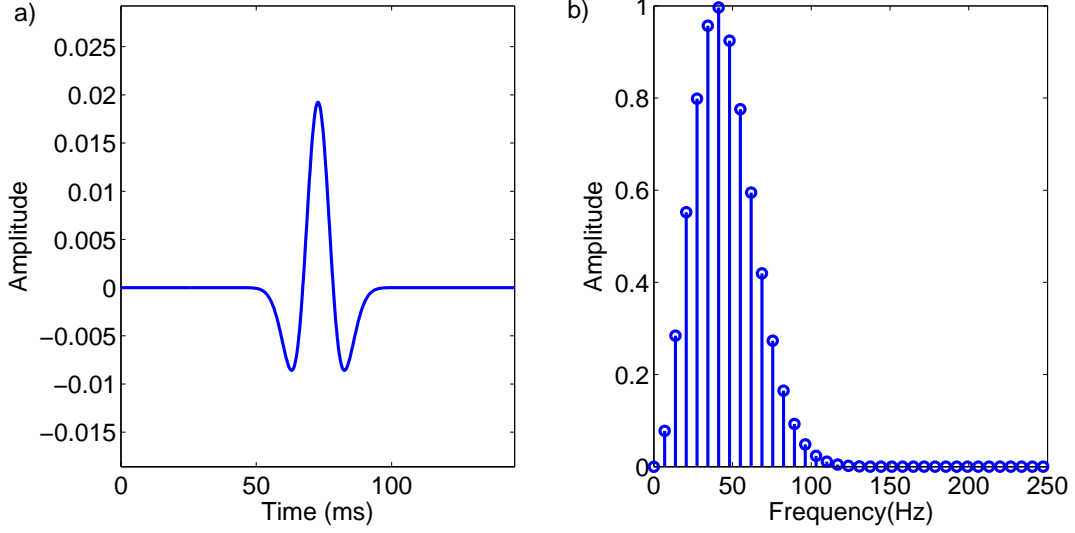


Figure 5.4: The Ricker wavelet used as an explosive source in the modelings, represented in time (a) and frequency (b) domains. The dominant frequency of this wavelet is 40 Hz.

and

$$w_{fluid} = \phi w, \quad (5.36)$$

where w is the source wavelet.

The selected wavelet for the source in this work was the zero-phase Ricker wavelet. The Ricker wavelet is the second derivative of a Gaussian function, and is defined as:

$$f(t) = (1 - 2\pi^2 f_{dom}^2 t^2) e^{-\pi^2 f_{dom}^2 t^2}, \quad (5.37)$$

where f_{dom} is the dominant frequency of the wavelet, and t is the length of the wavelet in time. Figure 5.4 shows the wavelet used in this thesis, in both time and frequency domains. The dominant frequency of this wavelet is 40 Hz which is a typical dominant frequency in seismic data. This frequency has the maximum amplitude in the spectrum, as shown in Figure 5.4.b.

5.6 Generated snapshots

In this section we present some numerical examples to verify our finite-difference program. The numerical examples are based on the Quest project, and the details about the well log data were discussed in Chapter 3. The target formation for injection in the Quest project is the Basal Cambrian Sandstone (BCS). The in-situ properties of the BCS were extracted from the well data and listed in Table 3.3 as BCS_{Base} . In addition, using Gassmann's method, 40% of the in-situ brine was replaced by CO_2 and the properties of the BCS after substitution were calculated. These values that are listed in Table 3.3 as BCS_{Mon} , represent the BCS after injecting CO_2 . For numerical examinations of the developed finite-difference algorithm, two example models were defined and used as inputs in the program.

5.6.1 Uniform model with zero fluid viscosity: non-diffusive slow mode

The first example model is a uniform model with the properties of BCS_{Base} (Table 3.3). The dimensions of this model are 2 km by 2 km . The Ricker wavelet in Figure 5.4 with the dominant frequency of 40 Hz was used as an explosive source for modeling. The source is located at the center of the grid, that is $(x,z)=(1000,1000)$. The time step and grid size were chosen to be respectively 0.2 ms and 2 meters . Figure 5.5 shows this model along with the location of the source.

The unknowns are the solid and fluid particle velocities W and V , the solid stresses τ_{ij} , and the fluid pressure P that are calculated by the program. Biot's theory predicts a slow wave (P_s), generated due to the relative movement of the fluid with respect to the solid. The slow P-wave is not noticeable in seismic frequencies unless the factor b is close to zero. The reason is that in the seismic frequencies, the slow mode attenuates quickly due to viscosity of the fluid (Carcione et al., 2010; Carcione and Quiroga-Goode, 1995). However, if the fluid's viscosity (and therefore the factor b) is zero, the slow P-wave will be a traveling wave even in seismic frequencies. In this section we present the wave behavior in a uniform model in the absence

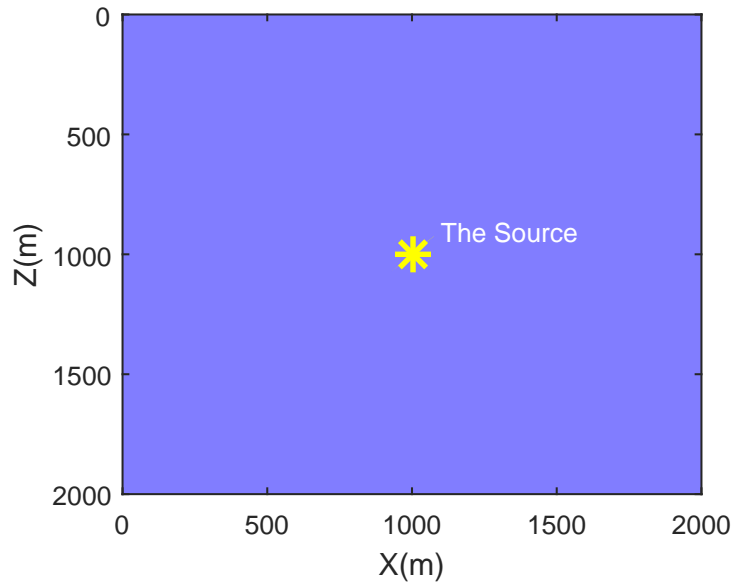


Figure 5.5: The uniform model used in examples, and the location of the source. This model is based on the in-situ properties of the BCS that are listed in Table 3.3 as BCS_{Base} .

of the fluid viscosity, when $b = 0$. We refer to this type of slow P-wave as "non-diffusive". In comparison, in the section 5.6.2 we show the results from the same model, with the same physical properties but with a nonzero viscosity, or when $b \neq 0$. This type of slow P-wave is referred to as "diffusive".

Figure 5.6 shows the calculated particle velocities of the solid and the fluid at the time of 0.14 s for the case of $b = 0$. The slow P-wave is observed as a traveling mode in the snapshots, and has a relatively small amplitude compared to the "fast P-wave". The slow and the fast P-waves are denoted in the figure, respectively by P_s and P_f . It can be noticed that the slow P-wave in the fluid snapshot has a larger amplitude relative to the fast P-wave in the same snapshot. This could be due to the nature of the slow P-wave which is generated by the fluid motion.

5.6.2 Uniform model with nonzero fluid viscosity: diffusive slow mode

The uniform model is used as our next example to see the wave propagation when the factor b is nonzero. Figure 5.7 shows the snapshots from this model with two different nonzero mobilities,

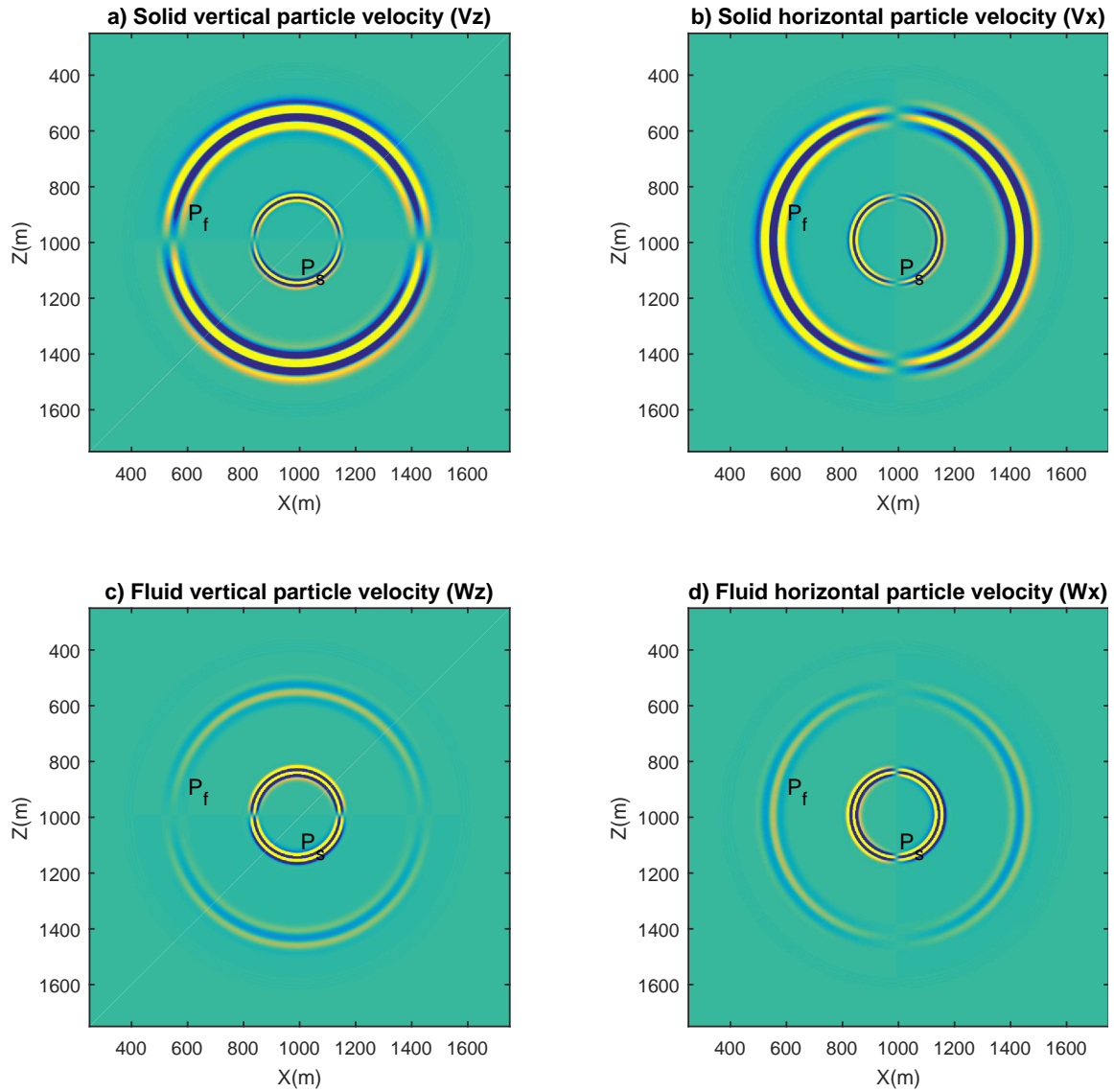


Figure 5.6: Sample snapshots of the vertical particle velocities of the solid (top row) and the fluid with respect to solid (bottom row) in both x and z directions. The model used in this example is the uniform model with $b = 0$. The snapshots were taken at the time of 0.14 s. The fast and the slow P-waves are respectively denoted by P_f and P_s .

along with the snapshots for the same model with zero b factor. The first column in the left is the same as our last example which was shown in Figure 5.6. One of the b factor values was estimated based on the estimated pore fluid viscosity in our example, and the permeability of the target formation, BCS. The BCS is known to have a permeability of 1 mD to $>1\text{ D}$, thus the permeability of the porous rock was assumed to be 1 D . The viscosity of the fluid was calculated based on the viscosity of the CO_2 and brine mixture in the temperature and pressure of the BCS. In this case, the average viscosity for the mixture of brine and CO_2 was approximated to be 10^{-5} kg/ms . Therefore, the estimated value of b for the BCS was 10^7 Pa sm^{-2} . The other value of b used in this example was randomly chosen so that it falls between the other two values of $b = 0$ and $b = 10^7\text{ Pa sm}^{-2}$. The selected b value was 10^5 Pa sm^{-2} which is smaller than the 10^7 Pa sm^{-2} and larger than zero. It is obvious that by increasing the factor b , the amplitude of the slow P-wave decreases and the wave becomes diffusive. It is also clear in the fluid snapshots that the fluid movement decreases by increasing b .

In Figure 5.8, traces from the two above examples have been plotted in order to examine the effect of b factor on the generated traces. In the case that $b = 0$, a non-diffusive slow P-wave is generated. The slow P-wave is also generated in the case of nonzero b factor ($b = 10^5\text{ Pa sm}^{-2}$), but in a diffusive form. By comparing the two traces through time we can see that the diffusive slow P-wave attenuates very quickly, while the non-diffusive one remains unchanged. This is consistent with the Biot's theory that suggests that the slow P-wave at typical seismic frequencies is diffusive.

Another fact that could be observed in Figure 5.8 is the difference in amplitudes of the fast P-waves. In poroelastic media, the fast P-wave amplitude reduces due to the wave partitioning and the presence of the slow P-wave. It is obvious that the difference between the two fast P-wave amplitudes in this figure is negligible. It can be concluded that the energy loss in poroelastic media is more due to the energy partitioning than to only the magnitude of the factor b .

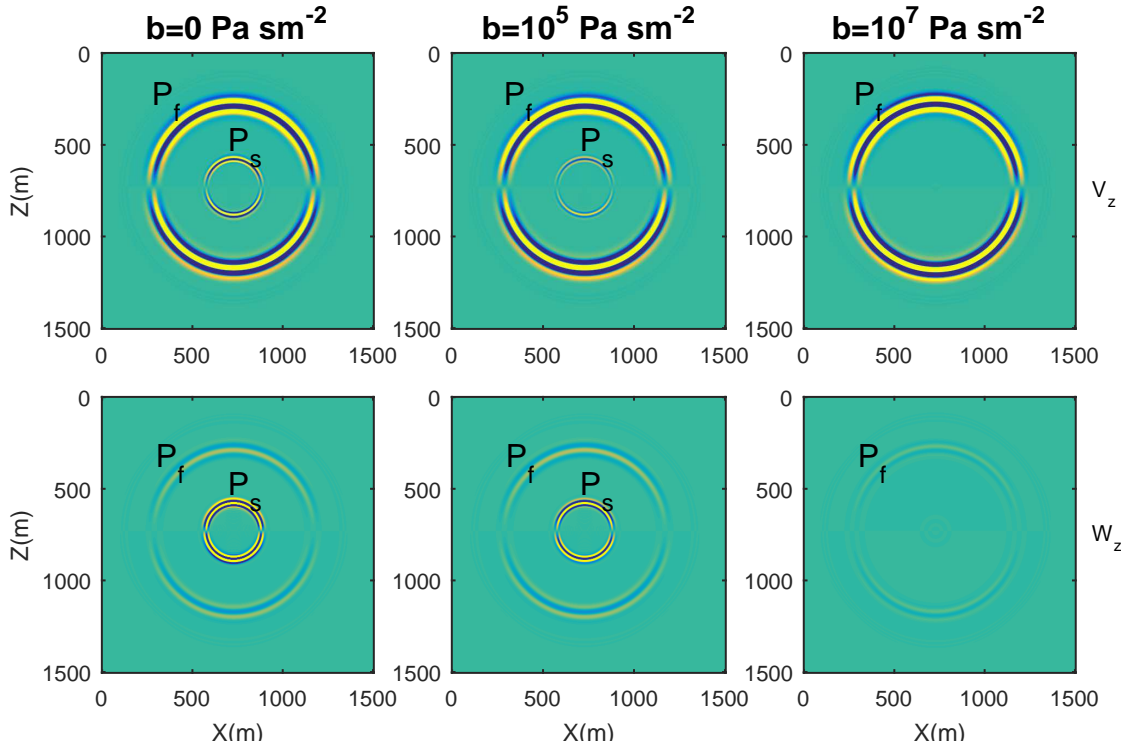


Figure 5.7: Sample snapshots of the vertical particle velocities of the solid (top row) and the fluid respect to solid (bottom row) for three different values of factor b . By increasing the value of b , the slow P-wave starts to become diffusive and being absorbed in the medium. The fast and the slow P-waves are respectively denoted P_f and P_s . The snapshots were taken at the time of 0.14 s.

5.6.3 Two layer model with zero fluid viscosity

The second example model is composed of two homogeneous layers (Figure 5.9). The lower layer is the BCS with in-situ properties, where the pore fluid is 100 % brine. This layer represents the baseline scenario for the Basal Cambrian Sands. As mentioned previously, the properties of the BCS for the baseline scenario are listed in Table 3.3 as BCS_{Base} . The upper layer, shows the BCS after replacing 40 % of the brine with CO_2 which represents the monitor scenario for this formation. The properties of the monitor scenario for the BCS are listed in Table 3.3 as BCS_{Mon} . These two layers are in fact two sandstones with the same solid properties but with different pore fluid. This model represents a storage rock in which the injected CO_2 has migrated towards the top of the rock due to the buoyancy force. The change in the fluid content

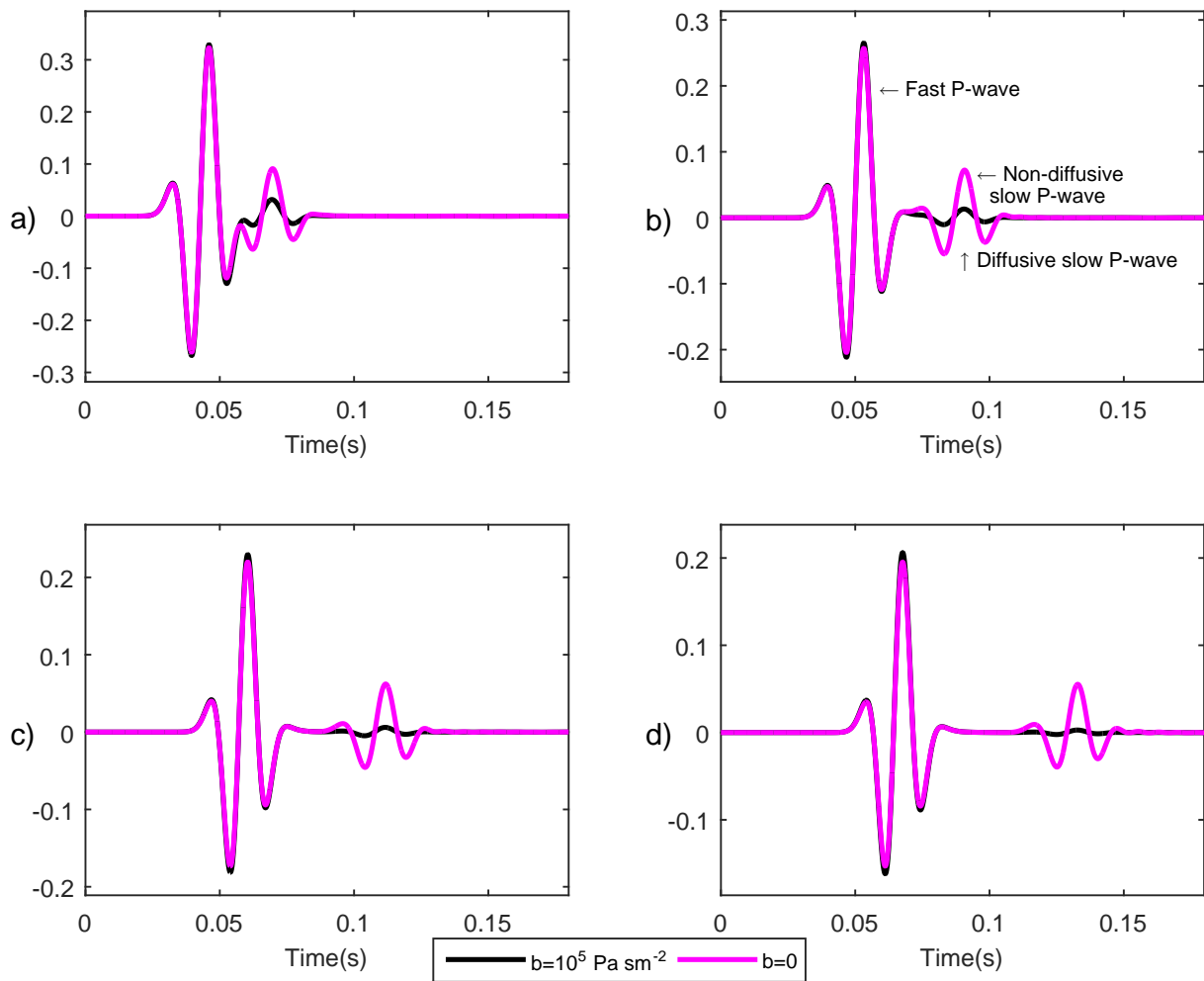


Figure 5.8: Traces from the vertical particle velocities of the solid in poroelastic media, for two values of $b = 0$ and $b = 10^5 \text{ Pa sm}^{-2}$. The slow P-wave in the case of $b \neq 0$ dissipates quickly while in the case of $b = 0$ it does not dissipate in the medium.

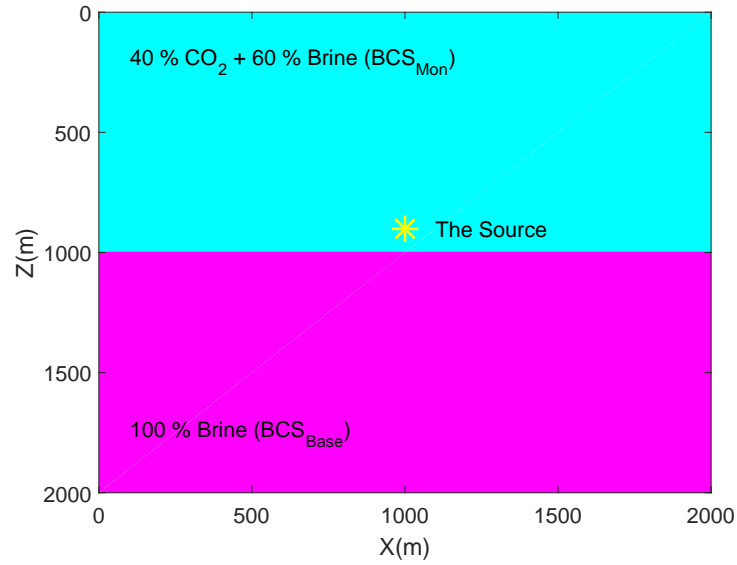


Figure 5.9: The two-layer model used in the examples. The top layer represents the BCS with in-situ properties, also listed in Table 3.3 as BCS_{Base} . The lower layer represents the BCS after injecting CO_2 , also listed in Table 3.3 as BCS_{Mon} .

of the rock leads to a change in the seismic response of the model. The purpose of showing this example is to see the mode conversions at a boundary made by differences in pore fluid, and also to verify the developed algorithm. In this example, the value of the b factor for both layers was assumed to be zero in order to observe the slow P-wave and consequently the mode conversions at the boundary. Figure 5.10.a shows a snapshot of the vertical particle velocity of the solid calculated for this model at the time of 0.2 s. The source was located at $(x,z)=(1000\text{ m},900\text{ m})$ and the grid size was the same as the previous example. As expected the slow P-wave (P_s) is generated due to the fluid movement relative to the solid frame. In addition, there are some mode conversions at the boundary including a fast P-wave converted from the slow P-wave (P_sP_f), and a slow P-wave converted from the fast P-wave (P_fP_s). The snapshots have been magnified by the factor of 100 in order to better display the waves with lower amplitudes.

In order to compare the poroelastic algorithm with an elastic one, in which the medium is assumed to be homogeneous solid with no fluid, the same model was used in the program but with an elastic assumption. This was accomplished by setting the fluid properties and the poros-

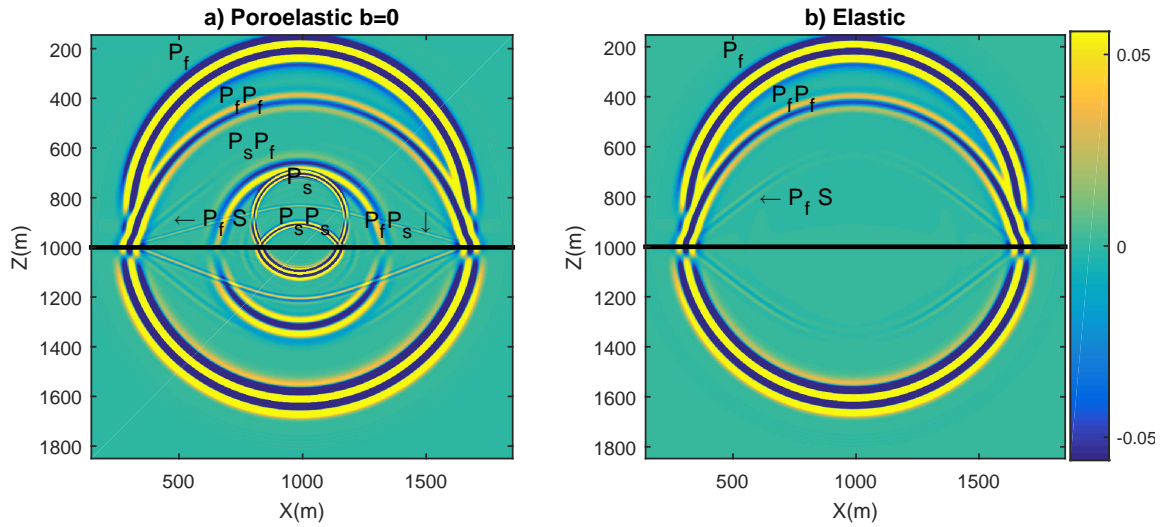


Figure 5.10: Snapshots of the vertical particle velocity of the solid for the two-layer model, calculated for a) poroelastic case, and b) elastic case. The horizontal line at the depth of 1000m represents the boundary. To see the reflections more clearly, the amplitudes are magnified by factor of 100. The direct and reflected waves are denoted in the figure as follows: the direct fast P-wave (P_f), the reflected fast P-wave ($P_f P_f$), the slow P-wave (P_s), the S-wave converted from the fast P-wave ($P_f S$), the slow P-wave converted from the fast P-wave ($P_f P_s$), and the fast P-wave converted from the slow P-wave ($P_s P_f$).

ity equal to zero and using the elastic properties of the saturated rock as model parameters. This way the presence of fluid as a separate phase is ignored and the rock behaves as an elastic solid in the modeling process. Figure 5.10.b shows the generated elastic snapshot. This figure illustrates how the wave propagates differently in an elastic medium versus a poroelastic medium. Although the slow P-wave cannot be detected in real seismic data, the energy loss caused by the fluid flow decreases the wave energy and therefore the amplitude of the reflections.

5.7 PML boundary condition

I now consider the uniform model used in Section 5.6.1 to examine the boundary conditions. Figure 5.11 shows the snapshot from the uniform model at a time of 0.32 s with different thicknesses of the PML boundary used in the algorithm. These thicknesses are $n_{PML}=0,10,20,30$, where n_{PML} is the number of the grid points used as the PML boundary. In the case that there

is no PML boundary, where $n_{PML}=0$, strong reflections are generated at the model borders as shown in Figure 5.11.a. These reflection start to fade by increasing the thickness of the PML region (Figure 5.11.b to d). For this model, we notice that with 20 nodes for the PML layer, the artifacts are effectively removed. This result is satisfactory and therefore there is no need to increase the PML thickness any further.

Figure 5.12 shows the computational grid used for this model with $n_{PML}=30$. The color-map represents the summation of attenuation factors a_z and a_x which are calculated from Equation 4.61. The values of the factors are zero in the internal region, and nonzero in the PML region. The value of a_x+a_z is larger at the corners because in that areas the wave hits the borders from both x and z directions. Therefore, at the corners both a_x and a_z are nonzero. Figure 5.13 (top row) shows the generated shot gathers for the uniform model in the case of $b \neq 0$, without PML boundary and with a PML boundary of 20 nodes. Selected traces from both gathers at the location of $x= 600 \text{ m}$ are also shown in the bottom row of the figure. It is observed from the traces, that the artifacts are absorbed efficiently by the PML boundary method. Similarly, generated gathers and selected traces for the uniform model in the case of zero b factor are shown in Figure 5.14. Likewise, in this case, the artifacts have been absorbed very well.

As I showed here, the PML boundary method is an efficient and effective way to attenuate the outgoing waves at the computational grid boundaries. It is worth mentioning that having a sharp transition from the internal grid to the PML grid could also generate some reflections. This problem could be partially resolved by smoothing the damping factors a_x and a_z . In all of our examples these factors have been smoothed accordingly.

5.8 Stability

In the finite-difference technique, the wavefield quantities at each time step are calculated from the ones calculated at the earlier times. Since the wave equations are approximated and truncated in this technique, the error caused by truncations could accumulate through time. This

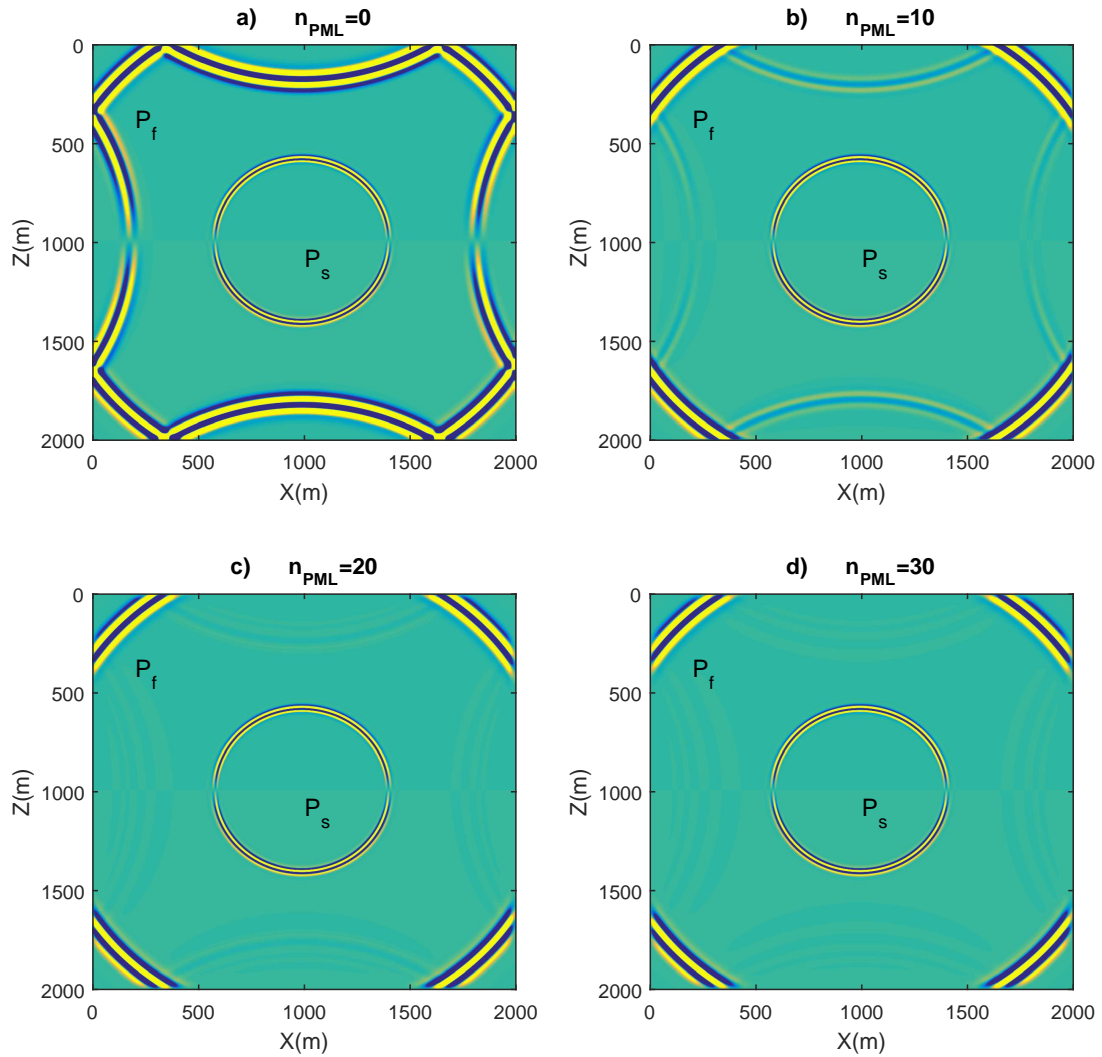


Figure 5.11: Snapshots of the vertical particle velocity of the solid with different values of $n_{PML}=0, 10, 20, 30$. By increasing the thickness of the PML region, the outgoing waves are absorbed more effectively. To see the artifacts more clearly, the amplitudes are magnified by the factor of 10.

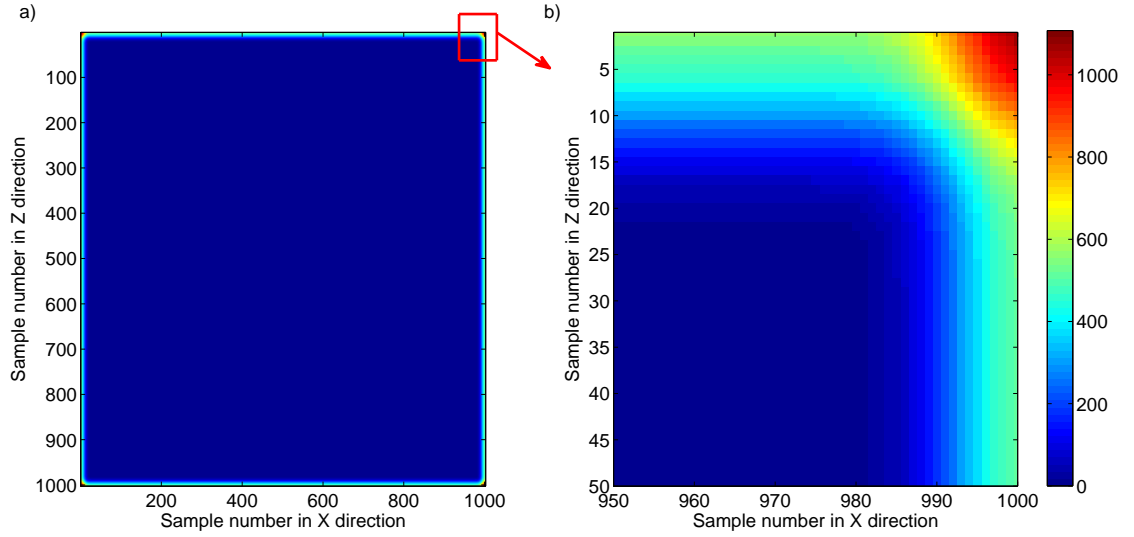


Figure 5.12: a) An example of a PML grid defined for the uniform model with dimensions of $1000 \text{ m} \times 1000 \text{ m}$. The image shows the summation $a_x + a_z$ where a_x and a_z are the attenuation factors in x and z directions. b) A closer view of the corner of the grid. In this example 20 grid points are used in the PML layer. The attenuation factors are zero at the internal grid and increase when moving towards the grid borders.

problem could be overcome by selecting a smaller time step and a larger grid size for calculations. However, selecting a larger grid size results in dispersion of the wave. Therefore, finding a stability condition for the finite difference algorithm helps to optimize the selected intervals to avoid either instability or dispersion of the numerical solution. Masson et al. (2006) derived the stability condition for staggered-grid finite-difference scheme solving the Biot's equations. They showed that, for a poroelastic medium in the case of $b = 0$, the surface separating the stable and unstable region is defined by:

$$\Delta t = h \sqrt{\frac{\pi_2 - \sqrt{\pi_2^2 - 4\pi_3\pi_1}}{2(c_1 + c_2)^2\pi_3}}, \quad (5.38)$$

where Δt and h are respectively the time step and the grid size. Furthermore, $c_1 = 1/24$ and $c_2 = 9/8$ are the difference coefficients in the fourth order spatial partial differential operator,

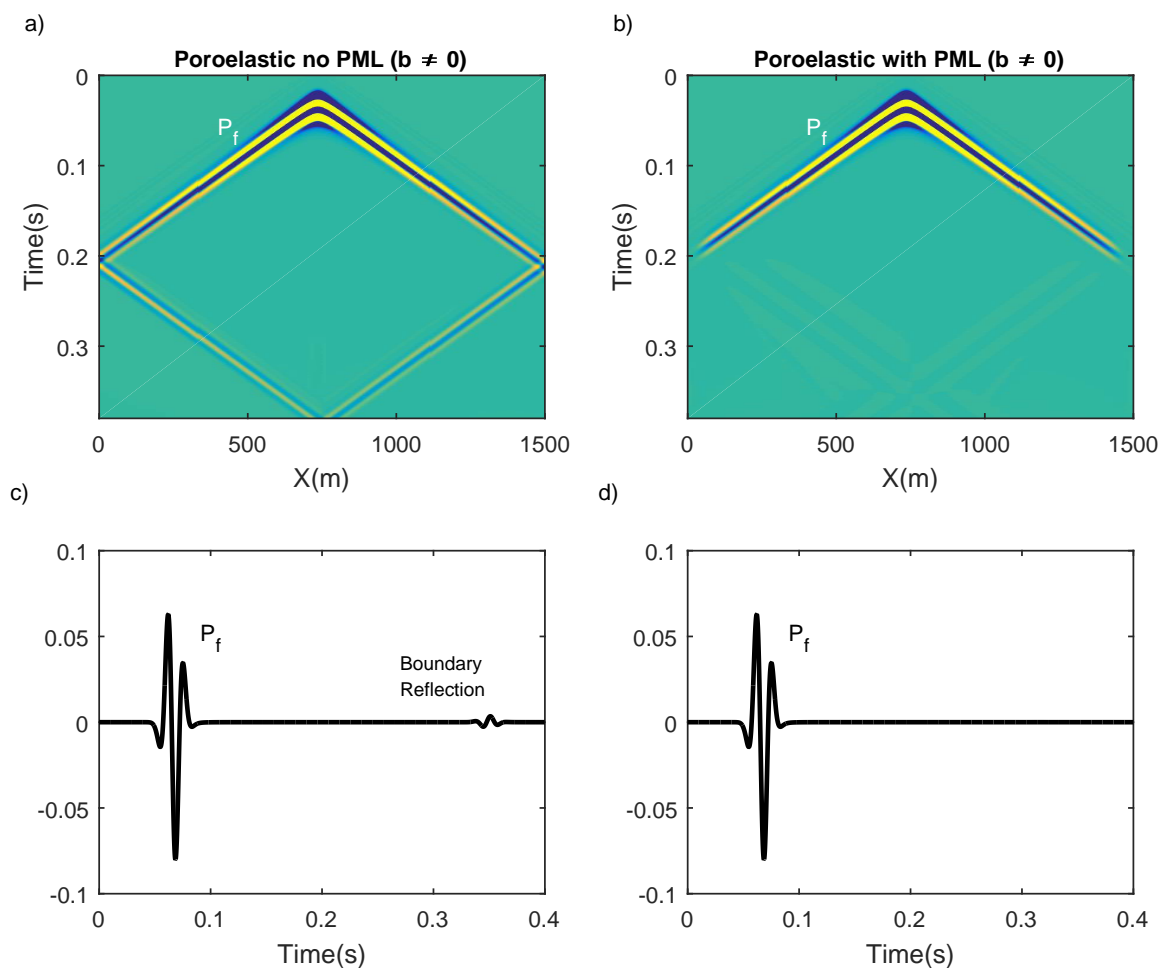


Figure 5.13: Sample shot gathers generated for the uniform model with $b \neq 0$, using the poroelastic algorithm, along with the selected traces from these gathers. a) No PML is used, therefore strong reflections from the boundaries are generated. b) A PML boundary with 20 nodes is used and the artifacts are efficiently removed. The amplitudes are magnified by the factor of ten to better illustrate the artifacts. c) and d) are selected trace at location of $x=600 \text{ m}$ respectively from shot gathers in a and b.

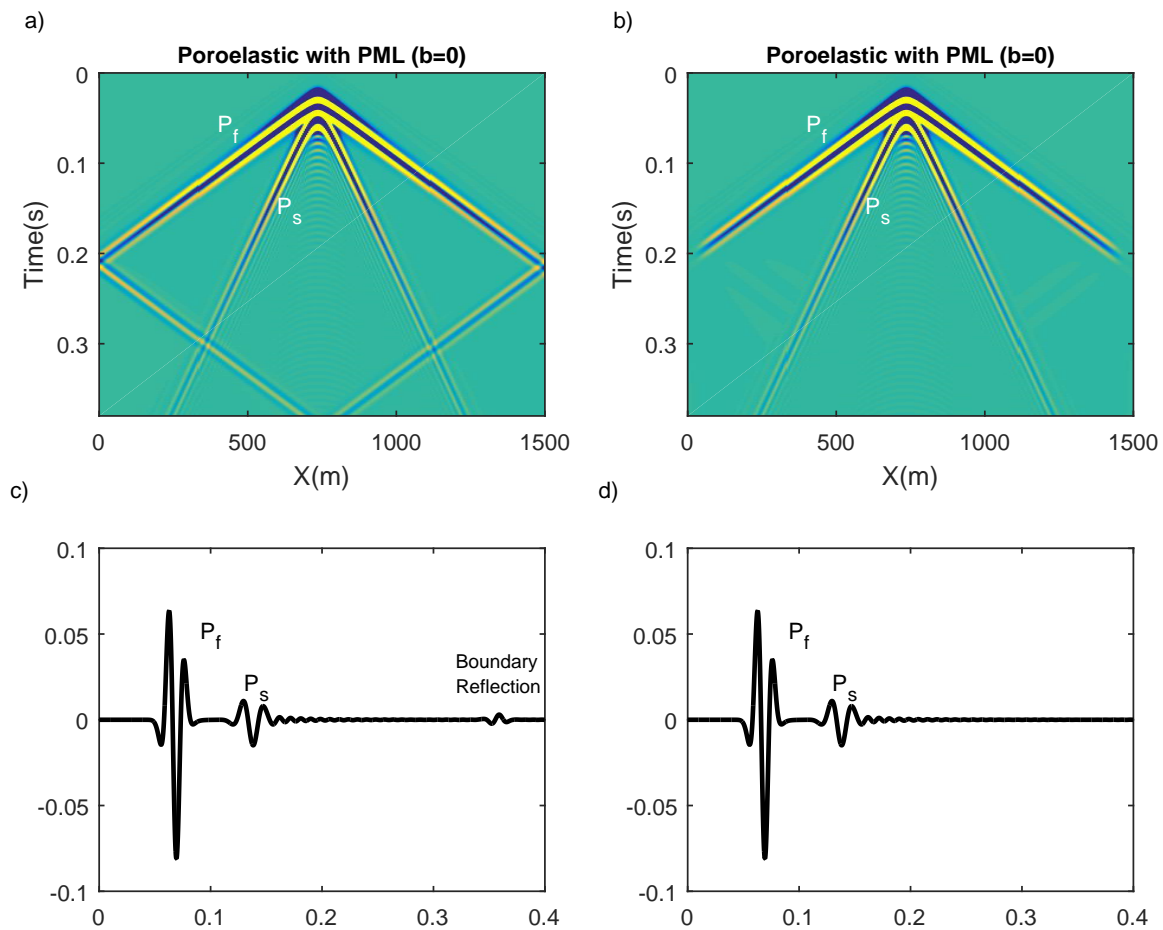


Figure 5.14: Sample shot gathers generated for the uniform model with $b = 0$, using the poroelastic algorithm, along with the selected traces from these gathers. a) No PML is used, therefore strong reflections from the boundaries are generated. b) A PML boundary with 20 nodes is used and the artifacts are efficiently removed. The amplitudes are magnified by the factor of ten to better illustrate the artifacts. c) and d) are selected trace at location of $x=600$ m respectively from shot gathers in a and b.

and

$$\pi_1 = m\rho - \rho_f^2, \quad (5.39)$$

$$\pi_2 = m(\lambda + 2\mu) + \rho M + 2\alpha M \rho_f, \quad (5.40)$$

$$\pi_3 = M(\lambda + 2\mu - \alpha^2 M), \quad (5.41)$$

where all the parameters are previously introduced (Table 4.1). The surface separating the stable and unstable areas is plotted for our uniform model in Figure 5.15. This figure shows this surface as a function of Δt , h and m/ρ_f . It is noticed that the relationship between h and Δt is always linear regardless of the magnitude of m/ρ (Figure 5.15.c).

It is worth mentioning that, for $\pi_1=0$, Δt is equal to zero, and thus the scheme becomes unconditionally unstable. According to Equation 5.39 this condition happens when $m/\rho_f = \rho_f/\rho$. Therefore, the solution is always unstable for $m/\rho_f < \rho_f/\rho$ as also seen in Figure 5.15.

To test the Masson et al. (2006) stability criterion, we tried different pairs of $(\Delta t, h)$ for our program. These pairs are shown as data points in Figure 5.16. The pairs that result in instability are represented by red crosses, and the ones with stable results are represented with blue stars. Furthermore, Masson et al. (2006) stability criteria calculated for our model is plotted on top of these points. The results show that, the stability of our algorithm matches the Masson et al. (2006) criteria quite well. However, the algorithm in the case with diffusion would be more unstable due to the presence of the diffusive slow P-wave. For example, Figure 5.17 shows snapshots generated using different pairs of $(\Delta t, h)$ for both diffusive and non-diffusive cases. It is noticed that, the pair $(\Delta t, h)=(0.3 \text{ ms}, 4 \text{ m})$ gives unstable results in the diffusive case while the results of the same pair in the non-diffusive case is stable.

Another common issue in finite-difference modeling is numerical dispersion, which is basically propagating wave packets with different velocities. The dispersion is normally controlled by ensuring that the grid size is not too large relative to the wavelength. A good criteria to use is the one used by Levander (1988) for the fourth order finite-difference approximation. He suggested that, at least 5 grid points should be sampled in one wavelength in order to avoid

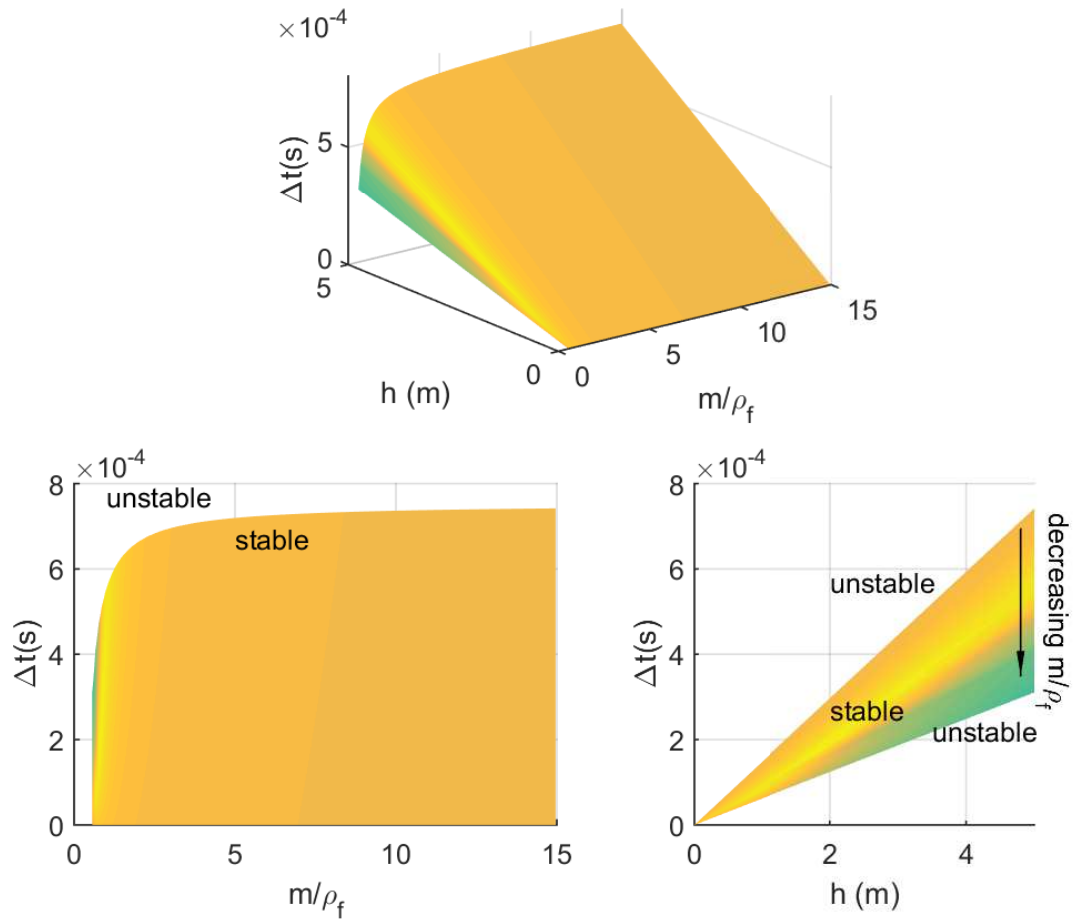


Figure 5.15: a) The surface separating the stable and unstable areas calculated based on Masson et al. (2006) criteria for our uniform model. This surface is plotted as a function of the time interval Δt , the grid size h and the factor m/ρ_f . b) The Δt – m/ρ_f plane view of the surface, which indicates for $m/\rho_f < \rho_f/\rho$ the solution is always unstable. c) The Δt – h view, where the relationship between Δt and h is always linear.

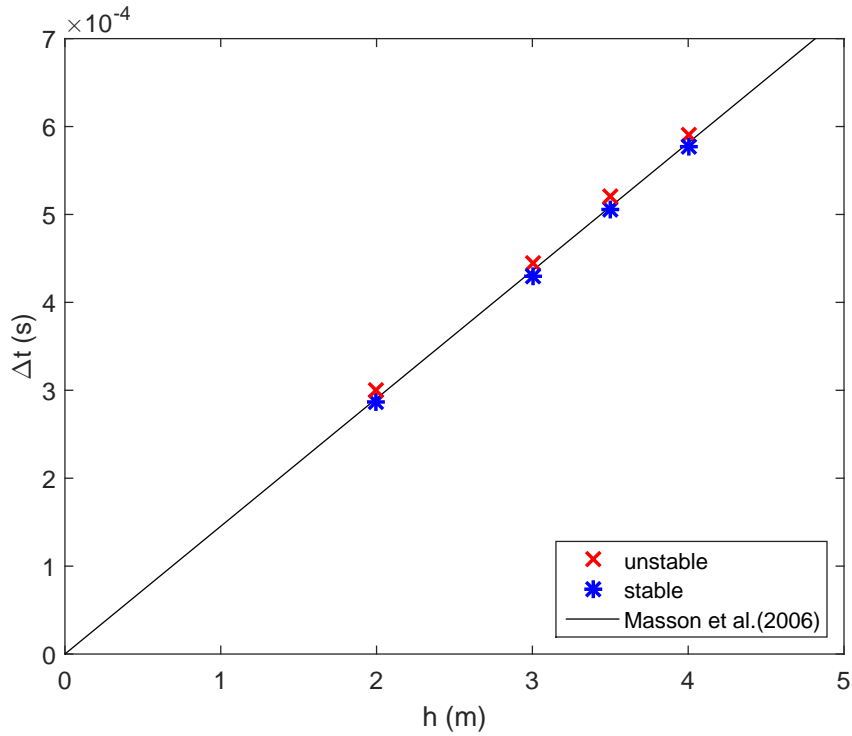


Figure 5.16: Several pairs of $(\Delta t, h)$ were used to test the stability of our algorithm for the uniform model (for $b = 0$). The stable pairs are shown with blue stars and the unstable ones are shown with red crosses. The straight line is the Masson et al. (2006) stability criteria calculated for this model. The stability of our algorithm matches the Masson et al. (2006) criteria very well.

dispersion. Therefore,

$$h < v_{min}/5f_{max}, \quad (5.42)$$

where v_{min} is the velocity of the slowest wave traveling in the medium, and f_{max} is the maximum source frequency. In the poroelastic media, for the non-diffusive case, the slowest wave is the slow P-wave, therefore there will be more limitations on defining the grid spacing. This is shown in figure 5.17.d to f in which by increasing h , the slow P-wave becomes more dispersive.

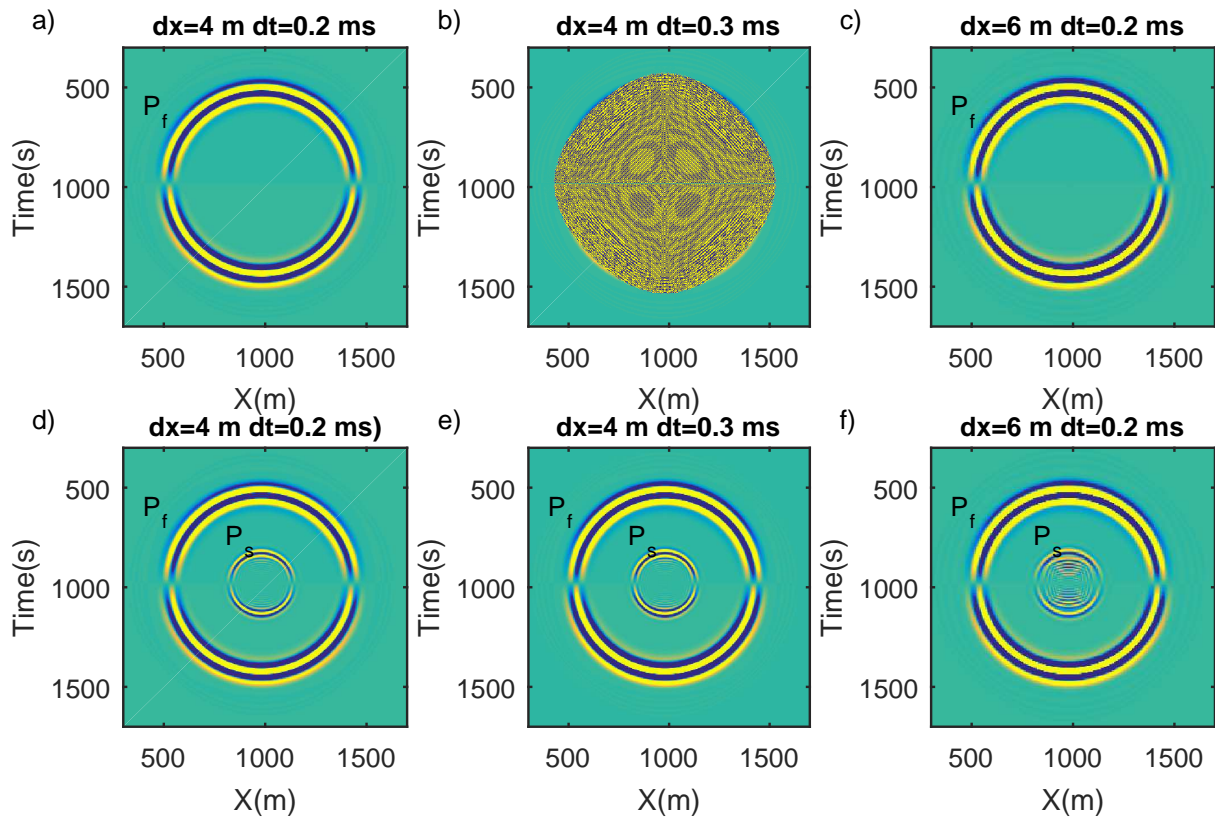


Figure 5.17: Sample snapshots with different pairs of $(\Delta t, h)$. The top row of snapshots belong to the diffusive case ($b \neq 0$) and the bottom row snapshots belong to the non-diffusive case ($b = 0$). The pair $(\Delta t, h) = (0.3 \text{ ms}, 4 \text{ m})$ leads to instability in the solution, indicating that the diffusive mode makes the solution less stable than the non-diffusive case. Moreover, the pair $(\Delta t, h) = (0.2 \text{ ms}, 6 \text{ m})$ lead to dispersion in the slow P-wave confirming that increasing the grid size results in more numerical dispersion.

5.9 Summary

I developed a 2D velocity-stress staggered-grid finite-difference code in MATLAB to simulate the wave propagation in poroelastic media. Biot equations of motion were discretized using a second order approximation for the time derivatives, and a fourth order approximation for the space derivatives. The program was then verified by showing some numerical models. In order to avoid the reflections from the grid boundaries a Perfectly Matched Layer (PML) was added to the algorithm. I then showed that how effectively the PML absorbs the outgoing waves at the boundaries. At the end of this chapter I carried out stability analysis and showed that our algorithm's stability matches the criteria suggested by Masson et al. (2006). We also showed that the presence of the the diffusive slow P-wave mode (when $b \neq 0$) makes the algorithm less stable than the case of zero fluid viscosity ($b=0$). By comparing the reduce in the amplitude of the fast P-wave in both cases of diffusive and non-diffusive, I realized that the energy loss is mainly due to the wave partitioning. In both cases the fast P-wave has lost amplitude with a negligible difference. However, in the next chapter I perform a time-lapse modeling for the Quest project considering the diffusive case.

Chapter 6

Time-lapse model-based numerical simulations for the Quest Carbon Capture and Storage project

6.1 Introduction

Prior to injection of CO₂ in Carbon Capture and Storage projects (CCS), seismic time lapse simulations need to be carried out to ensure the injected CO₂ could be detected in the seismic data in order to monitor the CO₂ over time. This is accomplished by defining a baseline scenario in which the storage formation is saturated with the in-situ fluid, and a monitor scenario in which some of the in-situ fluid is replaced by CO₂. The baseline and monitor scenarios are then used as the input models in the modeling program, and a set of synthetic data is generated for each scenario. Since the density and seismic P-wave velocity of the CO₂ is much lower than the formation's in-situ fluid, the physical properties of the storage rock undergo changes after injection. The most important change is the decrease in P-wave velocity and density of the saturated rock which leads to a change in the reflection coefficients of the top and the base of the storage formation. Moreover, the wave travels through the CO₂ plume with a slower velocity, causing a time delay for the reflections within and below the injection zone.

In the previous chapter the diffusive and non-diffusive slow P-wave modes were modeled using the poroelastic algorithm that I have developed, and as expected the slow P-wave was not detected in seismic data due to diffusion. Moreover, in both cases of diffusive and non-diffusive modes, some energy loss was observed that are believed to be caused by wave partitioning. By comparing the traces from both cases, a negligible difference between the fast P-wave amplitudes in the two cases was noticed. This observation suggests that in the fluid saturated media, the wave partitioning is more important in the energy loss than the fluid viscosity.

In this chapter a model-based time-lapse seismic simulations is carried out for the Quest project. For this purpose, a baseline and a monitor scenario are defined based on the available well logs from the area. The baseline scenario represents the subsurface for the Quest project prior to injection of CO₂. The monitor scenario represents the subsurface after injecting a certain amount of CO₂ into the BCS, and is generated by adding a CO₂ plume to the BCS in the baseline scenario. Both models are then run through the poroelastic algorithm to generate synthetic seismic sections. In order to observe the time-lapse effect caused by injection of CO₂ the monitor section is subtracted from the baseline section to obtain the residual section. Finally, to compare the developed poroelastic algorithm with an elastic one, the time-lapse modeling is also carried out using an elastic program and the results are compared with the ones from the poroelastic algorithm.

6.2 Baseline scenario

The baseline scenario is defined based on the physical properties of the subsurface prior to injection. The data simulated for this scenario is used as a reference data in order to track changes after injection of the CO₂. Figure 6.2.a shows the baseline acoustic impedance model defined for modeling. Acoustic impedance is the product of the bulk density and the P-wave velocity of the material. The reflection coefficients at the boundary of two materials depend on the contrast between their impedances. The higher the contrast, the larger the magnitude of the reflection coefficient at the boundary. For example, layer L₃ in the red color, has the largest impedance in the model. This layer is the Precambrian basin with high values of velocity and density. The high impedance contrast between the BCS and the Precambrian basin, that is the BCS-L₃ boundary, suggests a large reflection. In contrast, the reflection generated from the top of the BCS, that is the BCS-L₂ boundary, will be a weak reflection.

This model is a very simple model composed of 4 layers, and was defined based on the well log data in Chapter 3. Only the physical properties of BCS are affected by the CO₂ injection

and the rest of the layers remain unchanged after injection. Therefore, the reflections and travel times of any boundary that is not in contact with the BCS, do not alter by injection of CO₂. Consequently, having finer layers in the model is not necessary for the time-lapse modeling since the unchanged reflections will finally cancel out by subtraction of the sections.

Due to lack of information about the poroelastic properties of the subsurface, all layers other than BCS were assumed to be elastic. This was done by setting the porosity and fluid properties of these layers equal to zero in the poroelastic program and using the elastic properties of the saturated rock as the properties of the solid phase. This is identical to using an elastic algorithm. The physical properties of the elastic layers, which are denoted by L_1, L_2, L_3 are listed in Table 6.1. The poroelastic properties of BCS for the baseline scenario were extracted from the logs earlier in Chapter 3, and listed in Table 3.3 as BCS_{Base} .

Table 6.1: Physical properties of the elastic layers in the baseline and monitor scenarios.

Layer	Density (kg/m^3)	P-wave velocity (m/s)	S-wave velocity (m/s)
L_1	2600	3980	2380
L_2	2550	4000	2200
L_3	2650	5800	3300

6.3 Monitor scenario

For the monitor scenario some amount of CO₂ is needed to be hypothetically injected into the storage formation. For this purpose, a CO₂ plume is added to the BCS layer to generate a model that represents the subsurface after injection. The properties of the plume are the same as the properties of the BCS after substituting 40% of the in-situ brine with CO₂. These properties were calculated using the Gassmann's fluid substitution modeling earlier in Chapter 3 and listed in Table 3.3 as BCS_{Mon} . For both scenarios the factor b for BCS was assumed to be the constant value of 10^7 Pa sm^{-2} . Therefore the slow P-wave mode in this modeling is of the diffusive type and does not appear in the synthetic data as a traveling wave.

The CO₂ plume is assumed to have a cylindrical shape for simplicity in calculations. In reality, the flow path of the CO₂ strongly depends on the permeability distribution in the storage rock. However, we do not focus on the possible shapes and distribution of the plume in this dissertation. Thus, the numerical simulations is carried out with the simple cylindrical shape for the plume (Figure 6.1).

6.3.1 Plume size calculation

The size of the plume for the monitor model was estimated from the volumetric calculations. This was done based on the amount of the CO₂ injected in the course of one year, that is 1.2 million tonnes. It was shown in Chapter 3, that based on the Gassmann's fluid substitution modeling, the maximum change in the P-wave velocity occurs between 20% and 40 % CO₂ saturation. For this study the CO₂ saturation in the monitor scenario was chosen to be 40% that is a typical value for CO₂ saturation in such medium. To estimate the size of the plume, the volume of the CO₂ needed to be first calculated from its mass and density. The density of CO₂ was previously calculated based on the depth and pressure of the storage formation (Table 3.2). The volume of the injected CO₂ in a course of one year would be:

$$V_{CO_2} = \frac{M_{CO_2}}{\rho_{CO_2}} = \frac{1.2 \times 10^9 \text{ kg}}{625 \text{ kgm}^{-3}} = 1.92 \times 10^6 \text{ m}^3, \quad (6.1)$$

Assuming the cylindrical shape for the CO₂ plume (Figure 6.1), and the fact that CO₂ only occupies 40 % of the pore space, and the pore space in this case is 18 % of the rock, we have:

$$V_{Plume} = \frac{V_{CO_2}}{\phi \times S_{CO_2}} = \frac{1.92 \times 10^6 \text{ m}^3}{0.18 \times 0.4} = 2.67 \times 10^7 \text{ m}^3, \quad (6.2)$$

with ϕ being the porosity of the rock, and S_{CO_2} the saturation of CO₂. The volume of the cylindrical plume with the radius of R and height of h is:

$$V_{Plume} = \pi R^2 h, \quad (6.3)$$

then the the radius of the plume is:

$$R = \sqrt{\frac{V_{Plume}}{\pi h}} = \sqrt{\frac{2.67 \times 10^7 \text{ m}^3}{\pi(50 \text{ m})}} \approx 400\text{m}, \quad (6.4)$$

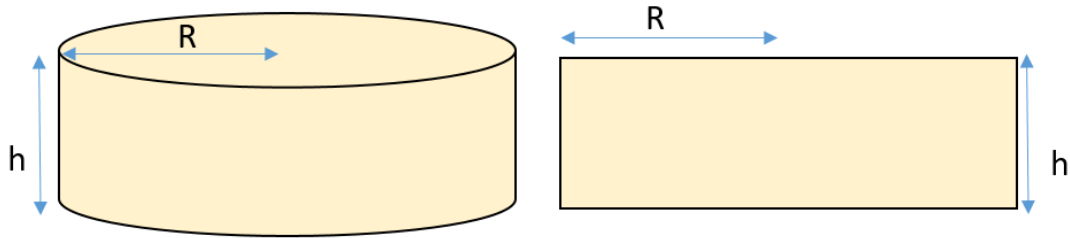


Figure 6.1: Cylindrical shape considered for the CO₂ plume for the monitor model (left). The height of the cylinder is equal to the thickness of the BCS. The cylinder will appear as a block in the 2D model (right)

where, the height of the plume was considered to be equal to the thickness of the BCS. The plume with a radius of 400 meters and a height of 50 meters was then added to the BCS in the monitor scenario. The acoustic impedance model of the monitor scenario is shown in Figure 6.2.b. The cool blue color of the plume indicates that, the impedance of the CO₂ plume is smaller than that of the BCS outside the plume. This decrease leads to a change in the reflection coefficients from the top and the base of the plume, along with a time delay for the reflection below the plume. All these changes lead to a difference between the baseline and monitor seismic sections which is even more visible after subtracting the sections. By this subtraction, all reflections that were unchanged after injection will be removed, and the residual is due to injection of CO₂.

6.4 Numerical modeling and discussion

In order to accomplish the time-lapse modeling, synthetic seismic sections were created for both baseline and monitor scenarios. This was done by generating 105 shot gathers with a shot interval of 20 m and receiver interval of 10 m. The shots and the receivers were located at the same depth, at 300 m below the surface. For each scenario, all the generated shot gathers were migrated separately using an Kirchhoff migration algorithm from the CREWES MATLAB

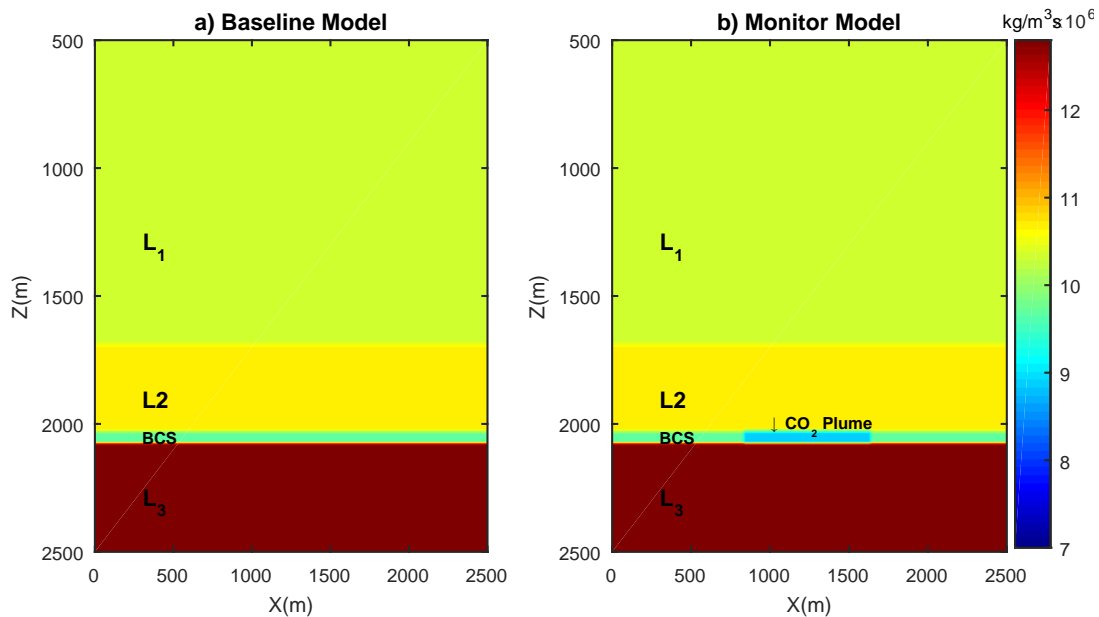


Figure 6.2: a) Acoustic impedance models for a) baseline and b) monitor scenarios. The warmer colors show higher impedance values. The blue color of the CO₂ plume in the monitor model indicates the decrease in the BCS impedance after injecting CO₂.

toolbox (Margrave, 2006) and were stacked to generate the seismic sections. The grid size and time interval used for the numerical modeling were 4 m and 0.2 ms, respectively. The thickness of the PML boundary was chosen to be 100 m in order to effectively avoid the numerical artifacts from the boundaries.

Figure 6.3.a-b show the generated seismic sections for both baseline and monitor scenarios using the poroelastic algorithm. It is noticed that injection of CO₂ has caused an increase in the reflection magnitudes from the top and bottom of the plume. The reflection from the top of the BCS has changed from a small negative reflection to a slightly larger negative reflection. Moreover, the reflection from the bottom of the plume has increased in magnitude. This reflection has also undergone a time shift due to the lower velocity of BCS after injection. The time shift was calculated from the cross correlation of the baseline and monitor traces and was equal to 1.7 ms. The amount of the time shift is affected by the thickness of the plume and the velocity change in the BCS. The longer distance that the wave travels through the plume, the more time

delay it will have. The time-lapse effect could be noticed more effectively when the monitor section is subtracted from the baseline section. Figure 6.3.c shows the difference section after subtracting the monitor section from the baseline section. The effect of the plume is more visible in this section since other reflections that are not affected by the injection are canceled out. The lateral extension of the plume as well as the top of the plume could be determined from the difference section.

One of the objectives of this dissertation was to compare the output of the poroelastic algorithm with an elastic one. Therefore, an elastic time-lapse study was also carried out by setting the fluid properties, as well as the porosity equal to zero in the poroelastic algorithm. The same models were used to generate synthetic sections in an elastic algorithm. For this purpose only the density, the P-wave velocity, and the S-wave velocity of the saturated rock were needed. For BCS, the properties ρ_{sat} , V_P , and V_S were taken from Table 3.3 for both baseline and monitor scenarios. For the rest of the layers, same properties defined in the the previous models (listed in Table 6.1) were used because they were already assumed to be elastic. The generated synthetic sections from the elastic modeling are shown in Figure 6.4. The effect of CO₂ injection on the reflections and the travel times in this case is similar to the one in the poroelastic case. However, it appears that the reflection from the top of BCS is weaker compared to the poroelastic case.

In Figure 6.5.a-b, selected traces from the synthetic sections from both elastic and poroelastic cases are plotted. All traces belong to position $X=1240\text{ m}$ that is almost the middle of the sections. In both cases the reflection from the top of the plume has become slightly larger in magnitude due to change in the properties of the plume. Furthermore, the reflection from the base of the plume is larger in monitor scenarios and has also delayed 1.9 ms in time. The magnitudes of the residual traces in both cases are comparable with the amplitudes of the baseline and scenario traces. This leads to the conclusion that, the time-lapse effect caused by the CO₂ injected in a course of one year in the Quest project will likely be large enough to be detected in the seismic data. However, this conclusion is based on our numerical modeling with a simple

model, and is free of noise. Therefore, it is necessary that the data have good quality and a high signal-to-noise ratio in order to yield results similar to our numerical results.

Figure 6.6 shows the same traces plotted separately for each scenario in order to compare the poroelastic algorithm with the elastic one. The reflection from the base of the plume in the elastic case is larger in magnitude than the one in the poroelastic case. This could be due to loss of energy in the poroelastic medium that was discussed in this thesis earlier. Moreover, the time-lapse residual traces for both cases are plotted in Figure 6.6.c. It is also noticed that, the time-lapse residual in the elastic case is larger in magnitude than the one in the poroelastic case. This difference may not be significant enough to confirm the poroelastic algorithm as a better solution for modeling. However, it needs to be noted that, in our model, only the BCS layer was considered to be poroelastic and the rest of the layers were elastic. It is expected that in the cases with multiple poroelastic layers, more energy will be lost due to poroelastic effect. The comparison between the two algorithms also confirms that the elastic algorithm overestimates the time lapse residual caused by the CO₂ injection. Amplitudes are important in most geophysical applications, including time-lapse studies. The poroelastic approach helps us to perform more accurate modeling, especially for cases in which the pore fluid is changing through time.

6.5 Summary

The developed poroelastic finite-difference program was successfully used to carry out a time-lapse model-based numerical modeling for the Quest project. Synthetic seismic sections were generated for baseline and monitor scenarios and compared in terms of changes in reflection magnitudes and also the time shift resulted from the injection of CO₂. The lateral extent of the CO₂ plume was observed in the difference section as well as the top of the plume. Furthermore, a comparison was done between the elastic and poroelastic cases, and the results revealed the energy loss in the poroelastic algorithm which is not observed in the elastic modeling.

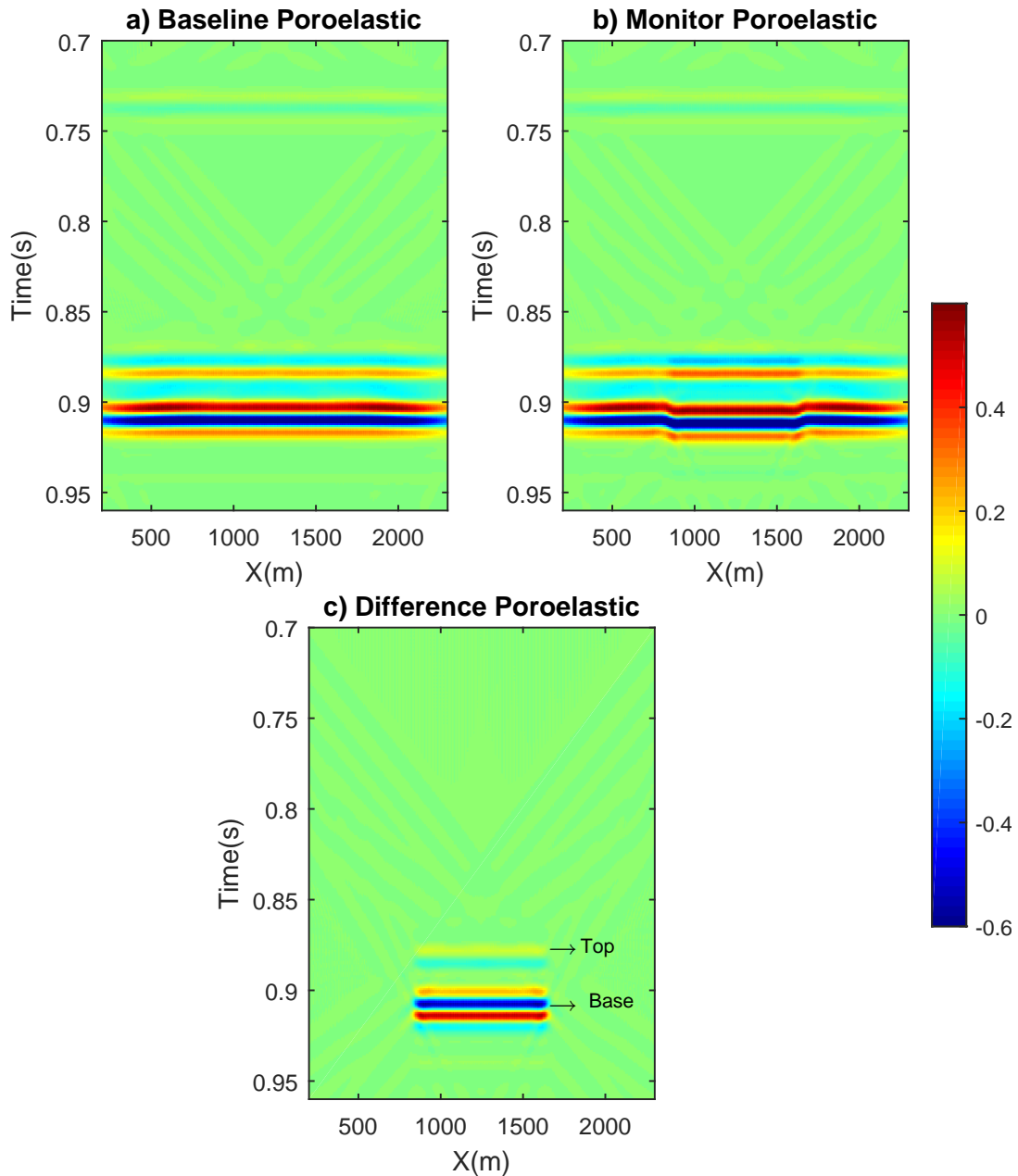


Figure 6.3: Synthetic seismic sections generated using the poroelastic algorithm for the baseline (a) and the monitor (b) scenarios. The changes in the reflections and also the time shift in the monitor section are due to the injection of CO_2 . The difference section is shown in (c) and is created by subtracting (b) from (a). The top and the base of the plume are observed in the difference section as a result of the change in the physical properties of the BCS

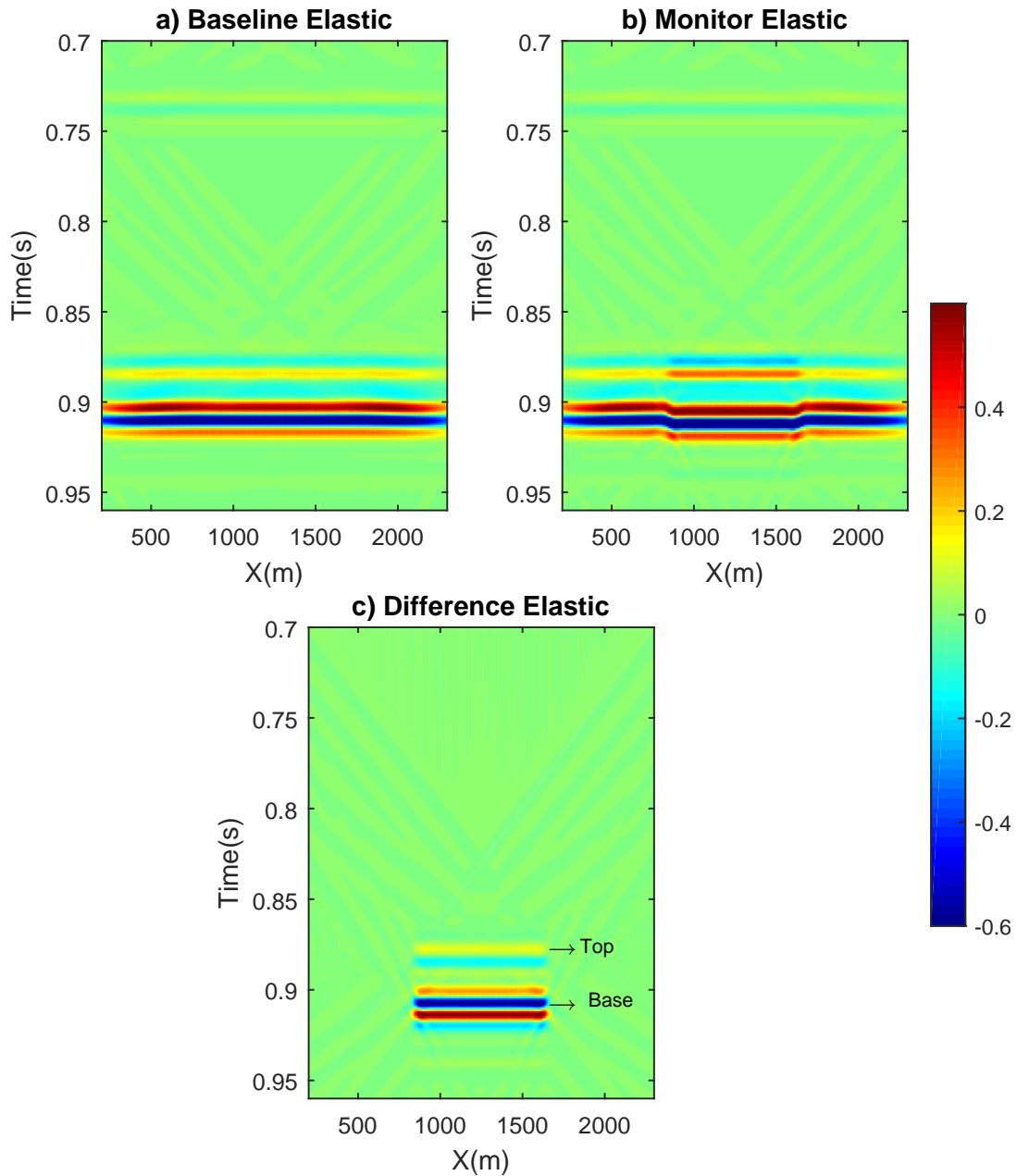


Figure 6.4: Synthetic seismic sections generated using an elastic algorithm for the baseline (a) and the monitor(b) scenarios. The changes in the reflections and also the time shift in the monitor section are due to the injection of CO₂. The difference section is shown in (c) and is created by subtracting (b) from (a).

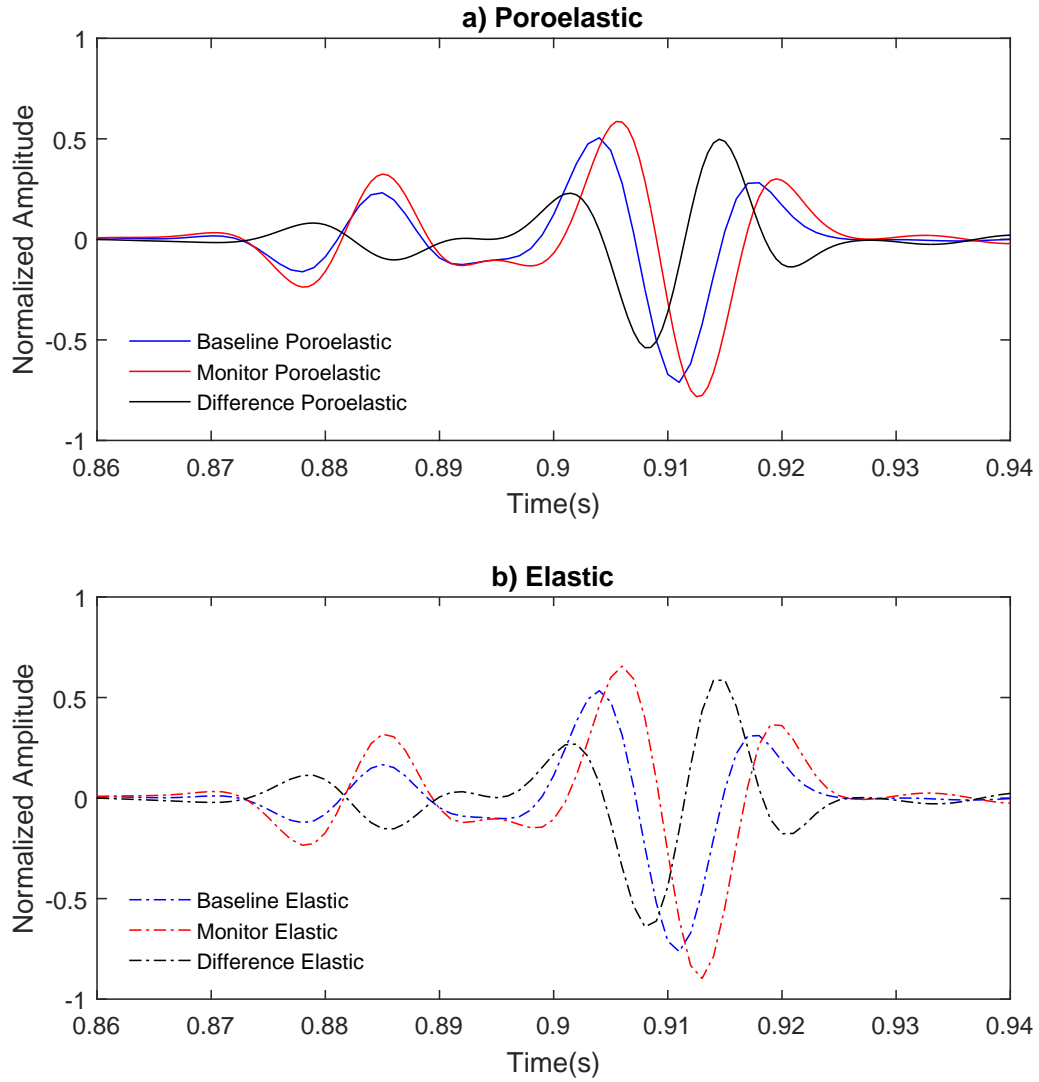


Figure 6.5: a) Extracted traces from the sections in Figure 6.3 at the location of 1240 m, and b) Extracted traces from the sections in Figure 6.4 at the same location. The traces are shown in blue for baseline scenario, red for monitor scenario and black for the difference of the two scenarios.

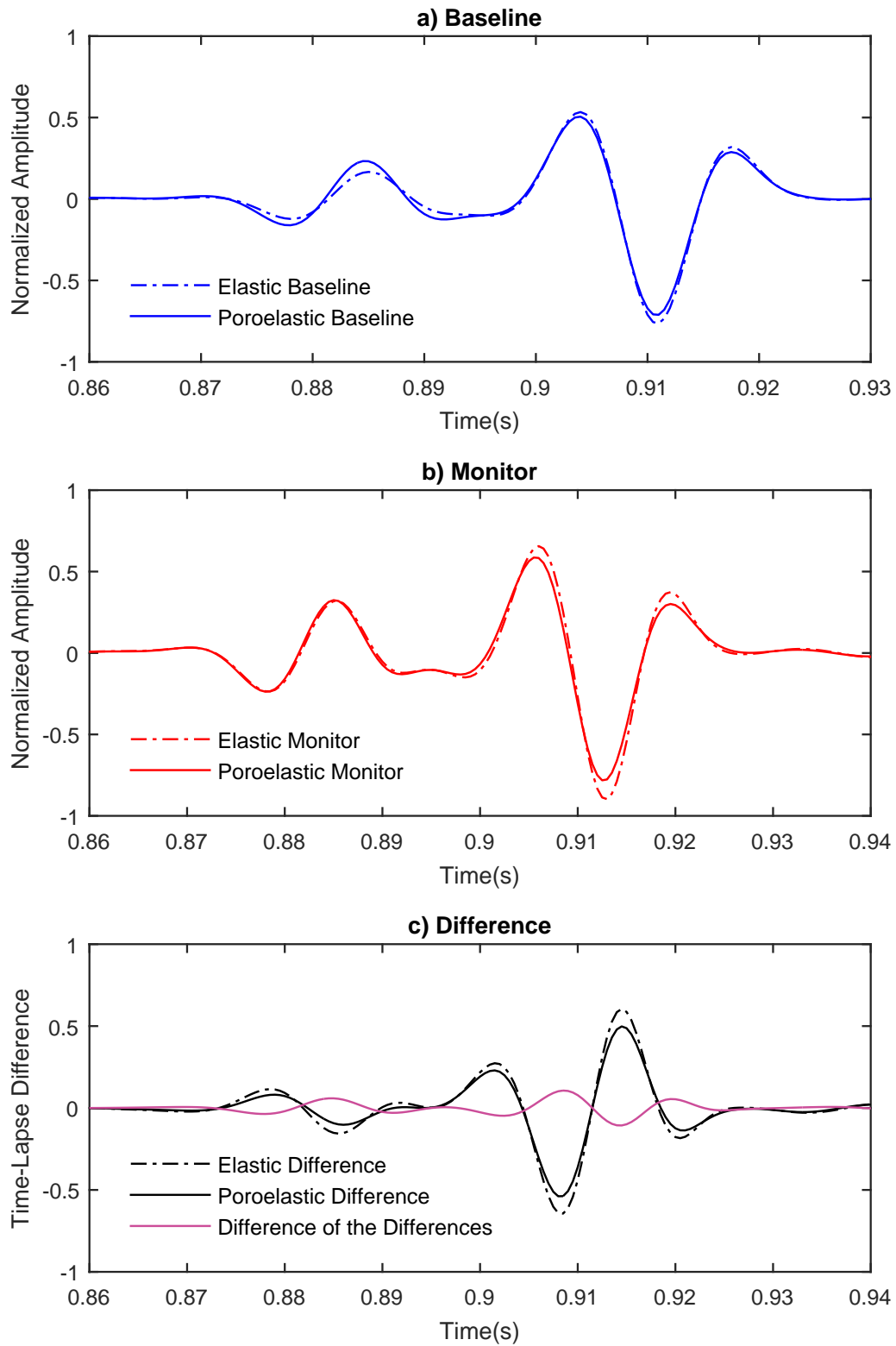


Figure 6.6: Comparison between the traces generated using elastic and poroelastic algorithms. These are the same traces in Figure 6.5, but plotted separately for the two scenarios and also the time-lapse difference.

Chapter 7

Conclusions and Future Work

7.1 Conclusions

Based on the results presented in this dissertation the following conclusions can be made:

- The Basal Cambrian Sands (BCS), at the depth of approximately 2 km is a suitable aquifer for Carbon Capture and Storage purpose. This saline aquifer is overlaid by multiple seals and baffles that prevent the potential upward migration of the injected CO_2 . In terms of porosity and permeability, the BCS qualifies as an ideal candidate for injection, since the storage formation needs to have relatively high porosity and permeabilities.
- The Gassmann's fluid substitution modeling results showed that, for 20 to 40 % of CO_2 saturation in the pore fluid of the Basal Cambrian Sands(BCS), there will be about 5-6% decrease in the P-wave velocity and 1.5% increase in S-wave velocity. The decrease in the P-wave velocity is essential in the monitoring of the injected CO_2 .
- The primary objective of this dissertation was to develop a finite-difference modeling program for the fluid saturated media. This was successfully done using the staggered-grid discretization method and the wave equations in the poroelastic media (Biot's theory). The program is developed for the 2D case and based on the velocity-stress formulation. Snapshots for two basic models were generated to verify that the code could properly generate the reflections, transmissions and also wave mode conversions.
- One important aspect of the wave propagation in poroelastic media is the fluid induced slow P-wave. This wave was modeled with the developed program for a fluid with $b = 0$. It was also shown that, by increasing the value of the factor b , the slow P-wave becomes

diffusive and therefore is not detected as a traveling wave. This is in complete agreement with the theory. Based on a comparison between the fast P-wave amplitude in two cases of zero and nonzero b factor, it was concluded that the energy loss in fluid saturated media is more due to the wave partitioning of the wave than to only the fluid viscosity.

- The perfectly matched layer(PML) method was used in order to eliminate the numerical reflections from the grid boundaries. This method effectively absorbed the outgoing waves, using only 20 grid nodes as the boundary region.
- The stability analysis was carried out for the developed algorithm and it was observed that with nonzero b factor, the algorithm is less stable than with zero b factor. We believe that the presence of the diffusive slow P-wave in the case of nonzero b factor leads to unstable results.
- A time-lapse numerical modeling for the Quest project was carried out using the developed program. The purpose was to investigate the feasibility of the seismic monitoring of the CO₂ for this project as well as the performance of the poroelastic modeling for such a project. The modeling results showed that the shape and the depth of the CO₂ plume could be qualitatively determined in the seismic data. However, the results were obtained from noise-free numerical modeling, therefore this conclusion should be apply to high quality seismic data.
- Finally, a comparison between the traces from the poroelastic time-lapse study and the equivalent traces from an elastic case was performed. It was noticed that in the poroelastic case there is energy missing due to the wave partitioning to the slow P-wave. Therefore the reflection amplitudes in the poroelastic case are slightly smaller than those in the elastic case. As in the poroelastic monitor model only the BCS was assumed to be poroelastic, it is expected that in a case with more poroelastic layers, more energy is lost due to the wave conversions. This is important in time-lapse feasibility analysis for the Carbon Capture

and Storage projects. Therefore, using the poroelastic algorithm, more realistic synthetic data can be modeled.

7.2 Future Work

Here are some challenges that I have encountered in this research and also suggestions for future work:

- Lack of information on fluid properties of the subsurface was one of the main challenges in this work. Most of the layers in the models defined for the time-lapse simulations were assumed to be elastic. The only poroelastic layer was the BCS, the target injection formation in the Quest project. Even for this formation, the fluid properties were roughly estimated using the temperature and pressure at the depth of the formation. However, although the only poroelastic layer (BCS) had a thickness of only 50 meters, the difference between the elastic and poroelastic medium was relatively considerable. Therefore, it is suggested that the algorithm should be tested for the models with more poroelastic layers in order to investigate the amount of the energy loss caused by the poroelastic effect.
- The stability of the algorithm decreases by considering the nonzero fluid viscosity ($b \neq 0$). The reason is thought to be the diffusive slow P-wave mode which is due to presence of the factor b . On the other hand, the assumption of zero fluid viscosity ($b = 0$) is unreal and generates several converted modes that do not exist in the real medium. In this case, the generated synthetic sections would suffer from the artifacts caused by these waves, and therefore the zero viscosity assumption is not a good option for modeling. A more detailed stability analysis is needed to be done in order to set up a general stability criteria for this algorithm.
- A quantitative analysis of the reflection and transmission coefficients in the poroelastic media could be done in a future work. Furthermore, the Amplitude Versus Offset (AVO)

of the poroelastic media could be looked into, and the results from the theory can be compared with the simulated data from the developed program.

- The developed modeling algorithm could be used for Full Waveform Inversion (FWI). In this process a set of data is generated for an initial model using the finite difference algorithm and the synthetic data are compared with the available real data. The model parameters are then updated based on the difference between the modeled and the real data and the process is repeated until the misfit is minimized. However, due to coupling of some of the parameters, the inversion problem becomes complicated in poroelastic media. In cases such as CO₂ sequestration, since only the fluid content changes through time, the inversion problem can be simplified and performed to calculate some fluid properties (De Barros et al., 2010). More work still needs to be done in the field of FWI specially in complicated media such as poroelastic media.
- The Biot's equations can be compared with the diffusive-viscous theory suggested by Korneev et al. (2004) that describes the frequency dependency of the reflection coefficients in a fluid saturated media. An interesting possibility yet to be investigated is to use this theory instead of Biot's specially for AVO-AVA analysis (Zhao et al., 2014).
- This program can be used in many different cases for modeling purposes. For example, in cases that the separate patches of fluid exist in the reservoir rock. In that case, the wave traveling through several patches of fluid results in more fluid related energy loss. Therefore, the poroelastic algorithm will be a proper modeling algorithm for such a medium.

Bibliography

- Alberta Department of Energy, 2015, Quest Carbon Capture and Storage Project Annual Summary Report:2014.
- Aldridge, D., Bartel, L., and Symons, N., 2004, Velocity-stress-pressure algorithm for 3d poroelastic wave propagation: 74th annual international meeting, **1920**.
- Alshuhail, A. A., 2011, CO₂ sequestration site characterization and time-lapse monitoring using reflection seismic methods: Ph.D. thesis, University of Calgary.
- Arts, R., Eiken, O., Chadwick, A., Zweigel, P., Van der Meer, L., and Zinszner, B., 2004, Monitoring of CO₂ injected at Sleipner using time-lapse seismic data: *Energy*, **29**, No. 9, 1383–1392.
- Bachu, S., Broulotte, M., Grobe, M., and Stewart, S., 2000, Suitability of the Alberta subsurface for carbon-dioxide sequestration in geological media.
- Bachu, S., Stewart, S. et al., 2002, Geological sequestration of anthropogenic carbon dioxide in the western Canada sedimentary basin: suitability analysis: *Journal of Canadian Petroleum Technology*, **41**, No. 02.
- Berenger, J.-P., 1994, A perfectly matched layer for the absorption of electromagnetic waves: *Journal of computational physics*, **114**, No. 2, 185–200.
- Biot, M. A., 1956, Theory of propagation of elastic waves in a fluid-saturated porous solid. i. low-frequency range: *The Journal of the Acoustical Society of America*, **28**, No. 2, 168–178.
- Biot, M. A., 1962, Mechanics of deformation and acoustic propagation in porous media: *Journal of applied physics*, **33**, No. 4, 1482–1498.
- Carcione, J. M., Herman, G. C., and Ten Kroode, A., 2002, Seismic modeling: *Geophysics*, **67**, No. 4, 1304–1325.
- Carcione, J. M., Morency, C., and Santos, J. E., 2010, Computational poroelasticity -A review: *Geophysics*, **75**, No. 5, 75A229-75A243.
- Carcione, J. M., Picotti, S., Gei, D., and Rossi, G., 2006, Physics and seismic modeling for monitoring CO₂ storage: *Pure and Applied Geophysics*, **163**, No. 1, 175–207.
- Carcione, J. M., and Quiroga-Goode, G., 1995, Some aspects of the physics and numerical modeling of Biot compressional waves: *Journal of Computational Acoustics*, **3**, No. 04, 261–280.
- Chadwick, A., Arts, R., and Eiken, O., 2005, 4d seismic quantification of a growing CO₂ plume at Sleipner, North Sea, *in Geological Society, London, Petroleum Geology Conference series*, vol. 6, Geological Society of London, 1385–1399.

- Chew, W., and Liu, Q., 1996, Perfectly matched layers for elastodynamics: a new absorbing boundary condition: *Journal of Computational Acoustics*, **4**, No. 04, 341–359.
- Collino, F., and Tsogka, C., 2001, Application of the perfectly matched absorbing layer model to the linear elastodynamic problem in anisotropic heterogeneous media: *Geophysics*, **66**, No. 1, 294–307.
- Dai, N., Vafidis, A., and Kanasewich, E., 1995, Wave propagation in heterogeneous, porous media: A velocity-stress, finite-difference method: *Geophysics*, **60**, No. 2, 327–340.
- De Barros, L., Dietrich, M., and Valette, B., 2010, Full waveform inversion of seismic waves reflected in a stratified porous medium.: *Geophysical Journal International.*, **182**, No. 3, 1543-1556.
- Gassmann, F., 1951, *Über die elastizität poroser medien.:* Vier. der Natur. Gesellschaft in Zurich, **96**, 1–23.
- Government of Alberta , 2015, Climate leadership report to Minister. Edmonton, AB.
- Greaves, R. J., and Fulp, T. J., 1987, Three-dimensional seismic monitoring of an enhanced oil recovery process: *Geophysics*, **52**, No. 9, 1175–1187.
- Grobe, M., 2000, Distribution and thickness of salt within the devonian elk point group, western canada sedimentary basin, Tech. rep.
- Gurevich, B., Zyrianov, V. B., and Lopatnikov, S. L., 1997, Seismic attenuation in finely layered porous rocks: Effects of fluid flow and scattering: *Geophysics*, **62**, No. 1, 319–324.
- Hitchon, B., 1984, Geothermal gradients, hydrodynamics, and hydrocarbon occurrences, alberta, canada: *AAPG Bulletin*, **68**, No. 6, 713–743.
- IPCC, 2015, *Climate Change 2014: Mitigation of Climate Change*, vol. 3: Cambridge University Press.
- Jianfeng, Z., 1999, Quadrangle-grid velocity–stress finite difference method for poroelastic wave equations: *Geophysical Journal International*, **139**, No. 1, 171–182.
- Korneev, V. A., Goloshubin, G. M., Daley, T. M., and Silin, D. B., 2004, Seismic low-frequency effects in monitoring fluid-saturated reservoirs: *Geophysics*, **69**, No. 2, 522–532.
- Levander, A. R., 1988, Fourth-order finite-difference p-sv seismograms: *Geophysics*, **53**, No. 11, 1425–1436.
- Lumley, D. E., 2001, Time-lapse seismic reservoir monitoring: *Geophysics*, **66**, No. 1, 50–53.
- Madariaga, R., 1976, Dynamics of an expanding circular fault: *Bulletin of the Seismological Society of America*, **66**, No. 3, 639–666.
- Margrave, G. F., 2006, *Crewes matlab toolbox* (<https://www.crewes.org/>).

- Masson, Y., Pride, S., and Nihei, K., 2006, Finite difference modeling of biot's poroelastic equations at seismic frequencies: *Journal of Geophysical Research: Solid Earth*, **111**, No. B10.
- Metz, B., Davidson, O., De Coninck, H., Loos, M., Meyer, L. et al., 2005, Carbon dioxide capture and storage.
- Michael, K., Bachu, S., Buschkuehle, B. E., Haug, K., and Talman, S., 2009, Comprehensive characterization of a potential site for CO₂ geological storage in central Alberta, Canada.
- Norris, A. N., 1985, Radiation from a point source and scattering theory in a fluid-saturated porous solid: *The Journal of the Acoustical Society of America*, **77**, No. 6, 2012–2023.
- Shapiro, S. A., and Müller, T. M., 1999, Seismic signatures of permeability in heterogeneous porous media: *Geophysics*, **64**, No. 1, 99–103.
- Sheen, D.-H., Tuncay, K., Baag, C.-E., and Ortoleva, P. J., 2006, Parallel implementation of a velocity-stress staggered-grid finite-difference method for 2-d poroelastic wave propagation: *Computers & Geosciences*, **32**, No. 8, 1182–1191.
- Shell Canada Limited, 2010, Quest carbon capture and storage project, directive 65: application for a CO₂ acid gas storage scheme, Calgary, AB, Tech. rep.
- Slind, O., Andrews, G., Murray, D., Norford, B., Paterson, D., Salas, C., and Tawadros, E., 1994, Middle Cambrian to lower Ordovician strata of the western Canada sedimentary basin: *Geological Atlas of the Western Canada Sedimentary Basin*, **4**, 87–108.
- Smith, T. M., Sondergeld, C. H., and Rai, C. S., 2003, Gassmann fluid substitutions: A tutorial: *Geophysics*, **68**, No. 2, 430–440.
- Spencer, J. W., Cates, M. E., and Thompson, D. D., 1994, Frame moduli of unconsolidated sands and sandstones: *Geophysics*, **59**, No. 9, 1352–1361.
- Vera, V., 2012, Seismic modeling of CO₂ in a sandstone aquifer, Priddis, Alberta: M.Sc. thesis, University of Calgary.
- Virieux, J., 1984, Sh-wave propagation in heterogeneous media: velocity-stress finite-difference method: *Geophysics*, **49**, No. 11, 1933–1942.
- Virieux, J., 1986, P-sv wave propagation in heterogeneous media: Velocity-stress finite-difference method: *Geophysics*, **51**, No. 4, 889–901.
- Wang, X., Zhang, H., and Wang, D., 2003, Modelling of seismic wave propagation in heterogeneous poroelastic media using a high-order staggered finite-difference method: *Chinese Journal of Geophysics*, **46**, No. 6, 842–849.
- Wang, Z., 1997, Feasibility of time-lapse seismic reservoir monitoring: The physical basis: *The Leading Edge*, **16**, No. 9, 1327–1330.

- Wang, Z., Cates, M. E., and Langan, R. T., 1998, Seismic monitoring of a CO₂ flood in a carbonate reservoir: A rock physics study: *Geophysics*, **63**, No. 5, 1604–1617.
- Wang, Z., Wang, H., and Cates, M. E., 2001, Effective elastic properties of solid clays: *Geophysics*, **66**, No. 2, 428–440.
- Watts, G., Jizba, D., Gawith, D., and Gutteridge, P., 1996, Reservoir monitoring of the Magnus field through 4d time-lapse seismic analysis: *Petroleum Geoscience*, **2**, No. 4, 361–372.
- Zhao, H., Gao, J., and Liu, F., 2014, Frequency-dependent reflection coefficients in diffusive-viscous media: *Geophysics*, **79**, No. 3, T143–T155.
- Zeng, Y. Q., He, J. Q., and Liu, Q. H., 2001, The application of the perfectly matched layer in numerical modeling of wave propagation in poroelastic media: *Geophysics*, **66**, No. 4, 1258–1266.
- Zhu, X., and McMechan, G., 1991, Numerical simulation of seismic responses of poroelastic reservoirs using Biot theory: *Geophysics*, **56**, No. 3, 328–339.

Appendix A

Matlab Code

- Poro2D function

```
function Poro2D (Modeltype,dx,dt,freq,shotx,shotz,shotspacing,numshot,...
xmax,totaldepth,tmax,bound,recz,numsnap)
%Modeltype: 1=Quest Baseline %4=Quest Monitor %3=2 layer model ;
%dx=grid size;
%dt=time step
%freq=dominant frequency;
% shotx= x location of first shot;
% shot z= depth of the first sot;
% shotspacing= shot spacing;
% numshot= number of shots;
% xmax= size of the model
% totaldepth= the depth of model if modeltype==3;
% tmax= total time of computation;
% bound= thickness of PML boundary ;
% recz=depth of the receivers;
% numsnap= number of snapshots to be displayed;
tal=round(tmax/dt);
len=tal/numsnap;
lp=round(bound/dx);
[Txxn,Tzzn,Sn,Txzn,sourcez,w,rec,draft,nz,X,Z]=...
gridit(0,xmax,dx,shotz,recz,dt,freq,0);
[Vpc,VS,phof1,rhos1,phi1,Kmin1,KF1,etta1,kappa1,depths,varg]=...
PProperties2(Modeltype,totaldepth);
[Vp,Vs,rhof,rhos,phi,Kmin,KF,eta,kapa]=...
PModel(Vpc,VS,phof1,rhos1,phi1,Kmin1,KF1,etta1,...
kappa1,depths,draft,dx,varg);
[A, B, C,lamdac, MM, mu, b, alpha,rho]=...
Pcoeffi(Vp,Vs,rhof,rhos,phi,Kmin,KF,eta,kapa,draft);
tl=length(w);
I=draft;I(:,:)=1;
ax=draft;az=draft;
for iz=1:bound
    ax(:,iz)=(25.5*Vp(:,iz)/((bound*dx)^3)).*(((bound-iz)*dx).^2);
    ax(:,nz+3-bound+iz:end)=(25.5*Vp(:,nz+...
3-bound+iz:end)/((bound*dx)^3)).*((iz*dx).^2);
    az(iz,:)=(25.5*Vp(iz,)/((bound*dx)^3)).*(((bound-iz)*dx).^2);
    az(nz+3-bound+iz:end,:)=(25.5*Vp(nz+...
```

```

    3-bound+iz:end, :)/((bound*dx)^3)).*((iz*dx).^2);
end
for io=1:5
ax=smooth2a(ax,4,4);
az=smooth2a(az,4,4);
end
Vxnegx=draft; Vxnegz=draft; Vznegx=draft; Vznegz=draft; Vzpoz=draft;
Wxpox=draft; Wxpoz=draft; Wzpoz=draft; Wzpoz=draft; ff=0;
Txxnx=draft; Txxnz=draft; Tzznx=draft; Tzznz=draft; Txxnz=draft;
Wxnegx=draft; Wxnegz=draft; Wznegx=draft; Wznegz=draft;
Snx=draft; Snz=draft; Txxnz=draft;

    for si=0:numshot-1
fs=(shotx+si*shotspaceing);
sourcez=round(fs/dx);
for h=1:tal
if h<tl
pphi=phi(sourcez,sourcez);
init=draft;
init(sourcez-1:sourcez,sourcez-1:sourcez)=w(1+h,1)*(1-pphi);
Txxn=init+Txxn;
Tzzn=init+Tzzn;
Sn=init*(pphi/(1-pphi))+Sn;
end
G1=0Ddxt(Sn,dx);G2=0Ddxt(Txxn,dx);G3=0Ddz(Txzn,dx);
G4=0Ddzt(Sn,dx);G5=0Ddx(Txzn,dx);G6=0Ddzt(Tzzn,dx);
Vxpox=(I-(ax*dt)).*Vxnegx+((-B.*G1)+(A.*(G2))- (B.*b.*Wxnegx))*dt;
Vxpoz=(I-(az*dt)).*Vxnegz+(A.*(G3))- (B.*b.*Wxnegz))*dt;
Vzpoz=(I-(ax*dt)).*Vznegz+(A.*G5- (B.*b.*Wznegx))*dt;
Vzpoz=(I-(az*dt)).*Vznegz+(-B.*G4+A.*G6- (B.*b.*Wznegz))*dt;
Wxpox=(I-(ax*dt)).*Wxnegx+(C.*G1+B.*G2+(C.*b.*Wxnegx))*dt;
Wxpoz=(I-(az*dt)).*Wxnegz+(B.*G3+(C.*b.*Wxnegz))*dt;
Wzpoz=(I-(ax*dt)).*Wznegz+(B.*G5)+(C.*b.*Wznegx))*dt;
Wzpoz=(I-(az*dt)).*Wznegz+(C.*G4+B.*G6+(C.*b.*Wznegz))*dt;

Vxpo=Vxpoz+Vxpox;
Vzpo=Vzpoz+Vzpoz;
Wxpo=Wxpoz+Wxpox;
Wzpo=Wzpoz+Wzpoz;
D1=0Ddx(Vxpo,dx);D3=0Ddz(Vzpo,dx);D4=0Ddx(Wxpo,dx);D5=0Ddz(Wzpo,dx);
E1=0Ddxt(Vzpo,dx);E2=0Ddzt(Vxpo,dx);
Txxn1x=(I-(ax*dt)).*Txxnx+(2*(mu.*D1)+(lamdac.*(D1))+((alpha.*MM).*(D4)))*dt;
Txxn1z=(I-(az*dt)).*Txxnz+((lamdac.*D3)+(alpha.*MM.*D5))*dt;
Tzzn1x=(I-(ax*dt)).*Tzznx+((lamdac.*D1)+(alpha.*MM.*D4))*dt;
Tzzn1z=(I-(az*dt)).*Tzznz+((2*mu.*D3)+(lamdac.*D3)+(alpha.*MM.*D5))*dt;

```

```

Txzn1x=(I-(ax*dt)).*Txznx+(mu.*E1)*dt;
Txzn1z=(I-(az*dt)).*Txznz+(mu.*E2)*dt;
Sn1x=(I-(ax*dt)).*Snx-((alpha.*MM.*D1)+(MM.*D4))*dt;
Sn1z=(I-(az*dt)).*Snz-((alpha.*MM.*D3)+(MM.*D5))*dt;
shotvx(h,:)=Vxpo(rec,:);
shotvz(h,:)=Vzpo(rec,:);
Txxnx=Txxn1x; Txxnz=Txxn1z; Tzznx=Tzzn1x; Txxn=Txxnz+Txxnx;
Tzznz=Tzzn1z; Txznx=Txzn1x; Txznz=Txzn1z; Tzzn=Tzznz+Tzznx;
Vxnegx=Vxpox; Vxnegz=Vxpoz; Vznegx=Vzpox; Vznegz=Vzpoz;
Wxnegx=Wxpox; Wxnegz=Wxpoz; Wznegx=Wzpox; Wznegz=Wzpoz;
Txzn=Txznz+Txznx; Snx=Sn1x; Snz=Sn1z; Sn=Snx+Snz;
if numsnap~=0
if mod(h,len)==0
imagesc(X,Z,Vzpo);colormap('copper');
drawnow
end; end;end
if Modeltype==1
f = [ 'Baseline', num2str(fs), '.mat' ];
save(f,'shotvz','shotvx','dt','dx','Vp')
else if Modeltype==4
f = [ 'Monitor', num2str(fs), '.mat' ];
save(f,'shotvz','shotvx','dt','dx','Vp')
end;end;
Vxnegx=draft; Vxnegz=draft; Vznegx=draft; Vznegz=draft;
Txxnx=draft; Txxnz=draft; Tzznx=draft; Tzznz=draft; Txznx=draft;
Wxnegx=draft; Wxnegz=draft; Wznegx=draft; Wznegz=draft; Txznz=draft;
Snx=draft; Snz=draft; Sn=draft; Txxn=draft;Tzzn=draft;Txzn=draft;
end

```

- gridit function

```

function[Txxn,Tzzn,Sn,Txzn,sourcez,w,rec,draft,nz,X,Z]=...
gridit(varargin,xmax,dx,sz,recz,dtsamp,f,wavetype)
zmax=xmax;
sx=round(xmax/2);
geo=recz;
Z=0:dx:xmax;
X=0:dx:zmax;
nz=round(zmax/dx);nx=round(xmax/dx);
draft=zeros(nz+2,nx+2);
if wavetype==0
[w,tw]=ricker(dtsamp,f,0.064);%hold on;plot(tw,w)
else
[w,tw]=wavemin(dtsamp,f,0.064);
end

```

```

sourcez=round(sz/dx);
rec=round(geo/dx);
Txxn=draft;Tzzn=draft;
Sn=draft;Txzn=draft;

```

- PProperties2 function

```

function [Vpc,Vs,rhof,rhos,phi,Kmin,KF,etta,kappa,depths,varg]=...
PProperties(vargin,depth1)
if vargin==4
    disp('poro monitor')
    Vpc = [3980 4000 4100 5800 3850];
    Vs = [2380 2200 2350 3300 2365];
    rhof=[0 0 0 0 0];
    rhos = [2600 2550 2650 2650 2650];
    rhof=[0 0 1230 0 1050];
    rhos = [2600 2600 2600 2600 2600];
    phi = [0.00 0.00 0.18 0.00 0.18];
    Kmin=[43.5*10^9 43.5*10^9 43.5*10^9 43.5*10^9 43.5*10^9];
    KF=[0 0 3.05*10^9 0 0.254*10^9];
    etta =[0 0 10^-5 0 10^-5];
    kappa = [10^-12 10^-12 10^-12 10^-12 10^-12];
    depths = [1700 2000 2050];
    varg=5;
else if vargin==1
    disp('poro baseline')
    Vpc = [3980 4000 4100 5800];
    Vs = [2380 2200 2350 3300];
    rhof=[0 0 1230 0 ];
    rhos = [2600 2600 2600 2600];
    phi = [0 0 0.18 0 ];
    Kmin=[43.5*10^9 43.5*10^9 43.5*10^9 43.5*10^9 ];
    KF=[0 0 3.05*10^9 0];
    etta =[0 0 10^-5 0];
    kappa = [10^-12 10^-12 10^-12 10^-12 ];
    depths = [1700 2000 2050];
    varg=1;
else if vargin==3
    disp(' two layer poroelastic')
    Vpc = [3850 4100];
    Vs = [2365 2350];
    rhof=[1050 1230];
    rhos = [2600 2600];
    phi = [0.18 0.18];
    Kmin =[43.5*10^9 43.5*10^9];

```

```

KF=[0.254*10^9 3.05*10^9];
etta =[ 10^-5 10^-5];
kappa = [10^-12 10^-12];
depths = [depth1];
  varg=1;
    end;end;end;

```

- PModel function

```

function [Vp,Vs,rhof,rhos,phi,Kmin,KF,etta,kappa]=PModel(PVel,SVel,...
FluidDensity,SolidDensity,phi1,Kmin1,KF1,etta1,kappa1,depths,draft,dx,varg)
  if varg==5 %block model for monitor scenario
    d=length(depths);
dp=round(depths/dx);
  Vp=draft; Vs=draft; rhof=draft;
  rhos=draft; phi=draft; Kmin=draft;
  KF=draft; etta=draft; kappa=draft;
z=1; [piz,pix]=size(draft);
for j=1:d
kj=dp(j) ;
Vp(z:kj,:)=PVel(j) ;
Vs(z:kj,:)=SVel(j) ;
rhof(z:kj,:)=FluidDensity(j) ;
rhos(z:kj,:)=SolidDensity(j) ;
phi(z:kj,:)=phi1(j) ;
Kmin(z:kj,:)=Kmin1(j) ;
KF(z:kj,:)=KF1(j) ;
etta(z:kj,:)=etta1(j) ;
kappa(z:kj,:)=kappa1(j) ;
z=kj+1;
  end
Vp(z:end,:)=PVel(j+1) ;
Vs(z:end,:)=SVel(j+1) ;
rhof(z:end,:)=FluidDensity(j+1) ;
rhos(z:end,:)=SolidDensity(j+1) ;
phi(z:end,:)=phi1(j+1) ;
Kmin(z:end,:)=Kmin1(j+1) ;
KF(z:end,:)=KF1(j+1) ;
etta(z:end,:)=etta1(j+1) ;
kappa(z:end,:)=kappa1(j+1) ;
mx1=round(piz/2-400/dx); mx2=round(pix/2+400/dx);
  mz1=dp(2)+1;mz2=dp(3);
Vp(mz1:mz2,mx1:mx2)=PVel(d+2) ;
Vs(mz1:mz2,mx1:mx2)=SVel(d+2) ;
rhof(mz1:mz2,mx1:mx2)=FluidDensity(d+2) ;

```

```

rhos(mz1:mz2,mx1:mx2)=SolidDensity(d+2) ;
phi(mz1:mz2,mx1:mx2)=phi1(d+2) ;
Kmin(mz1:mz2,mx1:mx2)=Kmin1(d+2) ;
KF(mz1:mz2,mx1:mx2)=KF1(d+2) ;
etta(mz1:mz2,mx1:mx2)=etta1(d+2) ;
kappa(mz1:mz2,mx1:mx2)=kappa1(d+2) ;

else %% layered model
d=length(depths);
dp=round(depths/dx);
Vp=draft; Vs=draft; rhof=draft;
rhos=draft; phi=draft; Kmin=draft;
KF=draft; etta=draft; kappa=draft;
z=1;
for j=1:d
kj=dp(j) ;
Vp(z:kj,:)=PVel(j) ;
Vs(z:kj,:)=SVel(j) ;
rhof(z:kj,:)=FluidDensity(j) ;
rhos(z:kj,:)=SolidDensity(j) ;
phi(z:kj,:)=phi1(j) ;
Kmin(z:kj,:)=Kmin1(j) ;
KF(z:kj,:)=KF1(j) ;
etta(z:kj,:)=etta1(j) ;
kappa(z:kj,:)=kappa1(j) ;
    z=kj+1;
    end
Vp(z:end,:)=PVel(j+1) ;
Vs(z:end,:)=SVel(j+1) ;
rhof(z:end,:)=FluidDensity(j+1) ;
rhos(z:end,:)=SolidDensity(j+1) ;
phi(z:end,:)=phi1(j+1) ;
Kmin(z:end,:)=Kmin1(j+1) ;
KF(z:end,:)=KF1(j+1) ;
etta(z:end,:)=etta1(j+1) ;
kappa(z:end,:)=kappa1(j+1) ;
end

```

- Pceoffi function

```

function[A, B, C, lamdac, MM, mus, b, alpha,rho]=...
Pceoffi(Vp,Vs,rhof,rhos,phi,Kmin,KF,eta,kapa,draft,lim,dp)
I=draft;I(:,:)=1;
rho1=(I-phi).*rhos; rho2=phi.*rhof;
rho=rho1+rho2;

```

```

mus=((Vs.^2).*rho);
Ksat=((rho.*(Vp.^2))-(4*mus./3));
BB=((phi.*Kmin)./KF);AA=(BB+(I-phi));
CC=(Ksat./Kmin)-(I+phi);
KDry=((Ksat.*AA)-Kmin)./(BB+CC);
alpha=1-(KDry./Kmin);
MM=((phi./KF)+((alpha-phi)./Kmin)).^-1;Tur=1;
mm=(Tur*rhof)./phi;
lamdac=(rho.*(Vp.^2)-(2*mus));
DE=(mm.*rho)-(rhof.^2);
b=(eta)./kapa;
A=(1./(rho-(phi.*rhof)));
B=-(rhof)./DE;
C=-(rho)./DE;
h2=find(isnan(B)); B(h2)=0;
h3=find(isnan(C)); C(h3)=0;
h4=find(isnan(A)); A(h4)=0;
h7=find(isnan(b)); b(h7)=0;
h8=find(isnan(MM)); MM(h8)=0;
h9=find(isnan(alpha)); alpha(h9)=0;

```

- ODDx function

```

function [output]= ODDx(input,delx)
[nrows,ncolumns]=size(input);
input2=zeros(nrows+4,ncolumns+4);
input2(3:nrows+2,3:ncolumns+2)=input;
clear input
xm=3:nrows+2;zm=3:ncolumns+2;
s=input2;
ot =27*(s(xm,zm+1)-s(xm,zm))-(s(xm,zm+2)-s(xm,zm-1)));
output=ot/(24*delx);

```

- ODDxt function

```

function [output]= ODDxt(input,delx)
[nrows,ncolumns]=size(input);
input2=zeros(nrows+4,ncolumns+4);
input2(3:nrows+2,3:ncolumns+2)=input;
clear input
xm=3:nrows+2;zm=3:ncolumns+2;
s=input2;
ot =27*(s(xm,zm)-s(xm,zm-1))-(s(xm,zm+1)-s(xm,zm-2)));
output=ot/(24*delx);

```

- ODDz function

```
function [output]= ODDz(input,delx)
[nrows,ncolumns]=size(input);
input2=zeros(nrows+4,ncolumns+4);
input2(3:nrows+2,3:ncolumns+2)=input;
clear input
xm=3:nrows+2;zm=3:ncolumns+2;
s=input2;
ot =27*(s(xm+1,zm)-s(xm,zm))-(s(xm+2,zm)-s(xm-1,zm));
output=ot/(24*delx);
```

- ODDzt function

```
function [output]= ODDzt(input,delx)

[nrows,ncolumns]=size(input);
input2=zeros(nrows+4,ncolumns+4);
input2(3:nrows+2,3:ncolumns+2)=input;
clear input
xm=3:nrows+2;zm=3:ncolumns+2;
s=input2;
ot =27*(s(xm,zm)-s(xm-1,zm))-(s(xm+1,zm)-s(xm-2,zm));
output=ot/(24*delx);
```